Development of the Dual-Vertical-Axis Wind Turbine with Active Blade Pitch Control

Daniel McLean

Presented in Partial Fulfillment of the Requirements for the Degree of

Master of Applied Science

(Mechanical Engineering)

Mechanical, Industrial and Aerospace Engineering

Concordia University

Montréal, Québec, Canada

December 2017

Concordia University

School of Graduate Studies

This is to certify that the thesis prepared

By: **Daniel McLean**

Entitled: **Development of the Dual-Vertical-Axis Wind Turbine with Active Blade Pitch Control**

and submitted in partial fulfillment of the requirements for the degree of

Master of Applied Science (Mechanical Engineering)

complies with the regulations of this University and meets the accepted standards with respect to originality and quality.

Signed by the Final Examining Committee:

_____ Chair
Dr. Zezhong Chevy Chen

_____ Examiner
Dr. Mojtaba Kheiri

_____ Examiner
Dr. Samuel Li

_____ Supervisor
Dr. Marius Paraschivoiu

Approved by _____
Martin D. Pugh, Chair
Department of Mechanical and Industrial Engineering

_____ 2017

_____
Amir Asif, Dean
Faculty of Engineering and Computer Science

Abstract

Wind turbines will play a crucial role in the global energy transition from a fossil fuel-based world to a renewable-based one. Horizontal-axis wind turbines (HAWTs) currently dominate the commercial sector, although a recent resurgence in interest and research has shown exciting opportunities for the future of vertical-axis wind turbines (VAWTs). Unique cyclical fluid physics results in additional complexity to VAWT blade aerodynamics. Unlike their horizontal-axis counterparts, the rotating blades of a VAWT produce varying torque depending on their location in the circular cycle. The aerodynamic relationship between the incoming wind flow and blade motion is such that the peak power is extracted when the blade and incoming wind are nearly perpendicular to each other during the windward side of the rotor. Recognizing this, the recently conceived dual-vertical-axis wind turbine (D-VAWT) extends a typical VAWT's windward region by having the blades rotate about two vertical axes. Introduced is a new path of purely rectilinear motion connecting the two axes, wherein the blade is designed to achieve optimal aerodynamic efficiency. Initial investigations into the D-VAWT's operation shows promising potential, with power coefficient values in the range of the most efficient VAWTs and even HAWTs. The current study seeks to further improve the performance of the D-VAWT through the incorporation of active blade pitch control throughout the blade path's distinct rotation and rectilinear regions. Computational fluid dynamics (CFD) is used to model a single-blade D-VAWT, and a user-defined method is devised to implement the blade pitch actuation as a function of cycle time location and blade centroid position. Numerical results reveal that strategic blade pitching can indeed increase performance in a specific region of the D-VAWT cycle, however the improvement can create undesired impacts on the flow field in other regions of the rotor. Emphasis is focused on the upstream and downstream flow interaction during active-pitch operation, offering important physical insight to the D-VAWT and VAWTs of similar geometric sizing.

Acknowledgements

There is a long list of people that have helped me either directly or indirectly over the course of this period of work, and I'd like to record my gratitude to a few of them here.

Firstly, I must acknowledge the guidance and patient support of my supervisor Dr. Marius Paraschivoiu. I would like to thank him for always reminding me to see the big picture and for easing my doubts on many occasions. I am also thankful of his understanding and encouragement with regards to my ambitions outside of the lab.

I'd like to thank my cohort of friends in the lab who I was lucky enough to work with over the past few years: Spencer Foley, Aierken Dilimulati, Jennifer Tan, Samson Victor, Gabriel Naccache, Patrick Larin, Farbod Vakilimoghaddam and Leslie Taylor. A special thanks is owed to Matin Komeili for his patience and willingness to share most-helpful insights during our many fruitful conversations on CFD and aerodynamics. Someone should erect a statue for Matin.

There's also a few of my close friends outside of the lab who I want to mention for their continual support and interest in this side of my life: Dylan Bridger, Kyle Logie, Adam Billard, Marie Malavaud, Marissa Bialowas, Micah Brown, and Sebastian Balk-Forcione. I really appreciate your thoughtfulness and understanding while I completed this project and didn't answer my phone.

Contemporary composer Philip Glass provided my academic soundtrack and kept my mind stimulated for hours on an end and all through the night. I am thankful for his music and would not have been able to complete this work without it.

Lastly, I'd like to thank my parents Laurie and Cheryl McLean for their selfless love and support not just during this endeavour but in everything I do. And have them always remember that I would be nowhere without them.

This thesis is dedicated to all the friends and family mentioned here.

Contents

List of Figures

List of Tables

Notation

A	Rotor swept area	[m^2]
AP	Active blade pitch	
c	Blade chord length	[m]
C_P	Power coefficient	
CAD	Computer-aided design	
CFD	Computational fluid dynamics	
D-VAWT	Dual-Vertical-Axis Wind Turbine	
F_x	Blade surface force in x-direction	[N]
F_y	Blade surface force in y-direction	[N]
F_N	Normal force	[N]
F_T	Tangential force	[N]
FP	Fixed blade pitch	
HAWT	Horizontal-Axis Wind Turbine	
l_o	Overset mesh edge length	[m]
l_u	Underset mesh edge length	[m]
M	Torque	[N m]
M_R	Torque during rotational region	[N m]
N	Number of blades	
p	Pressure	[Pa]
P	Extracted power	[W]
P_{wind}	Available aerodynamic power in wind	[W]
Q_∞	Freestream dynamic pressure	[Pa]
R	Rotor radius	[m]
Re	Reynolds number (blade velocity)	

S	Blade span	[m]
Δt	Time-step	[s]
TE-IN	Trailing edge inwards blade pitch angle	
TE-OUT	Trailing edge outwards blade pitch angle	
TSR	Tip speed ratio	
UDFF	User-defined field function	
$\boldsymbol{v}$	Velocity vector	[m/s]
V	Velocity magnitude	[m/s]
V_∞	Freestream wind speed	[m/s]
V_b	Blade tangential velocity	[m/s]
VAWT	Vertical-Axis Wind Turbine	
y^+	Dimensionless wall distance	
α	Blade angle of attack	[°]
λ	Tip speed ratio	
μ	Dynamic viscosity	[Pa s]
ω	Rotational velocity	[rad/s]
ϕ	Blade pitch angle	[°]
$\dot{\phi}$	Rate of blade pitch rotation	[rad/s]
ρ	Density of fluid	[kg/m^3]
θ	Azimuth angle	[°]

Chapter 1

Introduction

You don't need a weatherman to know which way the wind blows.

(Bob Dylan, 1965)

1.1 The Global Energy Revolution

Since the industrial revolution, modern civilization has been fuelled almost entirely by the finite resource known as fossil fuels. But the energy landscape is changing. Drastically.

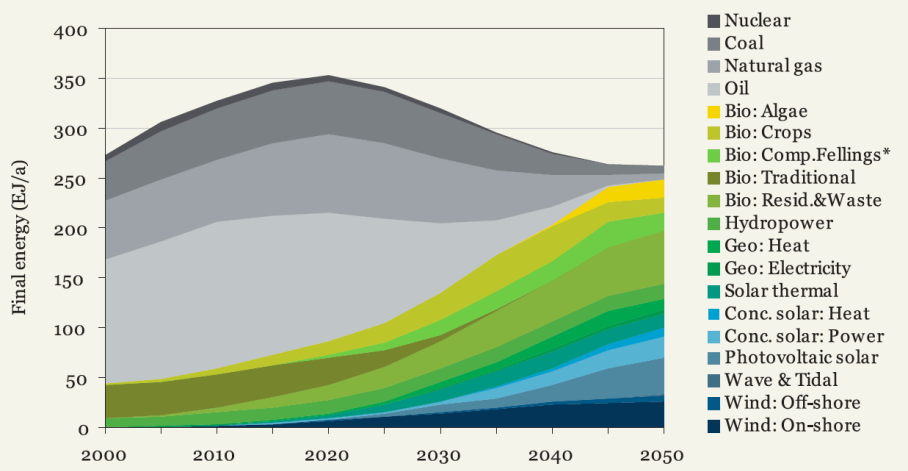

Figure 1.1: Energy distribution for WWF's 100% renewable scenario [1].

In the World Wide Fund for Nature (WWF) 2011 Energy Report, a completely realistic and achievable scenario is presented to transform the world to an energy make-up of 100% renewables by 2050 [1]. The scenario, although ambitious, is credible due to the fact that only existing and realistic technologies are employed, avoiding any unmerited hopefulness of potential future breakthrough

developments. Released in 2017, a consortium of scientists and researchers from around the world reinforced the pragmatism of the 2050 100% renewable shift by modeling and ranking the most effective (and existing) means of reducing greenhouse gases [2]. Presently, global investment and spending focus is shifting to facilitate this energy transition. In the 2017 edition of their World Energy Investment report, the International Energy Agency states that for the first time ever global spending on low-carbon electricity exceeded that of the oil and gas sector's, as the former's share rose to a record high of 43% [3].

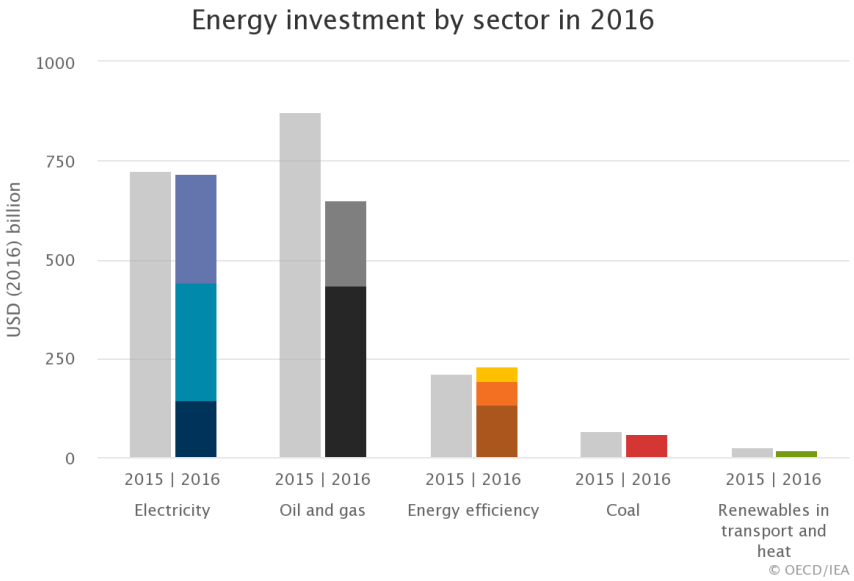

Figure 1.2: Energy investment breakdown by sector according to the 2017 World Energy Investment report [3].

Due to inherent characteristics, some forms of renewable energy are less consistent than the traditional fossil fuel scheme. That is, depending on the region of the world and the time of day, the sun may not be shining and the wind may not be blowing. Therefore, when discussing the renewable energy landscape of the future, it is important to recognize that the energy makeup must indeed be a *mix*. This notion of the renewable energy economy being a diverse one is well-established, as clearly shown by Figure 1.1. There are also a multitude of scholarly initiatives being undertaken to understand the conglomerated green energy system, such as the proposed North-East Asian super grid [4] and understanding the effects of the 100% renewable scenario on the European Union [5]. A crucial contributor to the developing renewable mix is wind energy, which is one of the most exciting and rapidly growing sources of green electricity today.

1.2 The Role of Wind Energy

Wind energy is one of the oldest forms of renewable energy, a fact easily understood by considering the fundamental common sense behind harnessing the perennial energy available in the freely flowing wind. Up until very recently, wind energy has been classified as somewhat of a niche market with limited widespread commercial applicability. Brought about in large part by the oil embargoes and energy crisis of the time, wind energy began its industrial-scale research and development in earnest in the early 1970s [6]. By 2017, any perceived immaturity in the wind power industry has been outgrown, with wind farms being constructed for the first time in history without any government subsidy [7].

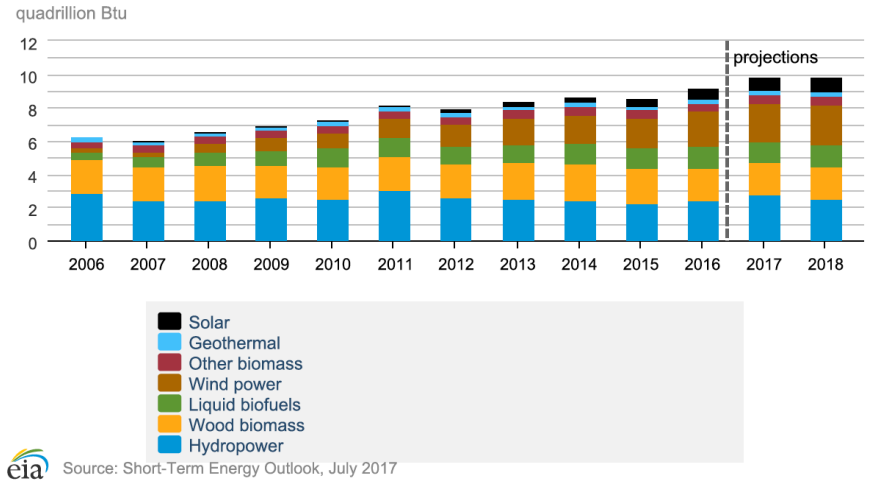

Figure 1.3: Renewable energy predictions for the U.S. [8].

Moving forward, wind energy will continue to increase its contribution to economies around the world. In the United States, wind power is now becoming the dominant form of renewable energy and its growth is projected to continue well into the next decade [8, 9]. In Canada, wind power represented 6% of the country's total electricity production in 2016, or the equivalent of three million homes. Annual cumulative installed capacity in the country has experienced growth at the exponential rate shown in Figure 1.4, and is expected to continue with an additional 700 MW planned for 2017 [10].

Although encouraging growth is currently being seen in North America and especially in Europe, further technological development is required to push wind power generation towards deep market penetration. As the most favourable wind locations are sought out and developed, increasingly clever and robust turbine designs will be needed to harness the wind in more challenging locations.

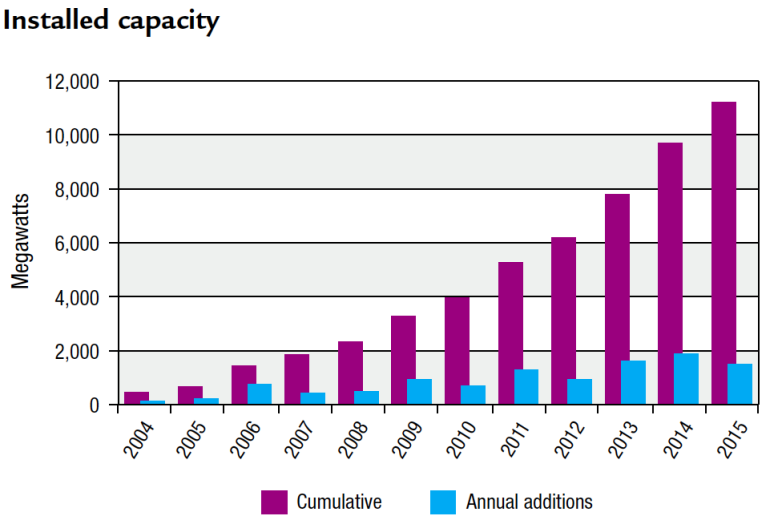

Figure 1.4: Installed wind energy capacity in Canada [11].

1.3 Wind Turbine Technology

Historically, at a high-level, wind turbines can be classified in two broad categories: horizontal and vertical axis turbines. The blades of the former rotate about an axis parallel to the incoming (horizontal) wind, while the rotational axis of the latter is perpendicular to the wind. Under the umbrella of axis classification, a plethora of designs exist and new concepts are constantly being explored and developed. Since the current investigation pertains to the development of a new type of vertical axis turbine, the brief theoretical background will be limited to this type.

1.3.1 Aerodynamic Fundamentals

Lift-based wind turbines[1]— regardless of axis orientation — make use of airfoil-shaped cross sectional blades to generate a pressure differential that consequently leads to an unbalanced force and motion. The forces generated over an airfoil due to the passage of flow are shown in Figure 1.5, where V_∞ is the incoming (freestream) wind speed, α is the blade's angle of attack, c is the blade's chord length, L & D are the lift and drag forces, respectively, and N & A are the normal and axial (or tangential) forces, respectively. The relationship between the lift & drag forces and the normal & tangential forces is provided in Section 3.1.

The freestream wind velocity, V_∞, is related to the turbine's rotational velocity using the non-

[1]Drag-based turbines, known as Savonius turbines, rely solely on the drag force over their blades to push them into a state of rotation. They are fundamentally quite different and aerodynamically less efficient than their lift-based counterparts, and are not discussed further in the present text.

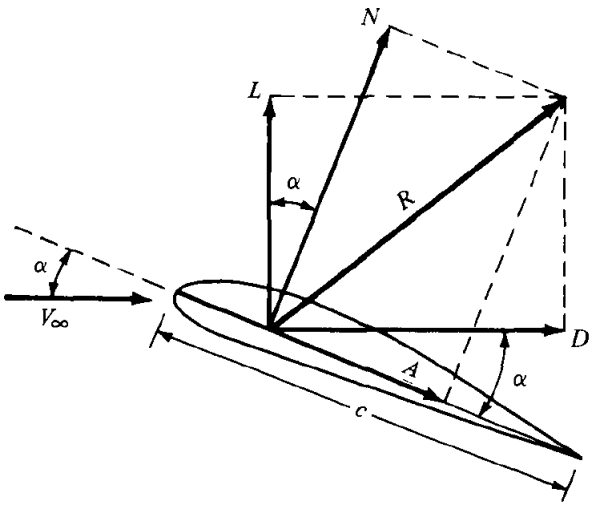

Figure 1.5: Airfoil aerodynamics [12].

dimensional quantity known as the *tip speed ratio* (TSR) [13]:

$$\lambda = \frac{V_b}{V_\infty} = \frac{\omega R}{V_\infty}, \tag{1.1}$$

where V_b is the tangential velocity of the blade, ω is the rotational velocity of the turbine, and R is the rotor radius of the turbine. At a given TSR and operating conditions, turbine performance is measured using the non-dimensional *power coefficient*:

$$C_P = \frac{P}{\frac{1}{2}\rho A V_\infty^3}, \tag{1.2}$$

where P is the turbine's power output, ρ is the air density, A is the rotor swept area, and V_∞ is the incoming freestream wind velocity. The turbine's aerodynamic power output is given by fundamental physics using:

$$P = M\omega = (F_T R)\omega, \tag{1.3}$$

where M is the rotor's torque or moment and F_T is the force in the tangential direction of blade motion. Equation 1.3 demonstrates that for a vertical-axis wind turbine it is the tangential force, not simply the lift force, that is ultimately responsible for the turbine's performance. The understanding of the relevant forces generated and their impact is an essential part of wind turbine design and is a focus of the current work.

1.3.2 Vertical-Axis Wind Turbines

While horizontal axis turbines currently hold a dominate position in the world marketplace, vertical axis machines still provide a number of distinct advantageous design characteristics. The specific type of VAWT known as the Darrieus H-rotor, seen in Figure 1.6, presents several notable advantages including the housing of heavy equipment (e.g. gearbox, generator) at the base of the structure, reduced aerodynamic noise due to lower rate of blade rotation, and simplicity of manufacturing for uniform straight blades [14]. Advantageous characteristics lead to unique opportunities, such as the potential for VAWTs to play an important role in decentralized energy requirements and standalone direct mechanical drive applications [15].

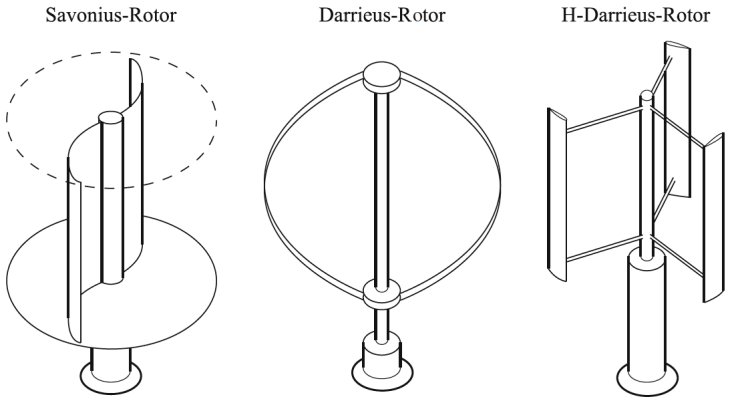

Figure 1.6: Standard types of vertical-axis wind turbines [13].

One of the main issues with VAWTs is their aerodynamic complexity. Figure 1.7 is a schematic of the velocity and force vectors associated with the blade of a VAWT during its rotation. In the schematic, θ is the blade azimuth angle position, α is the geometric blade angle of attack, ϕ is the blade pitch angle, δ is the effective blade angle of attack, and V_{rel} is the relative wind speed acting on the blade. The difficulty with regards to aerodynamics arises with the fact that both the velocity and force vectors are constantly changing as a function of blade azimuth position. This can lead to a highly variable force loading on the blade and overall rotor, which not only leads to fluctuation in power production but also to cyclical loading and indeed the potential for fatigue failure [13]. Fortunately, the difficulties present in VAWT engineering design are not unsurmountable and are currently being overcome as a result of the renewed interest in this area of research. Promising and novel investigations are being undertaken to discover the next generation of vertical-axis wind turbines, such as an exciting category of large offshore floating VAWTs up to 20 MW in size [16].

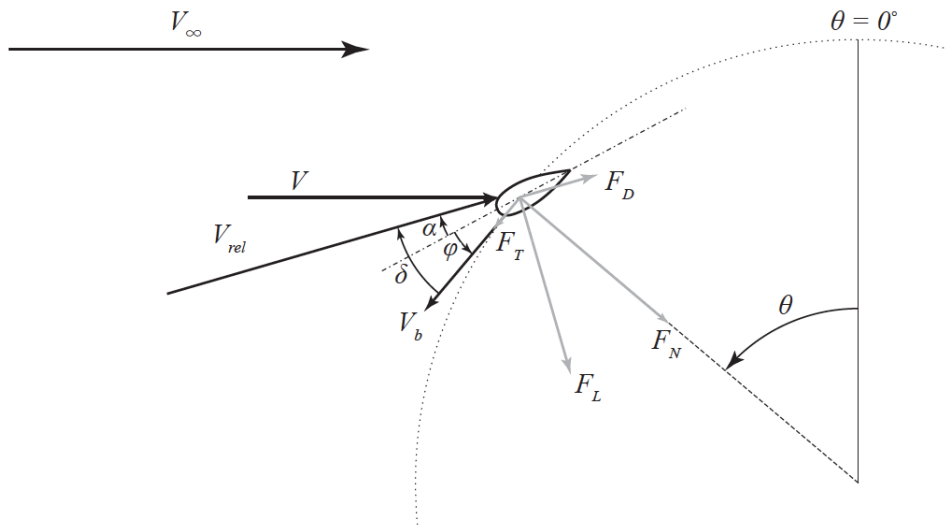

Figure 1.7: Vertical-axis wind turbine blade path velocity and force definitions. Adapted from Dyachuck et al. [17].

1.3.3 The Dual-Vertical-Axis Wind Turbine

As introduced in Section 1.3.2, the aerodynamic forces present on the blade of a VAWT are highly dependent on its azimuth position in the rotor's cycle. It has been shown that for a VAWT in standard operating conditions (i.e. those typical of useful power production), the turbine produces peak power when the upstream blade and incoming wind are nearly perpendicular to each other [18–20]. This phenomenon is depicted in Figure 1.8, which is a key result of the VAWT investigation performed by Paraschivoiu et al. [18]. Here the peak in positive blade torque is clearly seen in the 90° azimuth region, or when the blade's chord line is perpendicular to the incoming flow direction.

First explored by Naccache [21], the dual-vertical-axis wind turbine, or D-VAWT, exploits this position of peak aerodynamic performance unique to VAWTs. By having the blade rotate around *two* axes instead of the traditional one, the upstream region of 90° blade azimuth position is essentially extended as the blade travels linearly between the two axes. The extension of the optimal blade position region is described schematically in Figure 1.9a, where a *translation* region is now present as a result of the novel two axes design. A 3D-CAD model of a possible D-VAWT conceptual design is provided in Figure 1.9b[2]. It is envisioned that some sort of rail or cable mechanism could be implemented to achieve the unique blade motion — similar in principle to that of a ski lift. The actual mechanism, structure, and generator system for the D-VAWT is out of the scope of the current analysis.

[2]Note that this schematic is purely conceptual and for understanding purposes only.

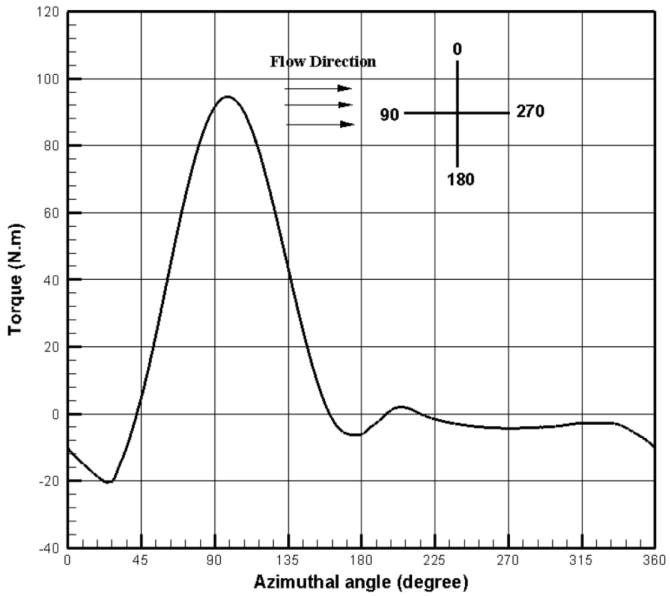

Figure 1.8: Blade torque as a function of azimuth position for a turbine operating at TSR $\lambda = 3$ [18].

1.4 Motivation of Current Work

The preliminary research and development work undertaken thus far on the D-VAWT has yielded promising results, with the turbine achieving predicted coefficient of power values in the range of the most efficient VAWTs and even HAWTs [21]. Having been only very recently conceived, the D-VAWT is an exciting opportunity for design exploration and improvement. Referring to Figure 1.8, the torque experienced by a VAWT blade changes drastically throughout the cycle — so much so that at points a negative torque is experienced[3]. This is especially relevant to the downstream (azimuth angle $\theta > 180°$) region. The D-VAWT blade torque profile is not immune to this, which is largely a result of so much of the incoming wind's energy being extracted by the blade during the upstream ($0° < \theta < 180°$) half of the cycle. This is particularly interesting for the D-VAWT, since now an extended translation region of the blade exists with the blade at a quasi $\theta = 270°$ downstream azimuth angle position. The primary focus of the current investigation is to improve on the aerodynamic performance of the D-VAWT by alleviating any regions of negative torque and potentially creating a region of secondary notable power extraction in the downstream translation path.

[3]A negative torque essentially means that the resultant tangential force acting on the blade is opposing the direction of motion along the cycle path.

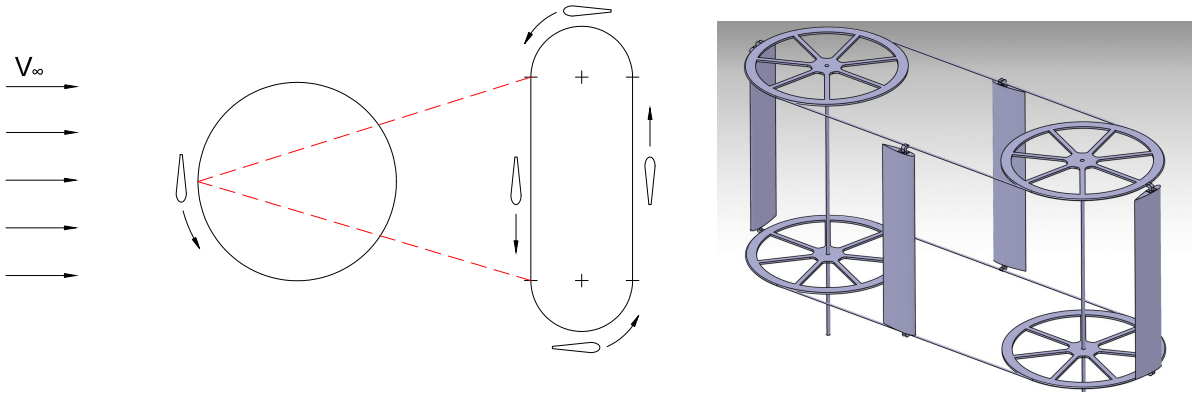

(a) The D-VAWT's extension of the blade's azimuth $\theta = 90^{\circ}$ position.

(b) Conceptual model [21].

Figure 1.9: The dual-vertical-axis wind turbine concept.

1.5 Literature Review

As part of the ongoing research effort to develop competitive VAWT technologies, a tremendous amount of work is being completed by research institutions across the globe. Presented first is a very brief summary of some pertinent topics to using computational fluid dynamics with VAWTs, which is then followed by a more specific review of the most relevant contributions relating to the topic under consideration.

1.5.1 CFD Considerations for VAWT Simulation

Computational fluid dynamics (CFD) involves the approximation of a real, continuous physical domain with a set of finite, discrete numerical sub-domains (known as elements or nodes). The flow field is computed by the CFD solver's interpretation of partial differential equations and physical models, with significant user expertise and knowledge required to establish an appropriate simulation environment. Although still susceptible to errors and spurious results, CFD is advantageous compared to the experimental approach in its accessibility, flexibility, and cost [22].

A comprehensive study specifically on Darrieus-type VAWT simulation using CFD was recently completed by Balduzzi et al. [23]. The thoroughness and direct relevancy of this study offers a number of key findings that are used in the development of the current CFD environment:

- A sufficiently large domain size is imperative to ensure artificial blockage effects are not

present in the solution. Figure 1.10 shows this effect, where attention should be drawn to the velocity vectors inappropriately reaching the domain boundaries for cases (B) and (C).

- The time-step size should in general increase proportionally with TSR, with very small time-steps (smaller than 0.25° of incremental rotation per step) required for low TSRs. However, if accurate flow separation and vorticity propagation is desired, a small time-step should be used regardless of TSR value.

- The coupled flow algorithm is preferred over the segregated *SIMPLE* on account of robustness and insensitivity to angular time-step.

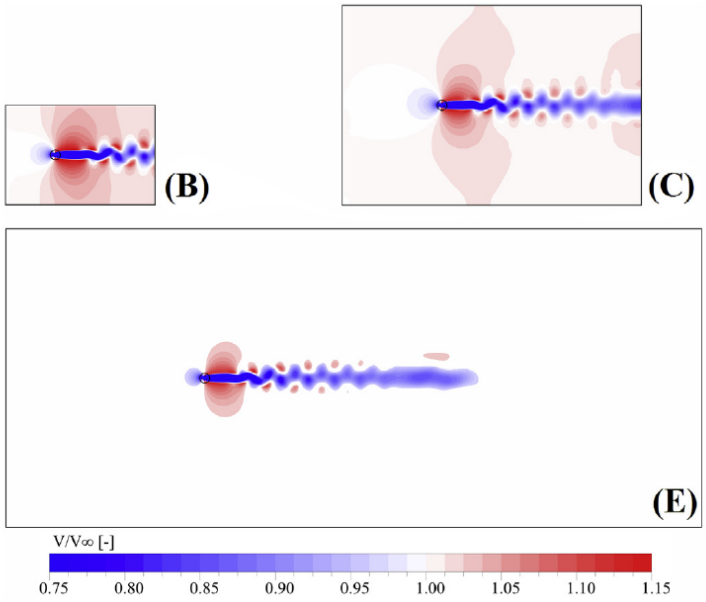

Figure 1.10: Non-dimensionalized velocity contours for CFD domains of varying overall size [23].

Turbulence remains one of the most complicated features of not only fluid dynamics, but of all classical physics. To represent turbulence numerically or mathematically, no universal theory exists — instead, there are a *number* of theories that have been developed in an effort to predict statistical values of the flow field [24]. These theories, or semi-empirical models, are based on the introduction of additional equations into the fundamental governing ones to represent the effects of turbulence[4]. The *modeling* of turbulence is indeed one of the most important aspects of CFD simulations in general, and especially crucial for VAWT investigations where the flow can be highly turbulent in the rotor area and downstream of it.

[4]This is elaborated on with more mathematical detail in Section 2.1.

With the current stage of the evolution of computational power, two-equation turbulence models have become the norm for the majority of average CFD simulations. Wilcox has shown that the two equation $k-\omega$ turbulence model is superior to the $k-\varepsilon$ model in flows with adverse pressure gradients and turbulent boundary layers [25]. An adverse pressure gradient is exactly the type of flow encountered over the blade of a vertical-axis wind turbine, which makes the $k-\omega$ model a more reliable choice for accurate boundary layer (and thus aerodynamic) predictions. However, the ω-equation by itself is known to possess sensitivity to values of the specific dissipation rate (ω) in the freestream and boundary conditions [26]. To address this issue, a notable improvement to the standard Wilcox model is attributed to the work of Menter [27]. Menter's shear-stress transport (SST) approach uses blending functions to essentially model the turbulence using $k-\varepsilon$ in the far-field flow and $k-\omega$ near the wall and inside the boundary layer. Thus, the advantages of both models are incorporated into the formulation, which has made the $k-\omega$ SST turbulence model the current industry standard for aerodynamic applications with flow separation.

A justified debate in the CFD modeling of VAWTs is the choice of a 2D, mid-plane approach or that of a full 3D analysis. The latter, while naturally being the more realistic representation of the physical situation, can be extremely computationally expensive for even simple geometries. Since wind turbines in general use long and slender blades, the spanwise velocity component of the flow is relatively small and thus the 2D aerodynamics are still of great practical interest [28]. As such, a number of applications exist in VAWT CFD modeling where the analysis is limited to 2D. However, if truly realistic power prediction values are desired, there is no substitute for a fully three-dimensional analysis. The over-prediction of power coefficient by 2D CFD simulations is a known issue, and is clearly shown by Howell et al. in their study of a small VAWT [29]. In that particular study, values of power coefficient for 2D simulations were as much as two times greater than those of 3D simulations under the same conditions.

1.5.2 Dynamic Stall

The variation in blade loading alluded to in Section 1.3.2 is a direct result of the variation in angle of attack experienced by the blade over the course of its cyclic path. The severity of the change in angle of attack is essentially a function of tip speed ratio (λ) and blade azimuth angle (θ) [20]:

$$\alpha = \arctan\left(\frac{1}{\lambda\ \sin(\theta)} + \frac{1}{\tan(\theta)} + \theta - \frac{\pi}{2}\right), \tag{1.4}$$

where in Equation 1.4 the blade angle of attack and all other angles are given in radians. Equation 1.4 can be used to display a revealing and somewhat concerning relationship between the tip speed ratio, blade azimuth angle, and blade angle of attack. Figure 1.11 demonstrates this for a typical range of TSRs for vertical axis wind turbines.

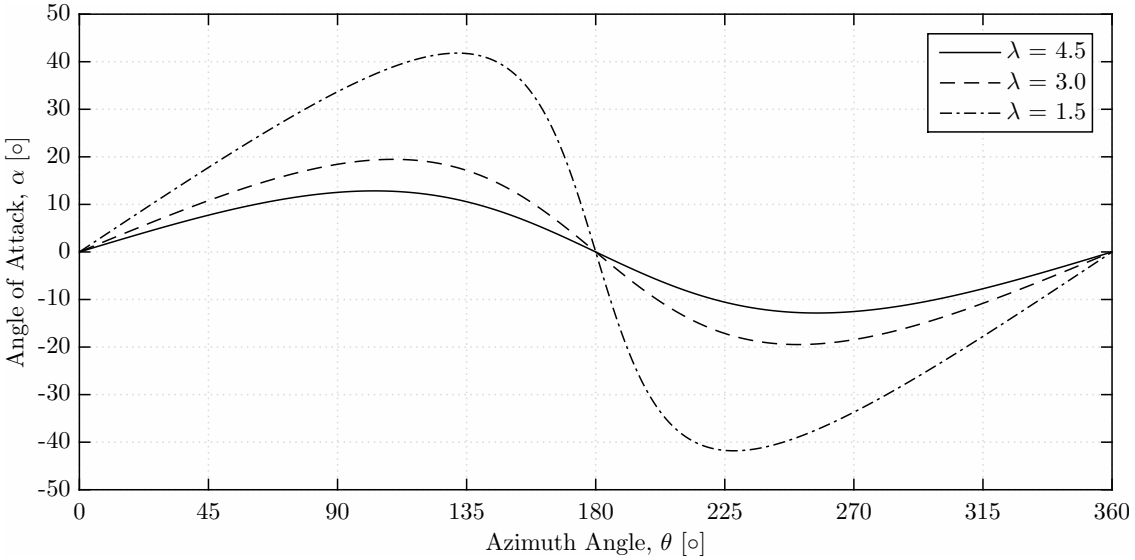

Figure 1.11: The dependance of cyclical VAWT blade angle of attack on TSR.

Observing Figure 1.11, it is quickly seen how the magnitude of cyclical angle of attack increases drastically with decreasing TSR. In an experimental study performed by Gerakopulos et al. [30], the static stall angle for a NACA0018 airfoil at a Reynolds number of 2×10^5 is determined to be 14°. This is a typical range of stall angle for symmetrical VAWT airfoils, and its comparison with the angles seen in Figure 1.11 is justification for the importance of the dynamic stall consideration. Consequently, for turbines operating at these low tip speed ratios, dynamic stall is arguably the most important flow feature to understand.

Insightful physical explanation of dynamic stall in VAWTs is offered by Ferreira et al. [31]. In this study, experimental particle image velocimetry (PIV) data is used in conjunction with CFD to explore the operation of a NACA0015 airfoil-based turbine operating in dynamic stall at TSR $\lambda = 2$. It is shown that dynamic stall acts as a source for two regimes of strong vortex shedding: one due to leading edge separation with a vortex shedding motion in the *same* direction as the rotor's rotation, and a second due to the roll up of vorticity at the trailing edge in the *opposite* direction of rotor rotation. These two distinct regions of vorticity are depicted in Figure 1.12, which is extracted from a related study of Ferreira et al. [32].

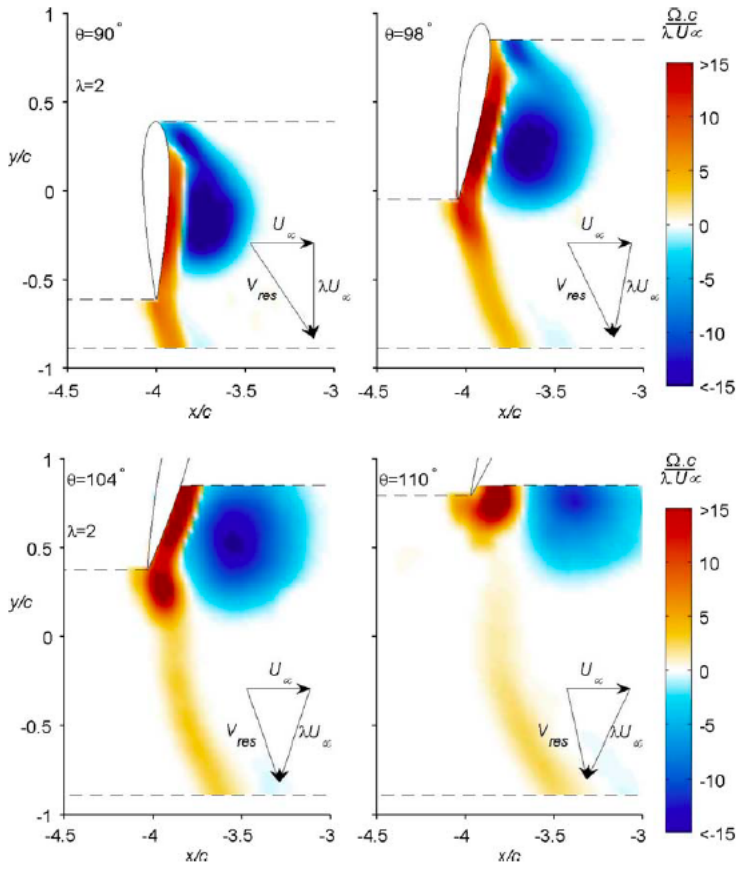

Figure 1.12: Development of separate vorticity roll-up at leading and trailing edges [32].

Ferreira et al. determined the detached-eddy simulation (DES) approach to be the most suitable turbulence model for recreating the complex vorticity field during dynamic stall [31]. In fact, both URANS[5] models tested, namely the one equation Spalart-Allmaras and two equation $k-\varepsilon$ models, proved unsatisfactory for this application. An analysis on dynamic stall in VAWT blades by Qin et al. [33] also makes use of a turbulence model from the k–ε family, although this time the more robust *RNG* $k-\varepsilon$ variant is chosen. For reasons provided in Section 1.5.1, the use of ε-based turbulence models to simulate VAWT flow with dynamic stall — flow that is by definition subject to extensive separation — seems to be a plausible source of error in the previously conducted URANS CFD modeling for this application. It is acknowledged here, however, that until recently the ε-based turbulence models were certainly the most often used in CFD analysis, with the advantages of ω-based approaches becoming established only as of late [25].

[5]URANS is an acronym for the Unsteady Reynolds-Averaged Navier-Stokes equations, which are described in Section 2.1.

1.5.3 Blade Pitch Control

Referencing Figure 1.7, the blade pitch angle, ϕ, is the degree of rotation applied to the blade about its own geometric axis, essentially creating an offset between the blade chord line and the tangent line of rotation. As a sign convention, a blade pitch that causes the trailing edge of the blade to rotate towards the center of rotor rotation is described as a negative pitch angle, and henceforth referred to as "TE-IN." Similarly, a pitch rotating the trailing edge outwards from the center of rotation is labeled "TE-OUT" and has a positive pitch angle.

Historically, the Darrieus vertical-axis turbine is a fixed-pitch machine. This is a notable difference between VAWTs and HAWTs, with the latter virtually always having a pitch mechanism to orient the blades to optimal angles of attack based on the incoming wind conditions. However, the recent resurgence into commercial H-Darrieus research has sparked investigation into having the blades on these turbines either actively (through an actuator mechanism) or passively (through incoming wind and cycle position) pitch during operation. The main goal of blade pitching in the case of a VAWT is to mitigate regions of negative torque and to also reduce the cyclic loading known to lead to fatigue failure in large-scale vertical axis turbines [34].

During the Sandia National Laboratories VAWT research campaign of the 1980s [35,36], testing was done on a 5 m, 3-blade, NACA0015 airfoil Darrieus turbine with 15.24 cm chord length and solidity $\sigma = 0.22$. Klimas and Worstell demonstrate that for a classic Darrieus turbine, with average blade Reynolds number of 3.5×10^5 , the power coefficient can be improved with a fixed-pitch angle of $\phi = -2°$, while it is degraded for all TE-IN angles beyond $\phi = -2°$ and all positive TE-OUT angles. The physics behind the efficacy of a fixed-pitch TE-IN or TE-OUT angle is observed in the experimental study from Armstrong et al. [37]. Here it is shown that for a turbine operating at TSR $\lambda = 1.6$ with a fixed-pitch offset, power coefficient improvement is experienced for TE-IN angles up to $\phi = -6°$. This is explained by the reduction in angle of attack in the upstream portion, thus delaying potential stall; followed by the increase of angle of attack in the downstream half of the cycle, where for zero blade pitch the angle of attack is normally far too small to produce meaningful tangential force. Important to note here is that for a given TSR, power coefficient improvement occurs for TE-IN fixed-pitch angles only up to a certain limit — that is, there is a critical negative pitch angle where beyond which the turbine performance *decreases*.

In their thorough parametric study on H-Darrieus VAWTs, Gosselin et al. considered blade pitch angle as one of the parameters of their CFD investigation [20]. Figure 1.13 shows the remarkable

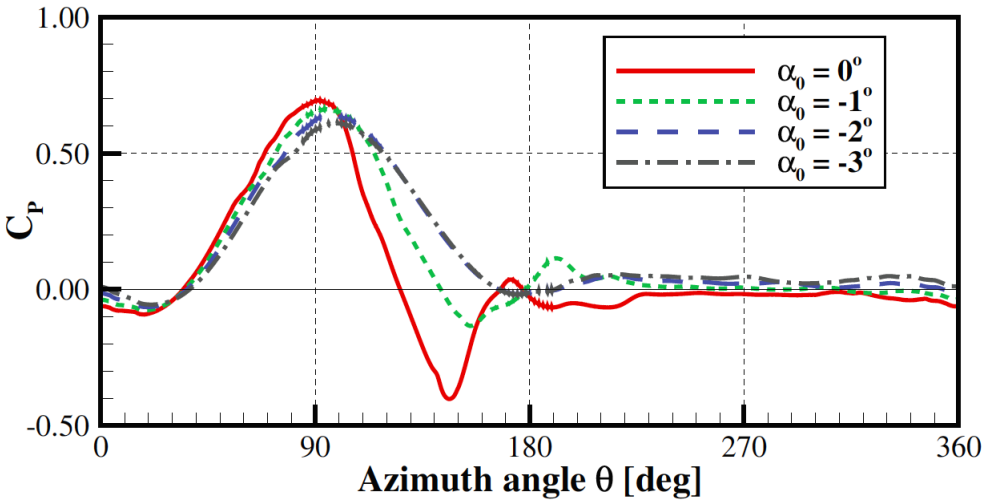

Figure 1.13: The effect of (TE-IN) blade pitch angle on instantaneous power coefficient at TSR $\lambda = 3$ [20].

improvement that is seen for the downstream performance of the blade, with any regions of negative torque being virtually eliminated for pitch angles of -2° and -3°. While this is a promising result, the pitch angle analysis of Gosselin and others in literature are primarily for tip speed ratios of $\lambda \leq 3$. Contemporary blade pitch angle investigations for higher TSR VAWTs appears to be a potential gap in the current library of literature.

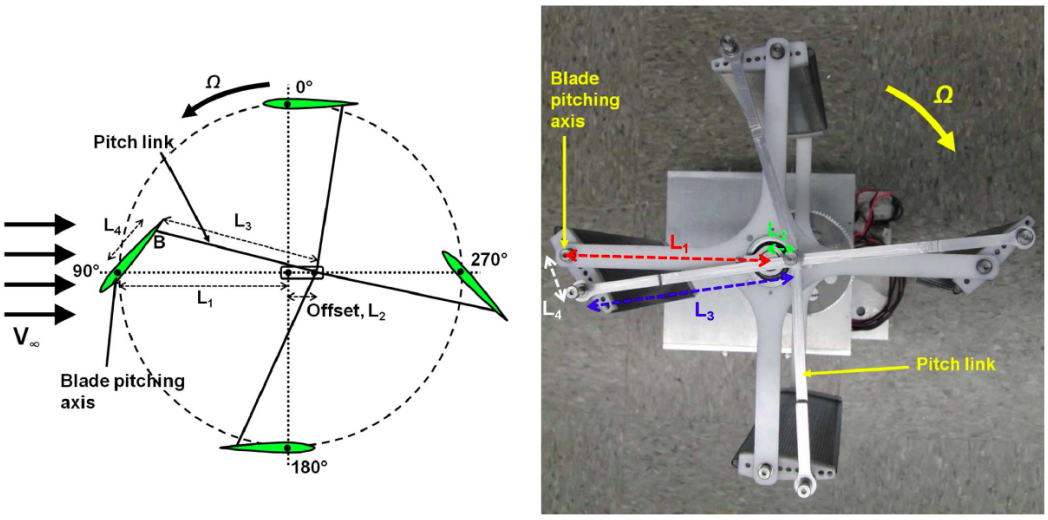

Figure 1.14: A novel passive variable pitch control mechanism based on a four-bar linkage [38].

A practical application of dynamic blade pitch variation for a VAWT is presented in the recent study of Benedict et al. [38]. A prototype VAWT was constructed with a novel passive blade

pitch mechanism as described in Figure 1.14, where the blade pitch is enacted naturally as only a function of the rotor's cyclic position. Furthermore, the pitch phasing — i.e. the azimuth position of the cycle where positive and negative pitching occur — reacts instantaneously to incoming wind direction, thus maximizing its effect. This is an important development, as it demonstrates the viability and potential for implementing effective, low power input pitch mechanisms in VAWTs of the next generation.

1.6 Scope

The remainder of the thesis is a presentation of the work completed to develop an accurate CFD model to predict the performance of the D-VAWT with active blade pitch control. Chapter 2 explains the general modeling approach implemented along with the theory and justification behind each decision. The following chapter is a validation of the computational methodology using experimental VAWT data. Chapter 4 presents the CFD results of the baseline 1-blade D-VAWT case. Finally, Chapter 5 is the investigation of the 1-blade D-VAWT with active pitch control. As a reference of interest and resource for future researchers, an appendix is included for start-up considerations and all developed user code is provided at the end of the thesis.

Chapter 2

Computational Methodology Considerations

A prerequisite to any computational investigation is a proficient understanding of the underlying theory such that a suitable approach is employed to model the given flow physics of the scenario. The fundamental equations of fluid mechanics are provided here, as well as the most important CFD considerations required to solve said equations. A relatively new and advantageous offering in commercial CFD packages is the overset mesh technique, whose description is provided herein and can be used as a useful reference to future researchers.

All simulations of the current investigation are performed using the commercial finite volume-based package STAR-CCM+ from Siemens PLM Software (formerly CD-adapco) [39], and ran locally on 4-core, Intel i7 processors.

2.1 Governing Equations

Fluid mechanics involves a set of powerful fundamental equations that govern the motion of fluid flow. The concept of *computational* fluid dynamics is to provide a means of solving the governing equations, which due to their complexity and non-linearity cannot be handled analytically except for the most simple of cases.

2.1.1 Fundamental Fluid Mechanics

The fundamental equations in the field of fluid mechanics are well-established, and are essentially applications of the conservation laws of classical physics to fluid flow. Compressibility is a consid-

eration of whether a fluid's density changes throughout the flow field or in time — a consideration of whether density can be treated as a constant or another solution variable. The treatment of density has a direct impact on the form of the governing equations of fluid mechanics, and thus also impacts the CFD approach to solve said equations. For reasons described in detail in Section 3.1.2, the *compressible* form of the governing equations are implemented in the current CFD environment. Instead of specifying the fluid's density to be an absolute constant, allowing the solver to determine the density produces a much 'smoother' computational solution. To reproduce the equations here, the STAR-CCM+ theory guide [39] is used to present the equations as they appear in the CFD solver, while the insightful explanations of the equations by Anderson [40] provide a fruitful reference for physical understanding and derivation.

Conservation of Mass

Using a fixed elemental volume frame of reference, the equation for the conservation of mass — or the *continuity* equation as it is known for fluids — in *conservation* form is given by:

$$\frac{\partial \rho}{\partial t} + \boldsymbol{\nabla} \cdot (\rho \boldsymbol{v}) = 0, \tag{2.1}$$

where ρ is the fluid density, $\boldsymbol{v}$ is the fluid velocity vector (in the x-, y-, and z-directions for the Cartesian coordinate system), and $\boldsymbol{\nabla}\cdot$ is the divergence operation. As shown by Equation 2.1, the fluid density and its velocity are directly included in the conservation of mass. Consideration of momentum is required to incorporate pressure.

Conservation of Momentum — The Navier-Stokes Equation

Newton's second law, written with the intent to represent the change in linear momentum, is given by [22]:

$$\frac{d}{dt}(m\boldsymbol{v}) = \boldsymbol{F}, \tag{2.2}$$

where m is the particle mass, $\boldsymbol{v}$ is the velocity vector, and $\boldsymbol{F}$ is the resultant force due to shear and body forces. To address the case of an infinitesimal fluid volume, Equation 2.2 is manipulated to replace the fluid element's mass with density (via a division by volume) and replacing the left-hand side with the material derivative. The right-hand side of the original 2nd law equation is broken

into the forces due to stresses, and those due to external sources (also known as body forces):

$$\frac{\partial(\rho \boldsymbol{v})}{\partial t} + \nabla \cdot (\rho \boldsymbol{v} \otimes \boldsymbol{v}) = \nabla \cdot \boldsymbol{\sigma} + \boldsymbol{f_b}, \tag{2.3}$$

where $\boldsymbol{v}$ is the velocity vector, $\otimes$ is the Kronecker product, $\boldsymbol{\sigma}$ is the stress tensor, and $\boldsymbol{f_b}$ encompasses the body forces (such as gravity).

The complexity arises with the shear or surface forces, which are caused by internal pressure and friction forces within the fluid. Expanding the stress tensor, $\boldsymbol{\sigma}$, to show these two constituents gives:

$$\frac{\partial(\rho \boldsymbol{v})}{\partial t} + \nabla \cdot (\rho \boldsymbol{v} \otimes \boldsymbol{v}) = -\nabla \cdot (p\boldsymbol{I}) + \nabla \cdot \boldsymbol{\tau} + \boldsymbol{f_b}, \tag{2.4}$$

where p is pressure, $\boldsymbol{I}$ is the identity tensor, and $\boldsymbol{\tau}$ is the *viscous* stress tensor. For a Newtonian fluid, the viscous stress tensor is given by the relation:

$$\boldsymbol{\tau} = 2\mu \boldsymbol{S} - \frac{2}{3}\mu (\nabla \cdot \boldsymbol{v}) \boldsymbol{I}, \tag{2.5}$$

where μ is the (assumed constant) *molecular* dynamic viscosity, and $\boldsymbol{S}$ is the rate of strain tensor defined as:

$$\boldsymbol{S} = \frac{1}{2}\left(\nabla \boldsymbol{v} + (\nabla \boldsymbol{v})^T\right). \tag{2.6}$$

Combining the definition of the viscous stress tensor given in Equation 2.5 and the momentum relationship of Equation 2.4 gives the Navier-Stokes equation in conservation form, using compact vector notation:

$$\frac{\partial(\rho \boldsymbol{v})}{\partial t} + \nabla \cdot (\rho \boldsymbol{v} \otimes \boldsymbol{v}) = -\nabla \cdot (p\boldsymbol{I}) + \nabla \cdot \left[2\mu \boldsymbol{S} - \frac{2}{3}(\nabla \cdot \boldsymbol{v}) \boldsymbol{I}\right] + \boldsymbol{f_b}. \tag{2.7}$$

Conservation of Energy

Additional physical modeling is required in the numerical approach if the Navier-Stokes equation given as Equation 2.7 is used. This is mainly a question of whether the flow scenario under consideration involves a constant fluid density, or if the density is instead a function of pressure and temperature. If the latter is true, a third conservation equation is required to provide a means of computing the fluid's internal energy, which is then used to determine temperature via an equation of state [41]. The conservation of energy, or the first law of thermodynamics, applied

to an elemental volume of fluid is given in conservation form as:

$$\frac{\partial(\rho E)}{\partial t} + \nabla \cdot (\rho E \boldsymbol{v}) = \boldsymbol{f_b} \cdot \boldsymbol{v} + \nabla \cdot (\boldsymbol{v} \cdot \boldsymbol{\sigma}) - \nabla \cdot \boldsymbol{q} + S_E, \tag{2.8}$$

where E is the total energy per unit mass, vector field $\boldsymbol{q}$ is the heat flux due to thermal conduction, and S_E is the rate of volumetric heat addition or energy source. The heat flux, $\boldsymbol{q}$, is described by Fourier's conduction law [22], which states that the heat transferred through thermal conduction is proportional to the temperature gradient:

$$\boldsymbol{q} = -\kappa \nabla T, \tag{2.9}$$

where T is the temperature field and the constant of proportionality, κ, is the coefficient of thermal conductivity.

Associated with the conservation of energy is an equation of state, which gives a relationship between fluid properties pressure, density and temperature. The ideal gas model is usually a suitable approximation for aerodynamic applications [40], and is given by:

$$\rho = \frac{p}{RT}, \tag{2.10}$$

where R is the specific gas constant. The three conservation equations and associated equation of state are the basis for the physical compressible flow model to be solved by the CFD software. However, additional equation manipulations and simplifications are usually[1] required to obtain the flow field's solution for realistic applications.

2.1.2 The Reynolds-Averaged Navier-Stokes Equations

The governing fluid mechanics equations presented in Section 2.1.1 are the most general mathematical relationships for the conservation of mass, momentum, and energy. In all but a very limited number of scenarios, real-world fluid flow is turbulent. A flow's transition from laminar to turbulent presents serious complications to its mathematical representation and prediction, stemming from the fluctuating and inherently random nature of turbulent flow. Under turbulent conditions, a

[1] The unadulterated fundamental equations can indeed be solved with the CFD technique known as direct numerical simulation (DNS). The enormous computational cost of DNS makes it currently prohibitive as a practical tool for obtaining CFD solutions to real-world problems such as external aerodynamics.

flow's velocity must be considered as the sum of a mean value, $\overline{v_i}$, and a fluctuating value, v_i', [25]:

$$v_i = \overline{v_i} + v_i', \tag{2.11}$$

or, for a general solution variable, γ, [39]:

$$\gamma = \overline{\gamma} + \gamma'. \tag{2.12}$$

Turbulence's requirement to describe flow variables in terms of a mean and fluctuating value cause the fundamental equations to be adjusted accordingly. A common way in CFD applications of accounting for the implications of turbulence is to use the *time*-averaged form of the fundamental equations, which is known as the Reynolds-Averaged Navier-Stokes (RANS) approach to turbulence modeling.

Replacing the flow variables of the conservation of mass (Eq. 2.1) with the time-averaged variable decomposition (Eq. 2.11) results in the following expression:

$$\frac{\partial \rho}{\partial t} + \boldsymbol{\nabla} \cdot (\rho \overline{\boldsymbol{v}}) = 0. \tag{2.13}$$

Comparing Equation 2.13 with Equation 2.1, it can be seen that the only difference is the replacement of the general velocity vector with the *mean* velocity vector. Introducing the velocity decomposition of Equation 2.11 into the conservation of momentum (Eq. 2.4), following algebraic simplifications, produces the RANS momentum equation:

$$\frac{\partial (\rho \overline{\boldsymbol{v}})}{\partial t} + \nabla \cdot (\rho \overline{\boldsymbol{v}} \otimes \overline{\boldsymbol{v}}) = -\nabla \cdot (\overline{p} \boldsymbol{I}) + \nabla \cdot (\boldsymbol{\tau} + \boldsymbol{\tau_t}) + \boldsymbol{f_b}. \tag{2.14}$$

Careful inspection is required when comparing Equation 2.14 and Equation 2.4. As expected, all pressure and velocity terms are replaced with their mean value equivalents. However, a new term is now apparent alongside the viscous stress tensor (defined in Equation 2.5). This new tensor — known as the '*Reynolds* stress tensor' — is due to the interactional effect the fluctuating velocity components have on the fluid's momentum. In three-dimensions, the Reynolds stress tensor, $\boldsymbol{\tau_t}$, is defined as:

$$\boldsymbol{\tau_t} = -\rho \begin{pmatrix} \overline{u'u'} & \overline{u'v'} & \overline{u'w'} \\ \overline{u'v'} & \overline{v'v'} & \overline{v'w'} \\ \overline{u'w'} & \overline{v'w'} & \overline{w'w'} \end{pmatrix}. \tag{2.15}$$

Each term of the Reynolds stress tensor given in Equation 2.15 can be thought of as a momentum flux that essentially behaves as a stress in the turbulent flow. As apparent by the size of the tensor, nine new unknowns are introduced to the Navier-Stokes equation as a result of these momentum fluxes. This is a testament to the complexity that arises due to the effects of turbulence in a flow. Developing a way to model the Reynolds stress tensor is known as the closure problem of turbulence, and is the essence of turbulence modeling in computational fluid dynamics [25].

2.2 The $k-\omega$ SST Turbulence Model

The $k-\omega$ SST turbulence model is a RANS-based approach to representing the effects of turbulence, and like all other RANS turbulence models, has its origins associated with the Boussinesq eddy-viscosity approximation. The Boussinesq approximation assumes that the momentum flux generated by random molecular fluctuations is comparable to that generated by random turbulent fluctuations. This leads to the relationship where the Reynolds stress tensor can be computed as the product of an *eddy*-viscosity and the mean rate of strain tensor [25]:

$$\tau_{ij} = 2\nu_T S_{ij} - \frac{2}{3}k\delta_{ij}, \tag{2.16}$$

where ν_T is the kinematic eddy-viscosity and k is the turbulent kinetic energy. Adopting Wilcox's meaningful description, Equation 2.16 can essentially be regarded as the definition of eddy-viscosity — bearing the important relationship that the eddy viscosity-parameter is linearly proportional to the Reynolds stress tensor.

Under the Boussinesq regime, the high-level goal of turbulence modeling is to develop a means of computing the fluid's eddy-viscosity, which in turn can be used to evaluate the Reynolds-stress tensor. First developed by Wilcox [25], the $k-\omega$ turbulence model uses the *turbulent kinetic energy* (k) and the *specific dissipation rate* (ω) as its two dependent variables. Using these two variables, the kinematic eddy-viscosity is defined as:

$$\nu_T = \frac{k}{\omega}. \tag{2.17}$$

The $k-\omega$ in its original, "Wilcox (1998)" form is reported to produce accurate results for free shear flow *as well as* boundary layer flow, which is difficult for other two-equation models [25].

However, despite its favourable performance near the wall, the original Wilcox model has a

severe sensitivity to free stream values of the specific dissipation rate. This is addressed by Menter [42], who developed what is known as the shear-stress transport (SST) turbulence model. Menter's approach is twofold: first, the $k-\varepsilon$ model is transformed into a $k-\omega$ one, which involves the introduction of a cross-diffusion term; second, the original eddy-viscosity formulation (Eq. 2.17) is improved by accounting for the importance of the transport of the principal turbulent shear stress in the boundary layer. The first step results in the use of a k–ω formulation in the near-wall boundary layer, which is switched via a blending function to k–ε in the boundary layer wake region and outer free shear flow. The incorporation of turbulent stress transport in Menter's second step is what allows the turbulence model to predict flow separation in severely adverse pressure gradients (e.g. airfoils experiencing dynamic stall). Together, these advantages make the $k-\omega$ SST turbulence model the most suitable for accurate RANS-based CFD simulations in aerodynamics.

Following Menter's $k-\omega$ SST model, the transport equations for turbulent kinetic energy and specific dissipation rate are employed in STAR-CCM+ as [39]:

$$\frac{\partial}{\partial t}(\rho k) + \nabla \cdot (\rho k \overline{\boldsymbol{v}}) = \nabla \cdot [(\mu + \sigma_k \mu_t) \nabla k] + P_k - \rho \beta^* f_{\beta^*} (\omega k - \omega_0 k_0) + S_k \tag{2.18}$$

$$\frac{\partial}{\partial t}(\rho \omega) + \nabla \cdot (\rho \omega \overline{\boldsymbol{v}}) = \nabla \cdot [(\mu + \sigma_\omega \mu_t) \nabla \omega] + P_\omega - \rho \beta f_\beta \left(\omega^2 - \omega_0^2\right) + S_\omega, \tag{2.19}$$

where $\overline{\boldsymbol{v}}$ is the mean flow velocity, μ is the (molecular) dynamic viscosity, σ_k and σ_ω are model coefficients (i.e. constants), P_k and P_ω are production terms, f_{β^*} is the free-shear modification factor, f_β is the vortex-stretching modification factor, k_0 and ω_0 are ambient turbulence values, and S_k and S_ω are source terms. The production terms are made up of the following constituents:

$$P_k = G_k + G_{nl} + G_b \tag{2.20}$$

$$P_\omega = G_\omega + D_\omega, \tag{2.21}$$

where G_k is turbulent production, G_{nl} is non-linear production, G_b is buoyancy production, G_ω is specific dissipation production, and D_ω is the cross-diffusion term. The $k-\omega$ SST model's characteristic cross-diffusion term is defined as:

$$D_\omega = 2\rho (1 - F_1) \sigma_{\omega_2} \frac{1}{\omega} \nabla k \cdot \nabla \omega, \tag{2.22}$$

where F_1 is the blending function to switch between $k-\omega$ and $k-\varepsilon$, and σ_{ω_2} is another model

coefficient. This blending function and the shear stress transport blending function, F_2, are defined to be:

$$F_1 = \tanh\left(\left[\min\left(\max\left(\frac{\sqrt{k}}{0.09\omega d}, \frac{500\nu}{d^2\omega}\right), \frac{2k}{d^2 CD_{k\omega}}\right)\right]^4\right) \tag{2.23}$$

$$F_2 = \tanh\left(\left(\max\left(\frac{2\sqrt{k}}{\beta^*\omega d}, \frac{500\nu}{d^2\omega}\right)\right)^2\right), \tag{2.24}$$

where d is the distance to the wall, ν is kinematic (molecular) viscosity, $CD_{k\omega}$ is a cross-diffusion coefficient, and β^* is also a model coefficient. The blending functions are one of the key properties of the model that sets it apart from other traditional two-equation turbulence models. The remaining functions and constants of the k–ω SST turbulence model can be readily found in the STAR-CCM+ theory guide [39].

2.3 Boundary Layer Modeling

Coined by Ludwig Prandtl in the early 20th century, the all-important boundary layer concept in fluid dynamics explains a staggering amount of flow physics. The theory essentially divides a high Reynolds number flow domain into two regions: an outer region away from surfaces where viscous effects can be neglected, and a very thin layer in the vicinity of surfaces where the viscosity of the fluid plays an essential role. Prandtl's boundary layer effectively forms the basis of all high Reynolds number flow modeling, with a prime and diligently studied example being the external aerodynamic flow over an airfoil [43].

The crux of boundary layer wall treatment in CFD is the non-dimensional distance known as y^+. In the STAR-CCM+ code this dimensionless distance parameter is defined as [39]:

$$y^+ = \frac{\rho y u^*}{\mu}, \tag{2.25}$$

where ρ is the fluid density, μ is dynamic viscosity, y is the normal distance from the wall to the *centroid* of the first cell, and u^* is a reference velocity (often referred to as the friction velocity [44]):

$$u^* = \sqrt{\frac{\tau_w}{\rho}}, \tag{2.26}$$

with τ_w being the wall shear stress. Careful physical and numerical considerations require attention in order to properly predict the fluid dynamics in the near-wall region. Figure 2.1a depicts the

three regions that the inner boundary layer is made up of. The region closest to the wall, known as the viscous sublayer, has its flow physics dominated by viscous effects. This is in line with the notion that for constant density flow, vorticity is essentially generated only at the walls [45]. As a consequence of the high levels of vorticity and the no-slip condition at the wall, steep velocity gradients are present in the near-vicinity of the wall boundary.

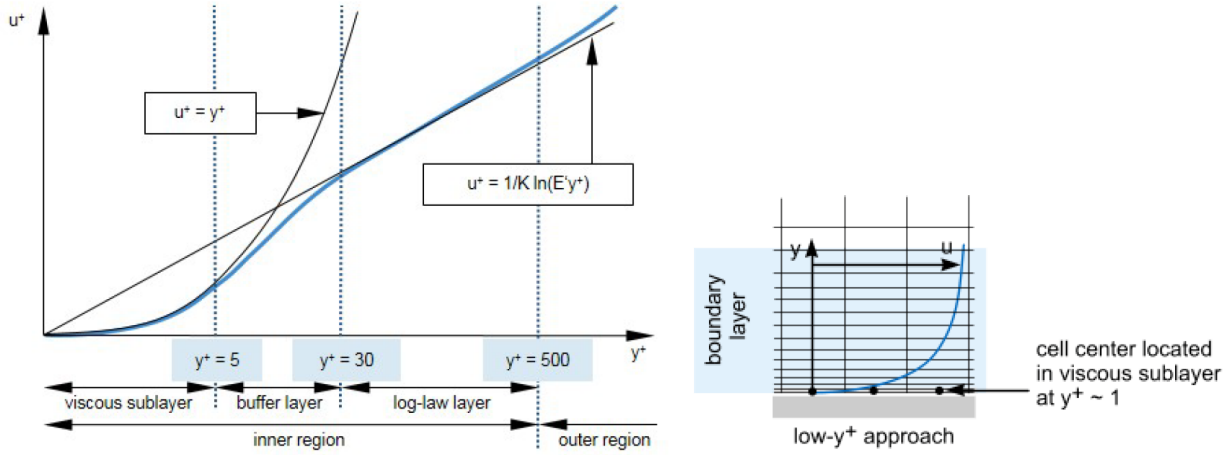

(a) Boundary layer sub-regions.

(b) Low y^+ wall treatment.

Figure 2.1: Boundary layer considerations in STAR-CCM+ [39].

Two approaches can be taken to numerically estimate the flow field within the boundary layer. The first, and more 'artificial' technique, is to employ models to essentially estimate the physics from the log-layer in Figure 2.1a all the way to the wall surface. To employ this approach, the near-wall mesh is designed such that the first cell's centroid distance from the wall produces a y^+ in the range of $y^+ \approx 30$. Rather than use semi-empirical wall model formulation, the second approach is to instead ensure that the first cell's height is small enough such that the centroid is well within the viscous sublayer region of the inner boundary layer. Figure 2.1b depicts this approach, which requires $y^+ \approx 1$ along the wall. The $y^+ \approx 1$ criteria can indeed impose significant implications to overall mesh size, however a full resolution of the boundary layer offers physical accuracy that simply cannot be achieved with modeling. Since the goal of the present simulation analysis is to accurately predict the forces and moments generated at the airfoil walls, the low y^+ approach is used in all simulations here and a strict enforcement of $y^+ \approx 1$ is maintained throughout the investigation.

2.4 Force and Moment Calculation

Obtaining a solution to the flow field allows physical quantities of interest to be computed and extracted from the CFD environment. For external aerodynamics, the surface forces and moments acting on the body under consideration are essential pieces of information. The force developed on a no-slip surface boundary is the result of the pressure and shear forces that act over the solid surface. The pressure force of the fluid acting on the surface face of an individual mesh cell is computed in STAR-CCM+ as [39]:

$$\boldsymbol{f}_f^{pressure} = (p_f - p_{ref})\,\boldsymbol{a}_f, \tag{2.27}$$

where p_f is the static pressure acting on the face, p_{ref} is a reference pressure, and $\boldsymbol{a}_f$ is the face area vector of the given cell.

The shear force of the fluid acting on a cell face, f, is given by:

$$\boldsymbol{f}_f^{shear} = -\boldsymbol{\tau}_f \cdot \boldsymbol{a}_f, \tag{2.28}$$

where $\boldsymbol{\tau}_f$ is the stress tensor acting at face f. Expanding Equation 2.5 and invoking the Boussinesq approximation, the total stress tensor is given by:

$$\boldsymbol{\tau} = \mu_{eff}\left[\nabla \boldsymbol{v} + \boldsymbol{v}^T - \frac{2}{3}(\nabla \cdot \boldsymbol{v})\right]\boldsymbol{I}, \tag{2.29}$$

where μ_{eff} is the effective viscosity due to both moelcular and turbulence considerations, or:

$$\mu_{eff} = \mu + \mu_t.$$

Considering the entire surface boundary, the magnitude of force in a specified direction is arrived at by summing the contribution of the pressure and shear forces experienced at each cell face:

$$F = \sum_f \left(\boldsymbol{f}_f^{pressure} + \boldsymbol{f}_f^{shear}\right) \cdot \boldsymbol{n_f}, \tag{2.30}$$

where $\boldsymbol{n_f}$ is a user-defined direction vector. To retrieve the x-direction force F_x, for example, the user-defined direction vector $\boldsymbol{n_f}$ is specified as $[1, 0, 0]$.

To determine the moment acting on the body, the lever arm cross product is incorporated into

Equation 2.30 to give:

$$M = \sum_{f} \left[\boldsymbol{r}_f \times \left(\boldsymbol{f}_f^{pressure} + \boldsymbol{f}_f^{shear} \right) \right] \cdot \boldsymbol{b}, \tag{2.31}$$

where $\boldsymbol{b}$ is the direction vector that defines the axis through moment origin point $\boldsymbol{x_0}$, and $\boldsymbol{r}_f$ is the position vector of cell face f relative to axis origin $\boldsymbol{x_0}$. The moment and force variables are recorded at each time-step of the simulation in order to provide a full history of the quantities.

2.5 Overset Meshing

Overset meshing, also known as chimera meshing, is a relatively new technique to the field of commercial CFD packages [39]. Considering its limited history in computational investigations, a few comments are offered here pertaining to this mesh method.

The approach involves at least two separate, standalone meshes — one stationary background mesh, and as many mobile overset meshes as desired, depending on the number of moving bodies under consideration. The fundamental idea is to overlap the background (i.e. underset) region with each overset region. In doing so, an interface is created between each overset region and the common underset region. Upon interface initialization, the cells in the underset region occupying the same space as the overset region are essentially removed and deactivated through a process known as hole-cutting. This methodology classifies cells as being *active* or *inactive* in each respective region, and includes *acceptor* and *donor* cells on the boundary linking both regions. Under this regime, the governing equations are solved only in the active cells throughout the computational domain. The interpolation topology between overset and underset regions is depicted in Figure 2.2. Here the dashed cells are acceptor cells, cells marked by a C are the respective mesh region's last cell before the acceptor cell of that same region, cells N_1—N_3 are donor cells from the same mesh region, and cells N_4—N_6 are donor cells from the other mesh region. In all simulations performed in the current CFD investigation, the linear interpolation option is used as this provides the most accurate numerical scheme for moving bodies [39].

Although only now becoming more common, the chimera mesh approach has recently been employed by other researchers undertaking CFD investigations on VAWTs and similar applications. Benedict et al. [38] make use of overset meshing with the CFD solver OVERTURNS to study the effect of a passive blade pitch VAWT design. Gauthier [46] employs overset meshing with STAR-CCM+ to efficiently model the motion of a hydrokinetic turbine blade undergoing complex heaving and pitching motion. Useful recommendations and insight is provided in the investigation of

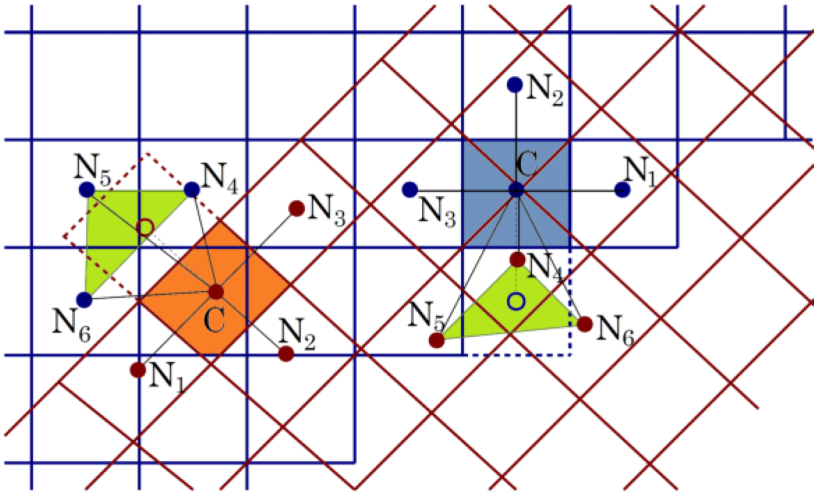

Figure 2.2: Overset mesh interpolation topology [39].

Kozak [47] pertaining to unsteady VAWT aerodynamics. Also using STAR-CCM+, Kozak offers a set of general recommendations for overset mesh environments, amongst which is a recommendation for the ratio of overset cell size to underset cell size:

$$\frac{1}{3} \leq \frac{l_o}{l_u} \leq \frac{2}{3}, \tag{2.32}$$

where l_o and l_u are the characteristic length sizes of the overset and underset meshes, respectively. For accurate chimera interpolation it is a requirement that the cell size and orientation must be similar at the interface between overlapping regions [39]; the current CFD investigation maintains a $\frac{l_o}{l_u}$ ratio of 1/2.

An example of the overset meshing configuration used in the current investigation is provided as Figure 2.3. Observing Figure 2.3a, the circular overset mesh region surrounding the airfoil can be seen overlaid against the coarser background mesh region. The mesh environment following the initialization of the interface between the overset and underset regions is shown in Figure 2.3b. The initialization results in the appropriate removal of background cells occupying the same physical space as the overset region, and now an overlap region between the two meshes can be seen as the slightly darker strip of cells on the periphery of the circular overset region. Details of the meshes used are presented in full during the description of each investigation component herein.

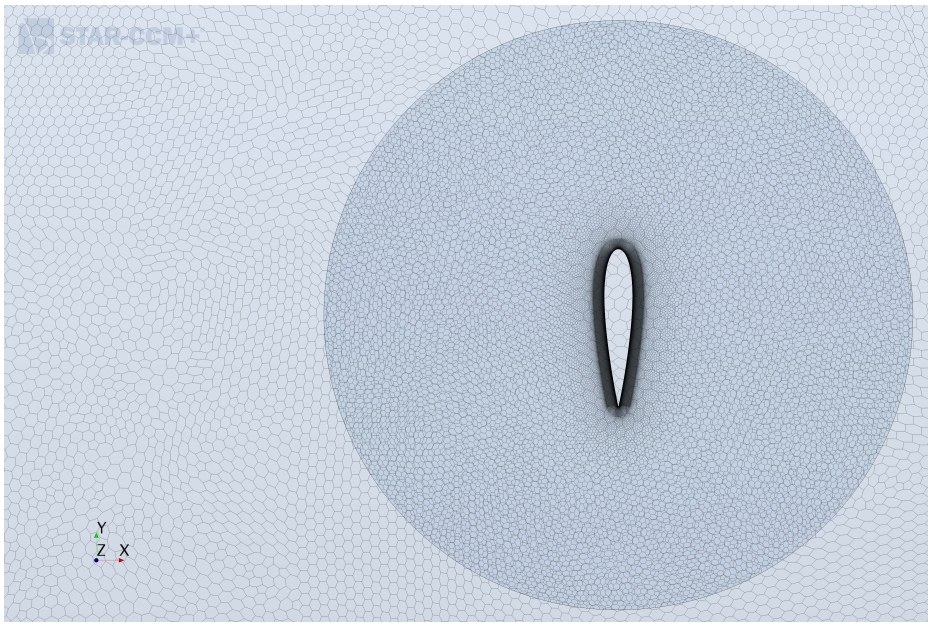

(a) Pre-initialization.

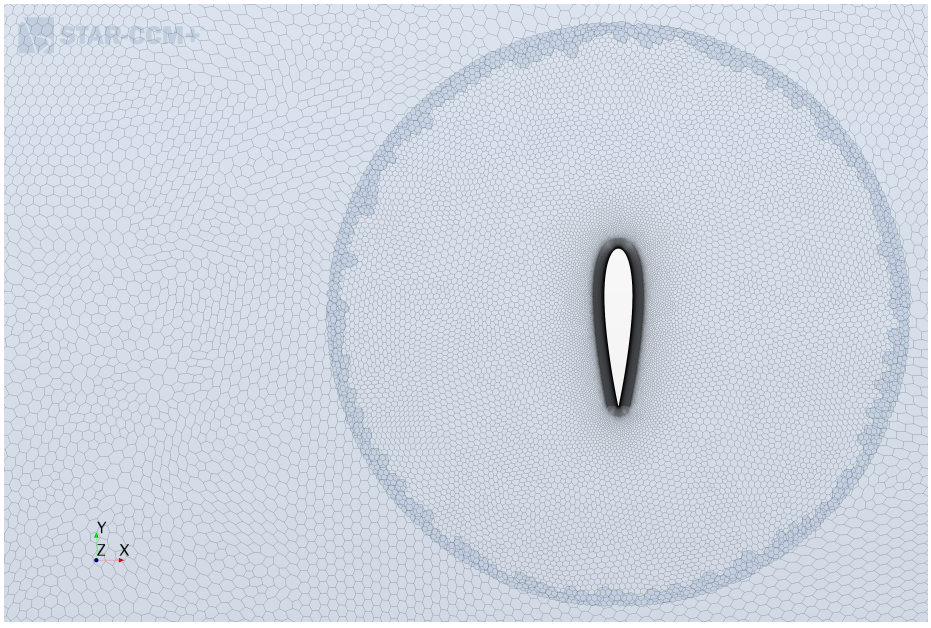

(b) Post-initialization.

Figure 2.3: Overset mesh used in the current CFD investigation.

Chapter 3

Methodology Validation

CFD is a numerical tool. As such, the tool requires validation so that confidence can be gained in the accuracy and physical fidelity of the model. The most reliable means of carrying out the validation is through comparison of the numerical results with those produced from an experimental investigation.

3.1 Simulating a VAWT in Dynamic Stall

Due to the extensive vortex generation and shedding over the blade, the simulation of a VAWT experiencing dynamic stall is a considerable challenge. As demonstrated in Figure 1.11, as the operational TSR of a VAWT decreases, the cyclical angle of attack increases. For low TSRs, on the order of $\lambda \leq 2$, there is a large portion of the cycle path where the blade's angle of attack exceeds the static stall angle. The violent separation and re-attachment of the blade's boundary layer throughout the cycle has a drastic impact on the surface forces and moments produced [31]. Knowing the complex flow physics associated with dynamic stall, the approach for the current investigation is to validate the CFD model with an experimental study under these flow conditions. The ability to predict a VAWT's operation under this regime provides confidence in the CFD tool's capacity to reliably handle the complexities inherent to VAWT fluid dynamics.

3.1.1 Experimental Study

The experimental study used to validate the current CFD approach is that of Dieter Castelein at TU Delft [48]. The intent of Castelein's work is to provide a benchmark experimental case for VAWT numerical model validation, and as such serves as an ideal case for comparison. The experimental

turbine is operated in the TU Delft open jet wind tunnel facility at a TSR of $\lambda = 2$ and freestream flow velocity of $V_\infty = 10.2\ m/s$. The characteristic geometry of the turbine is provided in Table 3.1.

Table 3.1: Experimental validation case turbine geometry.

Number of blades, N	2
Blade Shape	NACA0018
Blade Span, S [m]	1
Blade chord Length, c [m]	0.06
Rotor Radius, R [m]	0.5

There are two important geometrical considerations to identify from Table 3.1. First, the chord length to rotor radius ratio, c/R, is 0.12. This is a noteworthy characteristic, as low c/R ratios imply that the blade's upstream and downstream interaction and flow curvature effects are minimized [38]. Second, the ratio of the blade span to chord length, S/c, is over 16. By recording experimental data at the midspan of this high aspect ratio blade, a useful data set is provided for validation of *two*-dimensional numerical models as 3D and tip effects are minimized [20, 33]. Particle image velocimetry (PIV) is used to record the blade's midspan flow field during turbine operation, which is then used to compute the net normal and tangential forces acting on the blade.

3.1.2 Computational Approach

The CFD model developed to represent Castelein's experimental case is the foundation for all subsequent simulations performed in this study. As both the experimental validation case and the D-VAWT employ NACA0018 airfoil profiles, the validation CFD environment is readily adapted to suit the final D-VAWT investigation.

Mesh

The meshing process for this case makes use of STAR-CCM+'s polygonal mesh generator [39]. From a theoretical perspective, polygon meshes are believed to be capable of producing the smoothest growth rates and highest quality elemental meshes [45]. This notion is observed with the mesh environment created for the current analysis, as evidenced by the high quality mesh pictured in Figures 3.1-3.3.

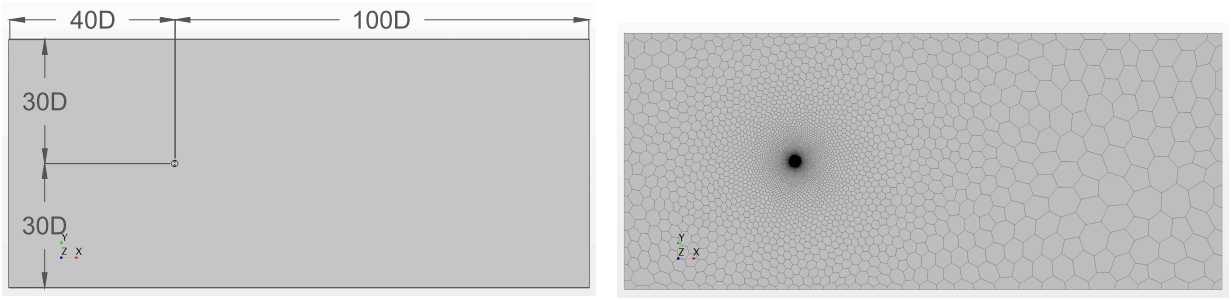

(a) Domain overview. (b) Domain mesh.

Figure 3.1: Overview of domain for experimental validation of CFD model.

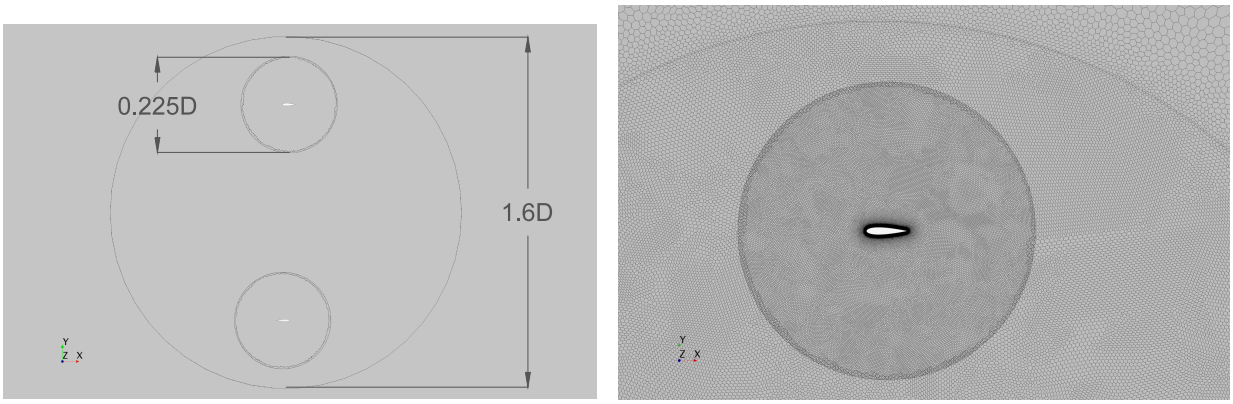

(a) Rotor area geometry. (b) Rotor area mesh.

Figure 3.2: Overview of rotor area for experimental validation of CFD model.

The outer computational domain dimensions given in Figure 3.1a are adopted from the recommendations of Balduzzi et al. [23]. A sufficiently large overset region is desirable such that the flow field gradients and complexity are reduced as to limit the interpolation error at the overset interface [39]. This recommendation, however, is not always possible to achieve based on the given geometry setup of the scenario being modeled.

The boundary layer mesh construction is shown in more detail in Figure 3.3, with STAR-CCM+'s *advancing layer mesher* option enabling a thick overall prism layer thickness to be generated. The thickness of the mesh's prism layer region is paramount for the current investigation as a thick boundary layer and heavy separation is expected for the blade's operation at low TSR.

Specific details of the mesh parameters are provided in Table 3.2. All element count totals are reported for active cells only after the overset interface initialization, or following the hole cutting procedure executed on the underset mesh region. Each overset region accounts for almost 1×10^5 elements, with the vast majority of cells clustered in the near-blade areas. At a count

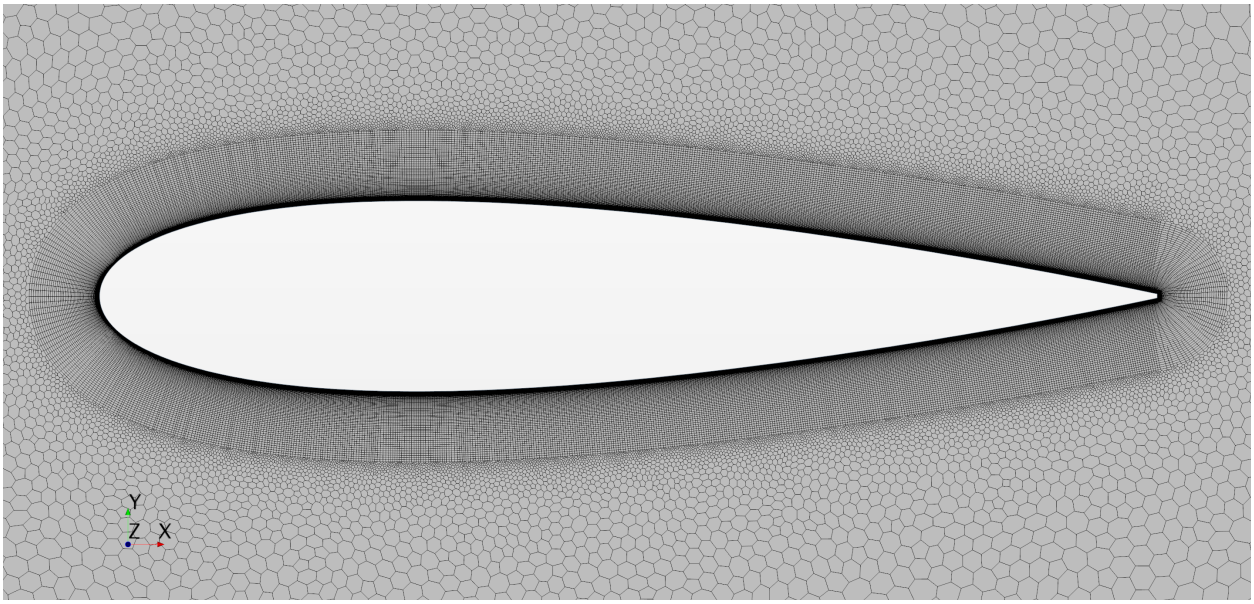

Figure 3.3: Boundary layer mesh for experimental validation case simulation.

of nearly 1000, a relatively large number of nodes over the airfoil surface is used to capture the boundary layer and vortex generation and shedding present in the low TSR case. The overset-to-underset ratio is strictly enforced at $\frac{1}{2}$, which is maintained for all succeeding simulations.

Numerics

To accompany a well-constructed mesh, judicious numerical choices are required to complete the CFD model. The key characteristic numerical parameters for the experimental validation exercise are provided in Table 3.3. An implicit, unsteady temporal solver is used with 2nd-order discretization in both the temporal and convective schemes. Typically, aerodynamic simulations for wind turbine operations involve low mach numbers and thus allow for an incompressible fluid regime to be adopted. However, for the current CFD approach, the segregated solver (with incompressible flow assumed) is found to produce unsatisfactory convergence trends for the continuity and both momentum residuals. The undesirable residual behaviour is rectified by activating the coupled energy flow solver, with the fluid's density instead being assigned by the ideal gas model (see Equation 2.10). Upon implementation of the coupled approach, the residuals are found to smoothly drop as is expected for a reliable CFD simulation. While the coupled approach and added energy equation (and density computation) undoubtedly adds considerable computational expense, the volatile residual trends of the segregated solver are unacceptable. The exact reason for the segregated solver's incapability to faithfully solve the current system of equations is unknown, but the issue is

Table 3.2: Experimental validation case mesh details.

Element size in overlap region	0.085c
Element size in overset region	0.0425c
Overset-to-underset element ratio $\left(\frac{l_o}{l_u}\right)$	$\frac{1}{2}$
Number of nodes on airfoil	962
Intended y^+	≤ 1
First cell height in boundary layer	0.000 17c
Number of prism layer elements	65
Prism layer total thickness	0.0667c
Number of elements in background region	102 559
Number of elements in one overset region	105 180
Total number of elements	312 919

presented here as a word of caution to other researchers carrying out similar CFD investigations.

3.1.3 Results

Aligning with the study of Castelein [48], the CFD model validation is accomplished by comparing the non-dimensionalized normal and tangential forces acting on the blade throughout one complete cycle. By extracting the x- and y-direction forces from the CFD solver, the azimuth angle position is used to convert the raw F_x and F_y forces into the desired force directions of interest, namely the normal, F_N, and tangential, F_T. An aerodynamic force analysis on the blade proves that at all azimuth positions in the cycle, the instantaneous normal and tangential forces are found using:

$$F_N = (F_x)\sin\theta - (F_y)\cos\theta \tag{3.1}$$

$$F_T = -(F_x)\cos\theta - (F_y)\sin\theta, \tag{3.2}$$

where the azimuth angle, θ, is taken from $\theta = 0°$ at top dead-center of the rotor. The converted forces (per unit blade length) are normalized using the rotor radius, R, and the freestream dynamic pressure, Q_∞ [34], given by:

$$Q_\infty = \frac{1}{2}\rho V_\infty^2. \tag{3.3}$$

To investigate temporal effects, two simulations are performed that are identical except for

Table 3.3: Numerical details for the experimental validation case simulation.

Temporal solver	Implicit unsteady
Temporal discretization	2nd-order
Courant number	75
Flow solver	Coupled energy
Convection scheme	2nd-order upwind
Equation of state	Ideal gas
Turbulence model	$k-\omega$ SST
Wall treatment	Low y^+

their respective time-steps. The final force comparison results from the two simulations is provided in Figure 3.4; it should be noted that the limited set of experimental data points shown is the extent of those reported in the study. A similar trend is observed between the $\Delta t = 0.18°/\omega$ (2000 steps-per-cycle equivalent) and refined $\Delta t = 0.12°/\omega$ (3000 steps-per-cycle) cases, with both providing impressive agreement with the experimental data considering the complexity of the flow field (i.e. vortex shedding, separation, re-attachment, etc.). Closer inspection of the force curves of the two simulation cases shows them to be almost identical for $0° < \theta < 90°$ (Figure 3.5), corresponding to the upstream region before drastic separation occurs. The discrepancies between the two simulations are visible in the downstream half of the blade cycle, and in particular for $270° < \theta < 360°$ (Figure 3.6). An appreciation for the flow field's extensive vortex generation can be seen in the $\Delta t = 0.18°/\omega$ simulation's turbulent viscosity ratio (TVR) shown in Figures 3.7 and 3.8.

Knowing its operation to be at the low TSR of $\lambda = 2$, blade flow separation and vortex shedding is to be expected for azimuth angles $\theta > 90°$ for the experimental turbine. However, the tip speed ratio of the D-VAWT under consideration operates under much faster blade conditions at $\lambda = 4.5$. Consequently, the D-VAWT blade's boundary layer can be predicted to remain largely attached throughout the cycle path. This leads to the notion that the CFD simulation must unquestionably provide accurate force and moment predictions for the upstream region where the flow is attached, but the complete resolving of the downstream separated flow is not as critical since this phenomenon will not be present for the case of a high-TSR turbine. Since the larger time-step simulation produces essentially the same force predictions while the flow is attached, the

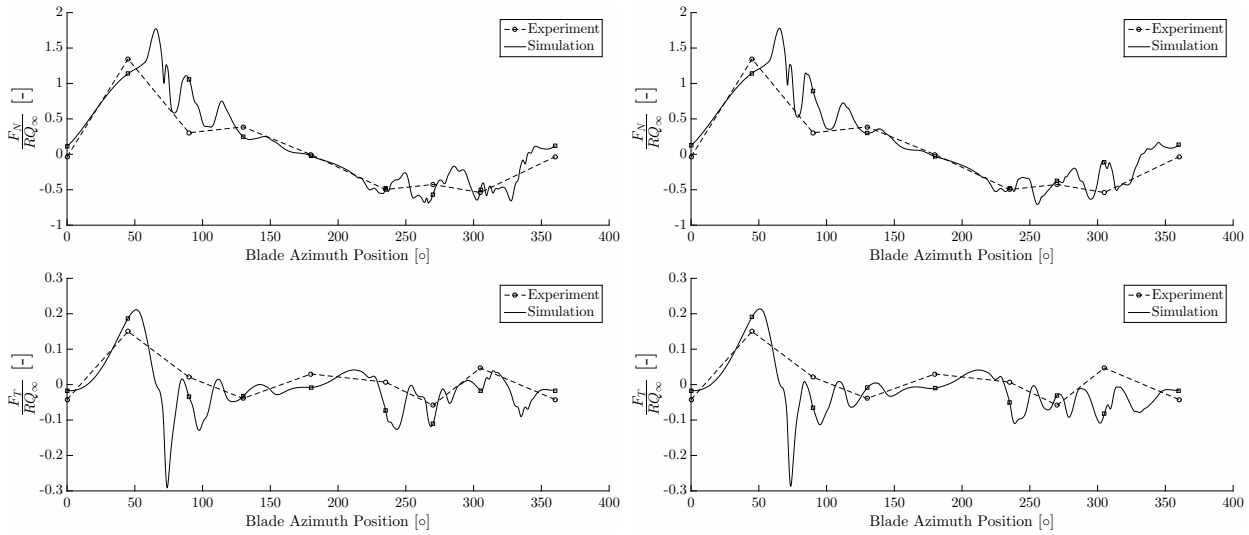

(a) Simulation with $\Delta t = 0.18°/\omega$.

(b) Simulation with $\Delta t = 0.12°/\omega$.

Figure 3.4: Comparison of CFD-predicted non-dimensionalized normal and tangential forces with experimental results.

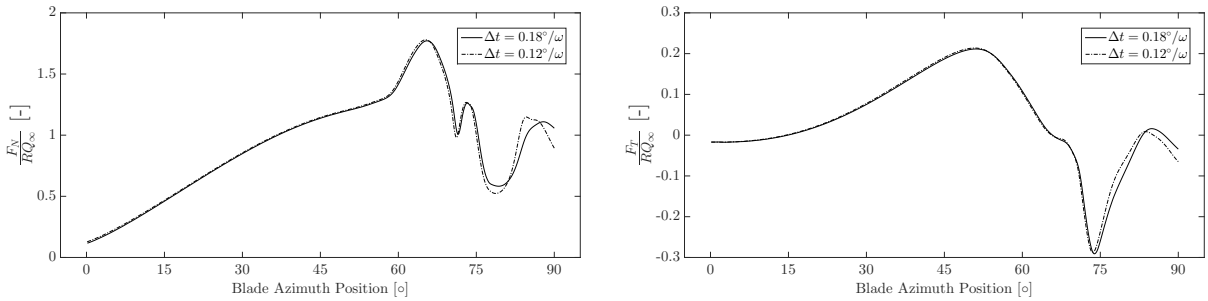

(a) Normal Force.

(b) Tangential Force.

Figure 3.5: Comparison of normal and tangential forces of $\Delta t = 0.18°/\omega$ and $\Delta t = 0.12°/\omega$ simulations between azimuth positions $0° < \theta < 90°$.

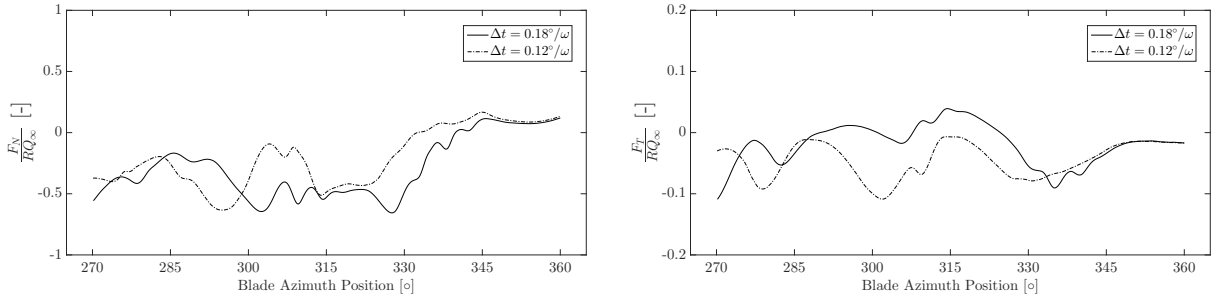

(a) Normal Force.

(b) Tangential Force.

Figure 3.6: Comparison of normal and tangential forces of $\Delta t = 0.18°/\omega$ and $\Delta t = 0.12°/\omega$ simulations between azimuth positions $270° < \theta < 360°$.

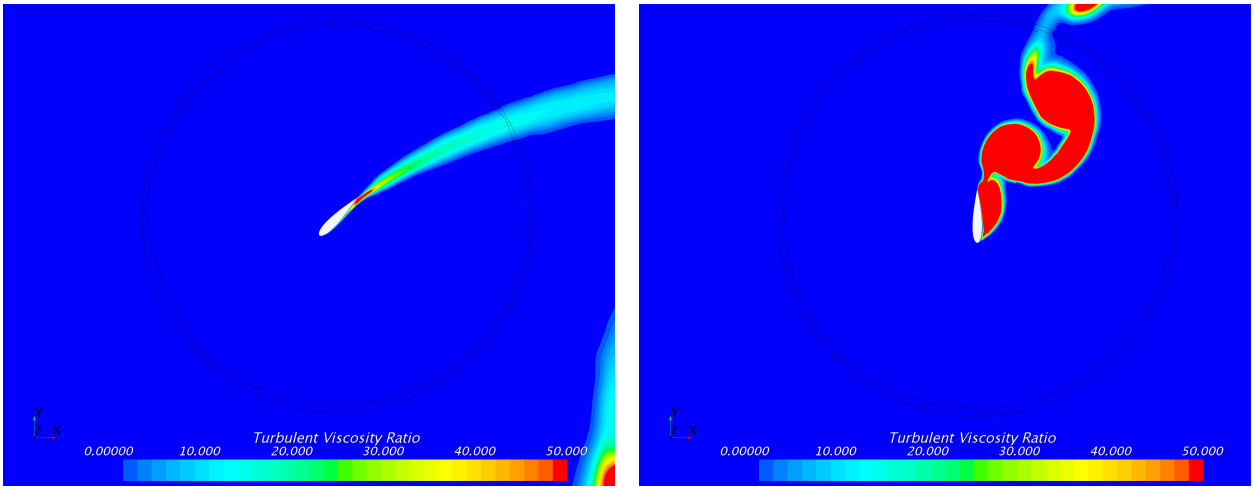

(a) Azimuth position $\theta = 45^{\circ}$. (b) Azimuth position $\theta = 90^{\circ}$.

Figure 3.7: Experimental validation case: Simulated flow field during the upstream portion of cycle.

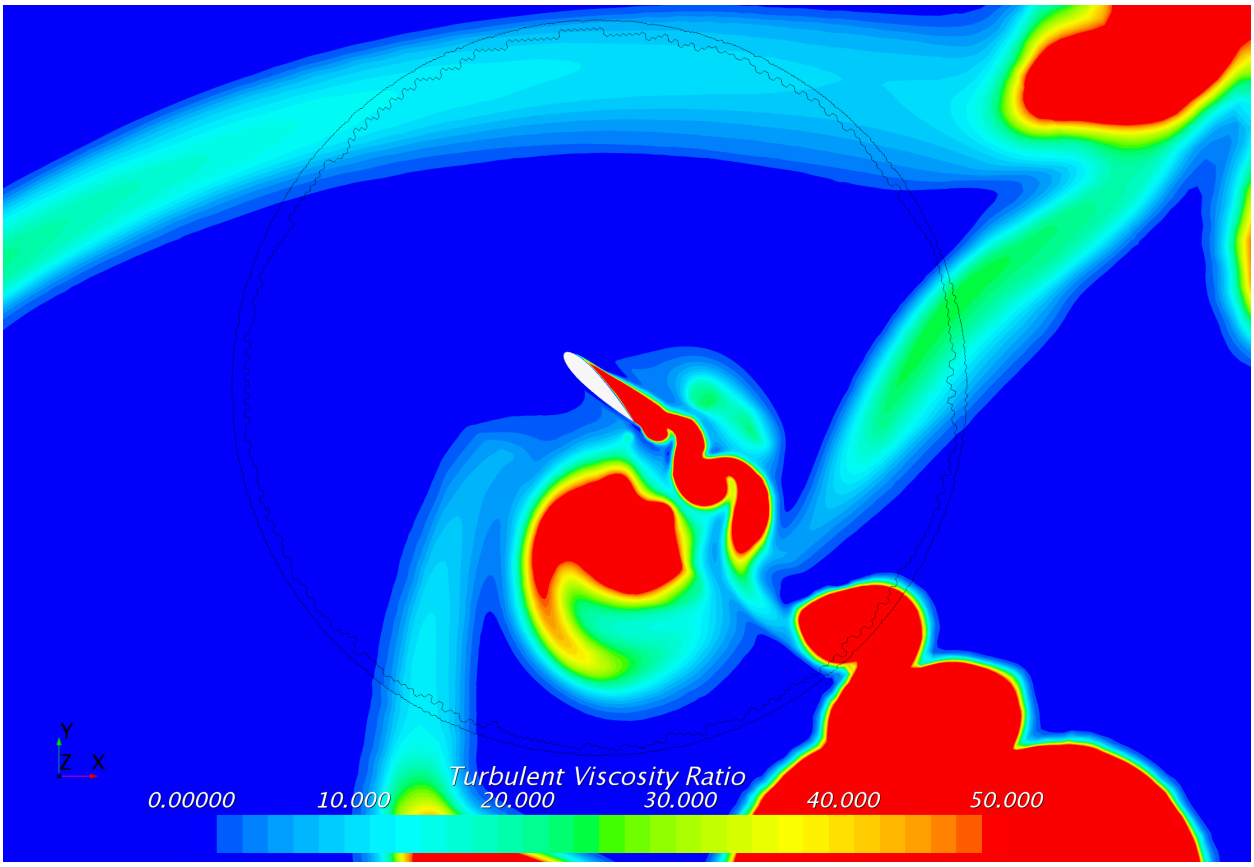

Figure 3.8: Experimental validation case: Simulated flow field during the downstream portion of cycle, shown here at azimuth position $\theta = 315^{\circ}$.

2000 steps-per-cycle scheme (or equivalent for the D-VAWT), is adopted for all simulations going forward. It is important to stress the fact that should the final force and power prediction value be required for the experimental turbine, the finer time-step of 3000 steps-per-cycle would surely have to be implemented for an accurate simulation. However, for the D-VAWT examined herein, a time-step of this refinement introduces unnecessary computational expense without any imperative flow physics being resolved.

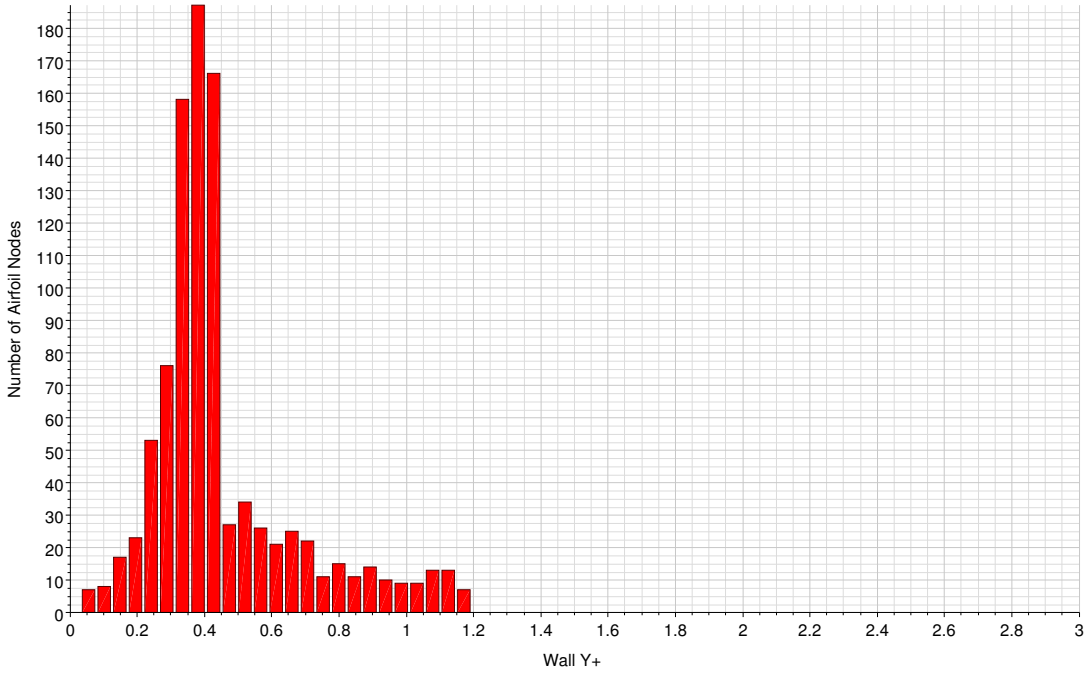

Figure 3.9: Airfoil y^+ distribution at $\theta = 0°$ azimuth position.

A final remark on the results of the CFD model validation is owed to the verification of y^+, the non-dimensional wall distance parameter. Since the Low y^+ wall treatment option is implemented within the $k-\omega$ SST turbulence model definition (see Table 3.3), it is a strict requirement that the y^+ value seen in the first cell of the boundary layer is indeed ≤ 1 across the entire airfoil surface. This is verified by extracting the y^+ variable from within the STAR-CCM+ environment, with the input surface being the airfoil wall. To assess the y^+ value, the worst case azimuth position of $\theta = 0°$ is analyzed since the relative flow over the airfoil is greatest at this point in the cycle, which in turn imposes the strictest criteria for the $y^+ \leq 1$ condition. A bar chart frequency distribution is displayed in Figure 3.9, where the 962 total nodes along the airfoil surface are binned according to their cell-centered y^+ value. As clearly seen, the vast majority of nodes have y^+ values safely below $y^+ = 1$, while only a few are slightly greater than the threshold. The y^+ verification is a

prudent step in the model validation process, and provides an additional level of reassurance of the approach undertaken.

Chapter 4

D-VAWT Baseline

The dual-vertical-axis turbine is a novel wind turbine design. Its blade path presents flow physics that have until recently never been fully explored [21, 49]. As such, before investigating a modification to this turbine's design, the baseline case must be considered.

4.1 Geometry and Parameter Definitions

The blade path profile of the D-VAWT is what makes it such a unique turbine design. Referencing Figure 4.1, the blade rotates about two axes with an elongated linear translation region linking the two. Under this topology scheme, four distinct regions can be identified: the East and West Translation regions, and the North and South Rotation regions. The characteristic geometry and operating conditions for the baseline 2D, 1-blade D-VAWT simulation are summarized in Table 4.1; all characteristics are adopted identically from Naccache [21]. Important to note from Table 4.1 is the previously chosen chord length and rotor radius produce a ratio of $\frac{c}{R} = 0.5$, which is quite large for a vertical-axis wind turbine and whose impact is to be discussed in Chapter 5.

Swept area is one of the key geometric parameters for wind turbines. The area covered by a turbine's rotor is directly proportional to the total amount of kinetic energy that is available in the wind. For the D-VAWT, the traditional VAWT swept area formulation is adapted to incorporate the linear translation section as:

$$A = (L + 2R)\, h, \tag{4.1}$$

where for 2D considerations the height of the rotor, h, is taken to be unity. Leading from the altered swept area of Equation 4.1, the measure of the D-VAWT's coefficient of power also has to

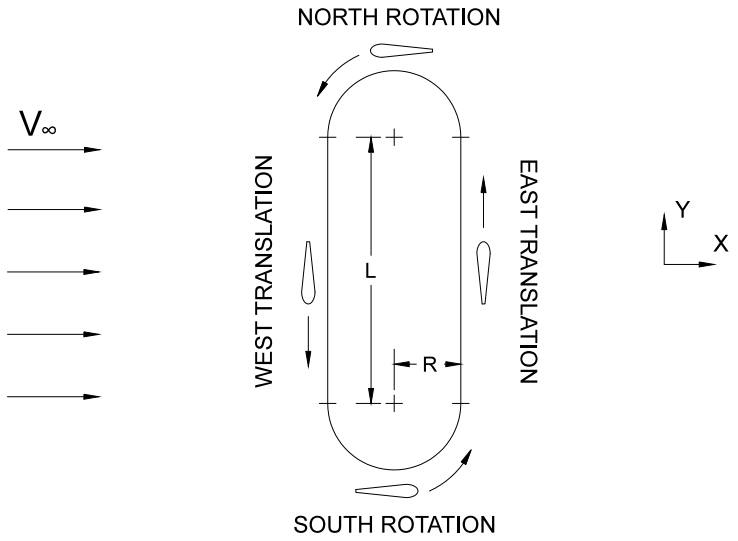

Figure 4.1: Baseline 1-blade D-VAWT motion topology.

be accounted for. A turbine's power coefficient is the ratio of the power extracted by the device to the available power in the incoming wind. The potential power available in the wind is derived from the change in kinetic energy with respect to time and given by [13]:

$$P_{wind} = \frac{1}{2}\rho A V_{\infty}^{3}, \tag{4.2}$$

where A is a reference area, which in the case of a wind turbine is taken to be the rotor swept area (such as that given in Equation 4.1). A typical vertical-axis wind turbine produces power through the summation of each blade's aerodynamic torque as the rotor rotates in a perfectly circular manner. However, the D-VAWT's blade motion profile is such that there are two regions of rectilinear motion, and thus the computation of an individual blade's torque during these regions is unphysical. This is considered in the work of Naccache [21], who defines the coefficient of power for the D-VAWT as:

$$C_P = \frac{P_{turbine}}{P_{wind}} = \frac{P_{rotating} + P_{translating}}{P_{wind}} = \frac{M_R\omega + F_T V_b}{\frac{1}{2}\rho A V_{\infty}^{3}}, \tag{4.3}$$

where M_R is the torque or moment during blade rotation, F_T is the translating or tangential force during rectilinear motion, and V_B is the linear blade speed. With this definition, the physics of the D-VAWT's aerodynamic power production are more realistically represented. Additional justification is provided by Naccache [21], who demonstrates that this method of performance

Table 4.1: D-VAWT baseline geometry and operational characteristics.

Number of blades, N	1
Blade shape	NACA0018
Blade chord Length, c [m]	0.4
Rotor radius, R [m]	0.8
Axes spacing, L [m]	3.2
L/R Ratio	4
Freestream wind velocity, V_∞ [m/s]	4
Tip speed ratio, λ	4.5
Blade rate of rotation, ω [rpm]	22.5
Blade linear velocity, V_B [m/s]	18

computation is conservative with regards to the numerical value of C_P computed.

4.2 Computational Approach

The same computational methodology for the experimental validation case of Section 3 is adopted for the D-VAWT baseline simulation. Essentially all numerical settings are kept in accordance with Table 3.3. The domain overview and geometry is provided in Figure 4.2 and the mesh details in Table 4.2. One change to note in the constructed mesh for the D-VAWT is the use of a one-cell-

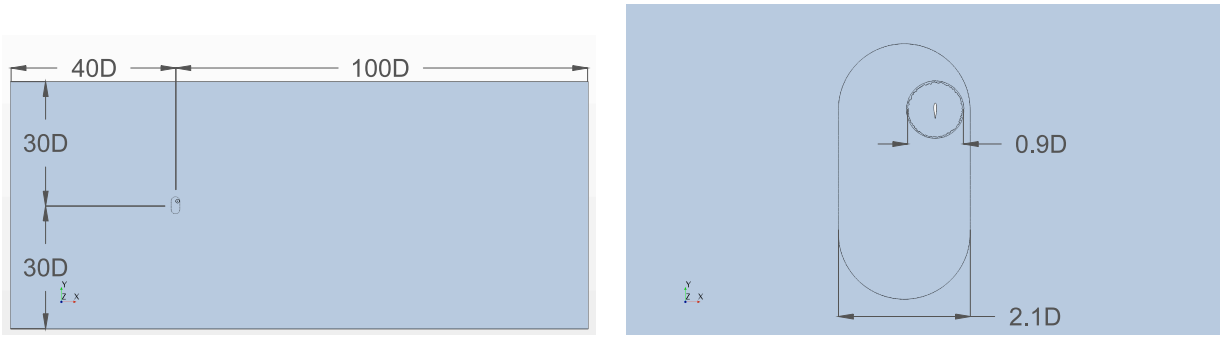

(a) Domain overview. (b) Rotor overview.

Figure 4.2: Overview of CFD domain for D-VAWT baseline.

thick approach in the third (i.e. z-) direction of the computational domain. This approach is used in order to provide the capability of utilizing STAR-CCM+'s six degree-of-freedom (6-DOF) solver

Table 4.2: D-VAWT baseline mesh details.

Element size in overlap region	0.08c
Element size in overset region	0.04c
Overset-to-underset element ratio $\left(\frac{l_o}{l_u}\right)$	$\frac{1}{2}$
Number of nodes on airfoil	1040
Intended y^+	≤ 1
First cell height in boundary layer	0.0007c
Number of prism layer elements	75
Prism layer total thickness	0.0667c
Number of elements in background region	35 150
Number of elements in one overset region	99 327
Total number of elements	134 477

for fluid structure interaction, which requires at least one cell in the third dimension. The use of one cell in the z-direction is expected to have no negative effects on the simulation tool's robustness or accuracy, since this is a common CFD practice.

The primary challenge in simulating the D-VAWT arises from the blade's atypical motion profile. Fortunately, STAR-CCM+'s overset meshing ability allows for complex motion to be assigned to a body in an accessible manner. Herein, the blade's rate of rotation, axis of rotation, and linear velocity are each assigned using *user-defined field functions* (UDFFs) within the STAR-CCM+ environment. The source code for these functions is provided in Appendix B.1. All three characteristics of the body's motion, namely linear and rotational velocity and axis of rotation, are assigned as a function of time-step. Adopting the time-step size of $\Delta t = 0.18°/\omega$ or 2000 steps/cycle from the experimental validation VAWT, the D-VAWT time-step is set such that each semi-circle rotation region maintains a discretization of 1000 steps. With the additional two rectilinear regions (East and West) using the same size time-step, the overall number of steps to complete one D-VAWT cycle is 4546. Knowing the exact number of steps in each of the four regions — 1000 for each rotation and 1273 for each rectilinear — two additional UDFFs are created to track the cycle number and step count of the current cycle. Using the cycle step function, the appropriate motion characteristic is assigned for each time-step during the simulation. At the time of development, this method was extensively verified to ensure the correct motion profile is achieved, although the

abrupt change in motion specification at the instant of change from linear to rotational motion and vice versa does introduce a brief transient "shock" to the CFD solver that is apparent in the blade surface forces.

4.3 Flow and Force Interpretation

A prerequisite to analyzing the forces and moments acting on the blade is to ensure that the flow field is behaving as expected. In particular, Section 3.1.3 explains how during the development of the D-VAWT simulation environment the assumption is used that minimal separation should occur during the turbine's operation. This hypothesis is attributed to the turbine's relatively high TSR, and allows for the larger of the two incremental azimuth time-steps to be employed. Figure 4.3 is a presentation of the baseline D-VAWT's turbulent viscosity ratio as the blade travels linearly in the negative y-direction through the West Translation region. The flow is essentially fully-attached under this scenario, which is a stark contrast to the experimental case TVR flow field at the equivalent azimuth position shown in Figure 3.7b. Analysis of the flow solution history shows minimal flow separation throughout the other regions of the blade's motion, and thus the original hypothesis made for fully-attached flow is assumed valid.

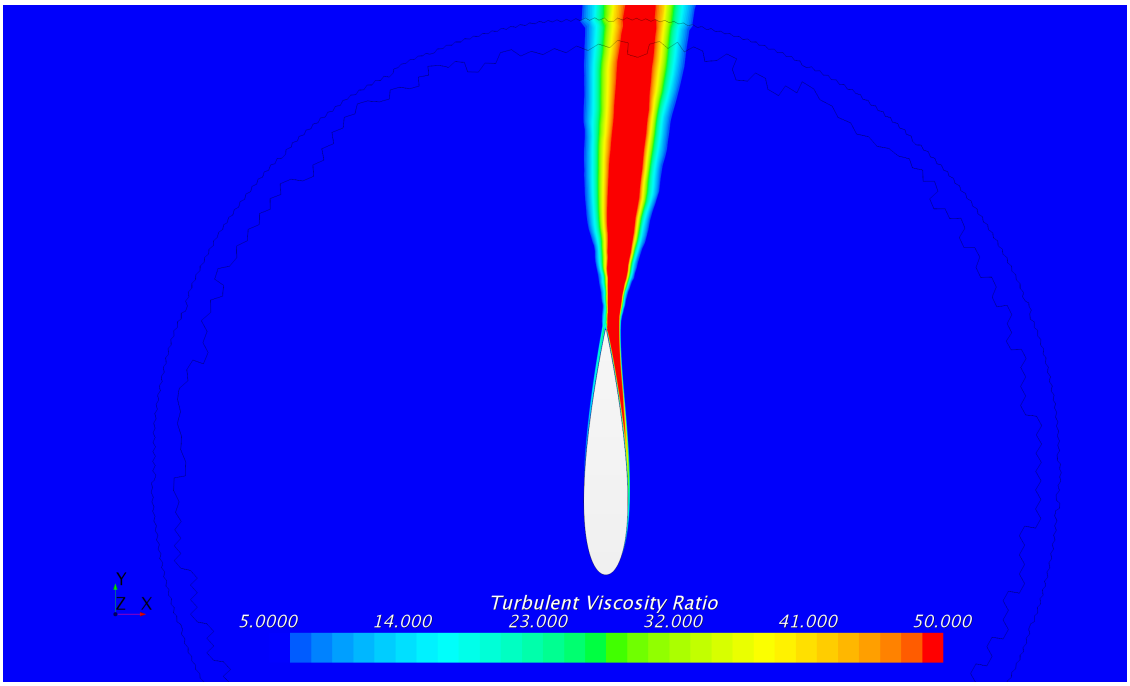

Figure 4.3: D-VAWT baseline turbulent viscosity ratio during the West Translation region, or quasi azimuth $\theta = 90°$ position.

For aerodynamic analysis, a CFD solver offers a crucial means of computing the forces and moments acting on a particular body. For a traditional VAWT at high TSR, the x- and y-direction forces acting on any given blade follow a relatively smooth, albeit cyclical, trend as the rotor completes one revolution of motion. However, the D-VAWT requires a virtually instantaneous change in motion specification between each region. From a computational perspective, this requires prescribing a "new" motion to the body (or in this case overset region) in line with the first time-step in the proceeding region of motion. As can be expected, this has numerical implications for the CFD solver.

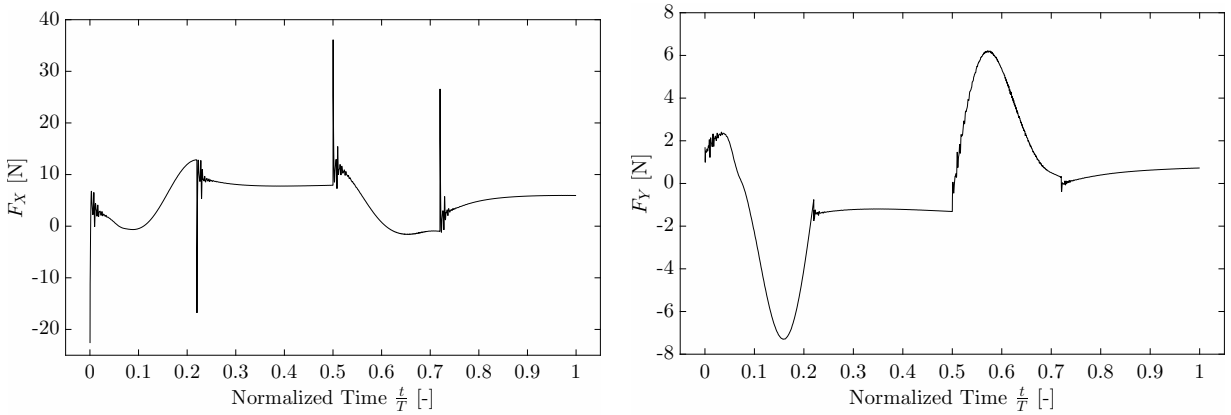

(a) Raw x-direction force.

(b) Raw y-direction force.

Figure 4.4: Raw forces extracted from D-VAWT blade surface over one complete cycle.

Figure 4.4 depicts the extracted x- and y-direction forces acting on the blade during one complete cycle of the baseline D-VAWT. Aerodynamically, the force trends in both directions make sense when considering traditional VAWT transient fluid dynamics. However, attention is to be drawn to the x-direction force at the beginning of each region of motion. As can be seen, upon the transition from one motion to the next, the force magnitude first peaks and is then followed by a transient oscillation period before acquiring an expected trend. Extensive investigation and deliberation was given to this phenomenon during the investigation. Observing the static pressure field surrounding the blade, a period of apparent 'flow recalibration' is present at the beginning of each region of motion, which lasts for approximately 100 time-steps or just under 14 ms. It is also important to note that the pressure (and force) recalibration is primarily in the x-direction, or the direction parallel to the freestream wind and perpendicular to the D-VAWT's longitudinal axis (see Figure 4.1). Therefore, it is believed that the oscillatory nature observed for F_x is almost a reaction in the CFD solver to the instantaneous change in motion. Physically, the spiking in force and

period of oscillation could be representative of the structural forces that would be encountered in a working prototype of the turbine. This behaviour is not seen as a serious concern to the accuracy of the performance prediction, especially considering that similar force spikes were experienced by Naccache [21] while using a completely different motion definition and computational approach (and CFD code). Attention to this issue is drawn here in case future researchers face similar findings when analyzing aerodynamics for bodies under complex, rapidly changing motion.

4.4 Power Coefficient

Considering overall potential turbine performance, the power coefficient is the most important parameter to analyze. Given by Equation 4.3, it is essentially a measure of the aerodynamic efficiency of the device. To determine the coefficient's value, the parameters to be derived from the CFD solver are blade torque, M_R, and tangential force, F_T. By assigning the correct axis of rotation during the respective North and South regions, the moment acting on the blade surface is extracted directly from the simulation solution. During the East and West translating regions, the tangential force required to compute the aerodynamic power is exactly the y-direction force, which can also be directly extracted. The full time history of each parameter is imported and post-processed using custom-written MATLAB scripts. Finally, a value for the instantaneous power coefficient is arrived at for every time-step of the simulation. A comparison of the transient power coefficient curves of the current investigation and that of Naccache is provided in Figure 4.5.

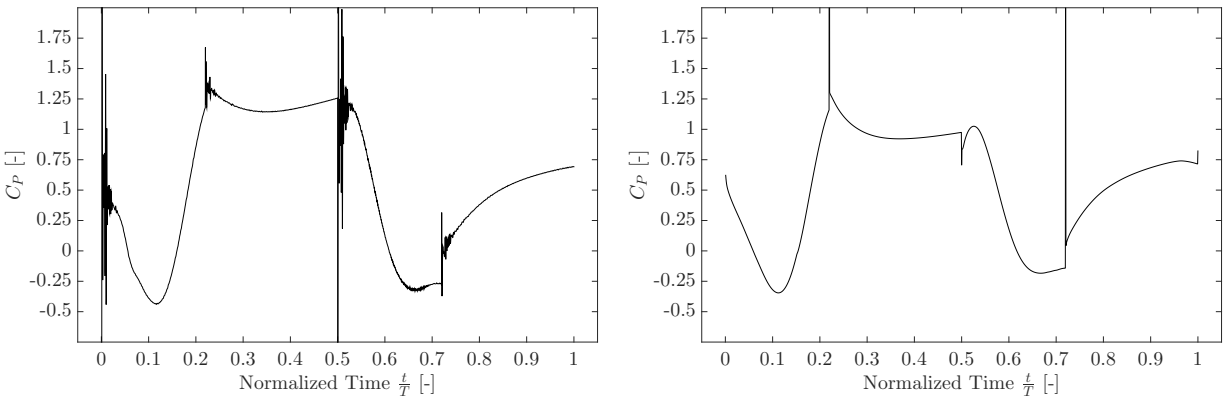

(a) Current investigation results.

(b) Naccache investigation results [21].

Figure 4.5: Instantaneous power coefficient for one D-VAWT blade.

Comparing the two C_P results, a similar trend is observed over the course of the cycle. The

aligning of the baseline C_P curves is notable since the performance of the D-VAWT was explored for the first time during the work of Naccache, and therefore to reproduce similar physical results during the current investigation is a reassuring finding for the potential of this turbine design. As expected, the turbine's blade produces the maximum power during the West Translation region, which is essentially the underlying premise of the design methodology. Similar to traditional VAWTs, regions of negative power production — where the resultant aerodynamics acting on the blade cause the tangential force to point in the opposite direction to the blade's motion — are still present in the D-VAWT. Addressing negative regions of torque generation is one of the primary drivers for vertical-axis wind turbine blade pitch control. Interestingly, the East or downstream translation region is also responsible for a significant portion of the D-VAWT's overall power production.

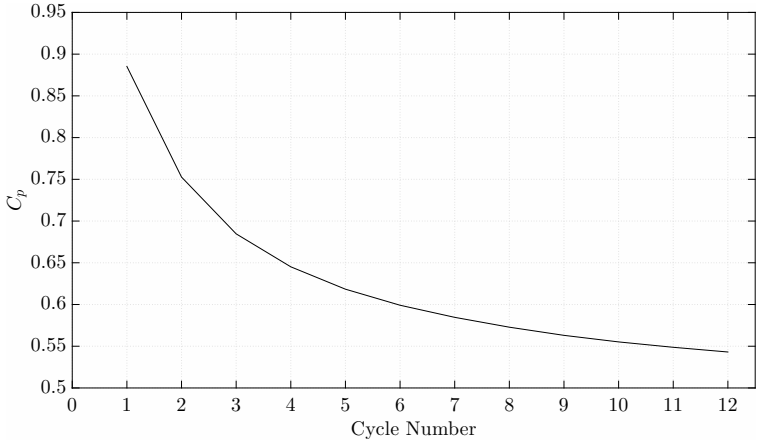

Figure 4.6: Cycle-to-cycle C_P convergence for the 1-blade D-VAWT baseline.

Table 4.3: D-VAWT baseline cycle-averaged power coefficient.

Naccache investigation baseline C_P	0.53
Current investigation baseline C_P	0.54
Percent difference	1.85%

Averaging the instantaneous C_P values in Figure 4.5 gives the final cycle-averaged coefficient of power, which in this case is the variable of most interest. The cycle-to-cycle convergence of C_P for the 1-blade baseline D-VAWT is presented in Figure 4.6. A smooth and expected trend is observed as the flow field matures with each progressive cycle, with the final cycle-to-cycle change in values being 1.0%. Although the trend is still slightly decreasing, due to the computational resources available and the constraint of time, a convergence of $\approx$1% is deemed acceptable as the

primary goal of the investigation is to explore the physical interaction within the flow. The final averaged C_P values from the current investigation and that of Naccache's are provided in Table 4.3. The computed values are quite close, with a final percent difference of less than 2%. The observed discrepancy has a number of potential sources. Most notably, the blade mounting point used by Naccache is at 1/3c from the leading edge, whereas for the current analysis it is at 1/2c. Blade mounting point location is known to have the effect of altering the incoming wind incidence angle (or angle of attack) [35], and as such can have a notable impact on the power produced. The reason for this geometrical difference is primarily a numerical one to facilitate the implementation of turbine start-up simulation in the current investigation. Naccache [21] does in fact show that the D-VAWT has an impressive insensitivity to mounting point at this particular TSR of $\lambda = 4.5$, and thus this behaviour aligns with the small change in C_P observed here. Other explanations for the difference in C_P are the current approach's use of the fully coupled solver instead of segregated, and adoption of the ideal gas and energy models instead of the standard incompressible flow assumption.

Chapter 5

D-VAWT Active Blade Pitch Control

Controlling the individual blade pitch orientation of a vertical-axis wind turbine blade is a powerful means of altering the aerodynamics experienced by the rotor. The central goal of the current investigation is to investigate the 1-blade D-VAWT's operation while the pitch angle of the blade is transformed depending on its regional location within the rotor's cycle.

5.1 Preliminary Fixed-Pitch Analysis

The baseline turbine presented in Chapter 4 is essentially the 1-blade D-VAWT device with a blade pitch angle, ϕ, fixed at $\phi = 0°$. To gain an understanding of the effect of pitching the D-VAWT's blade, two preliminary fixed-pitch (FP) simulations are carried out before moving to active-pitch (AP). Namely, a fixed trailing edge outwards (TE-OUT) with respect to the D-VAWT rotor longitudinal center and a trailing edge inwards (TE-IN) are examined. Both fixed-pitch regimes use an angle of $\phi = \pm 5°$. A visualization of the pitch offset angles and resulting pressure fields surrounding the blade can be seen in Figures 5.1 and 5.2.

Figure 5.1 depicts the blade's linear translation during the West Translation region — the region of optimal aerodynamic performance within the D-VAWT cycle. The $\phi = +5°$ TE-OUT case shown in Figure 5.1a shows a large suction region on the inner side of the airfoil, which corresponds to a significant production of lift and desired tangential force in the direction of motion (negative y-direction). This is in accordance with a priori understanding that a TE-OUT blade pitch angle will increase the effective angle of attack on the airfoil at this quasi $\theta = 90°$ azimuth position, and thus increasing the lift force (until stall is reached). For an inwards pitch angle at this point in the rotor cycle, Figure 5.1b proves that a less favourable pressure differential is developed and

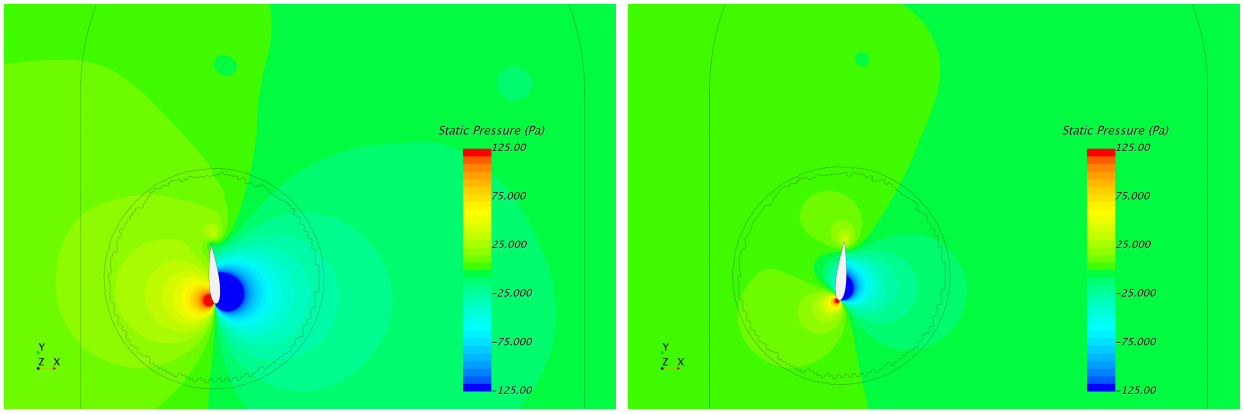

(a) TE-OUT: $\phi = +5^{\circ}$. (b) TE-IN: $\phi = -5^{\circ}$.

Figure 5.1: Preliminary FP analysis: pressure field surrounding blade during West Translation.

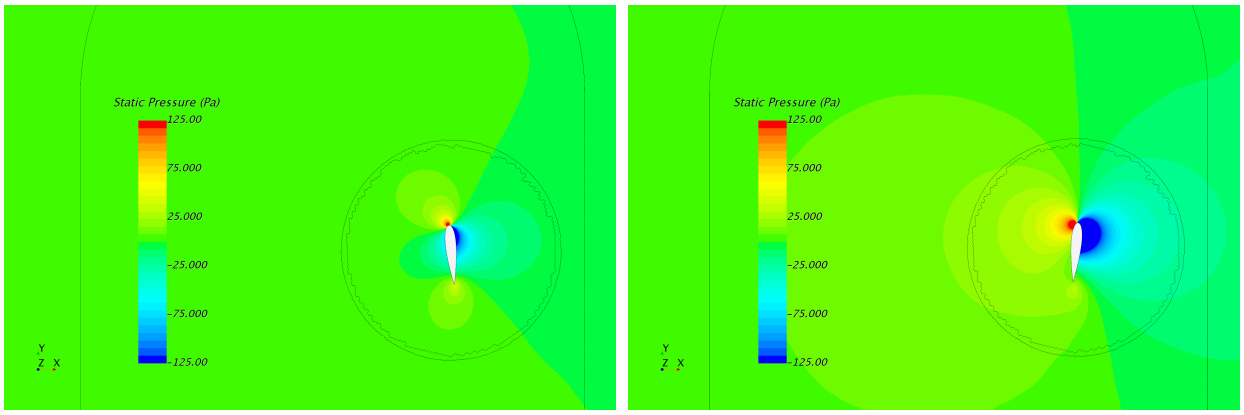

(a) TE-OUT: $\phi = +5^{\circ}$. (b) TE-IN: $\phi = -5^{\circ}$.

Figure 5.2: Preliminary FP analysis: pressure field surrounding blade during East Translation.

therefore a smaller amount of power is extracted from the flow. The generated pressure fields' effect on aerodynamic power production in this region is evident in the C_P curves given in Figures 5.3 and 5.4. Focusing on the West Translation region between $0.2 < \frac{t}{T} < 0.5$, the $\phi = +5^{\circ}$ outwards blade pitch in Figure 5.3 produces a significantly higher instantaneous C_P than the $\phi = -5^{\circ}$ case of Figure 5.4.

A complementary flow physics situation is observed in the East Translation pressure fields of Figure 5.2. Here it is the inwards rotation of $\phi = -5^{\circ}$ that effectively creates a larger angle of attack and greater tangential force in the direction of motion (positive y-direction). Again, this is reflected in the computed instantaneous C_P, where Figure 5.4 demonstrates a significant performance improvement in the East Translation region between $0.7 < \frac{t}{T} < 1$, and also in the latter half of the South Rotation region corresponding to approximately $0.6 < \frac{t}{T} < 0.7$.

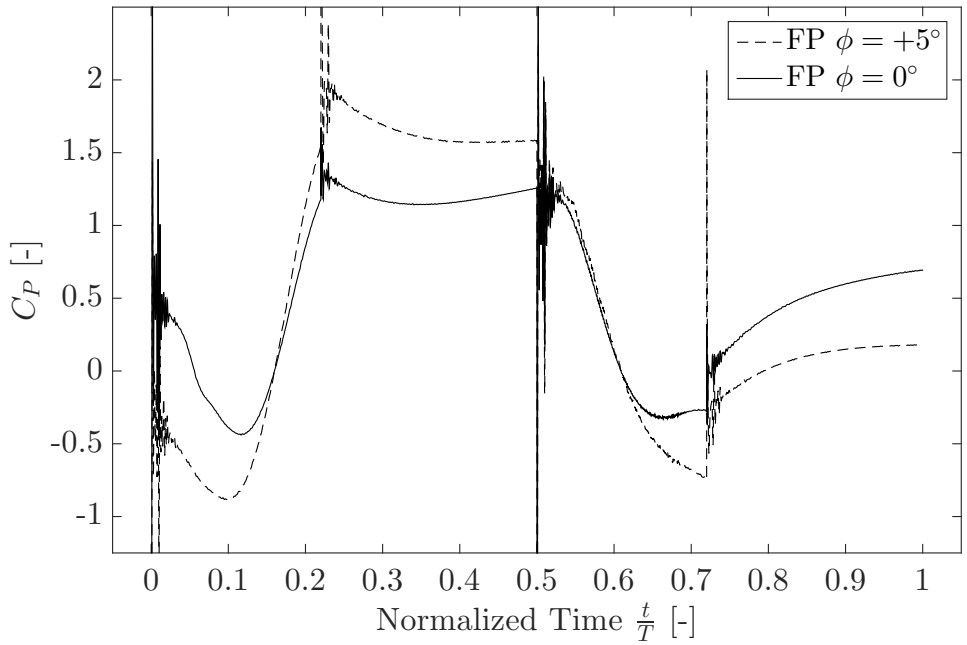

Figure 5.3: Fixed-pitch TE-OUT, $\phi = +5°$: Instantaneous C_P comparison.

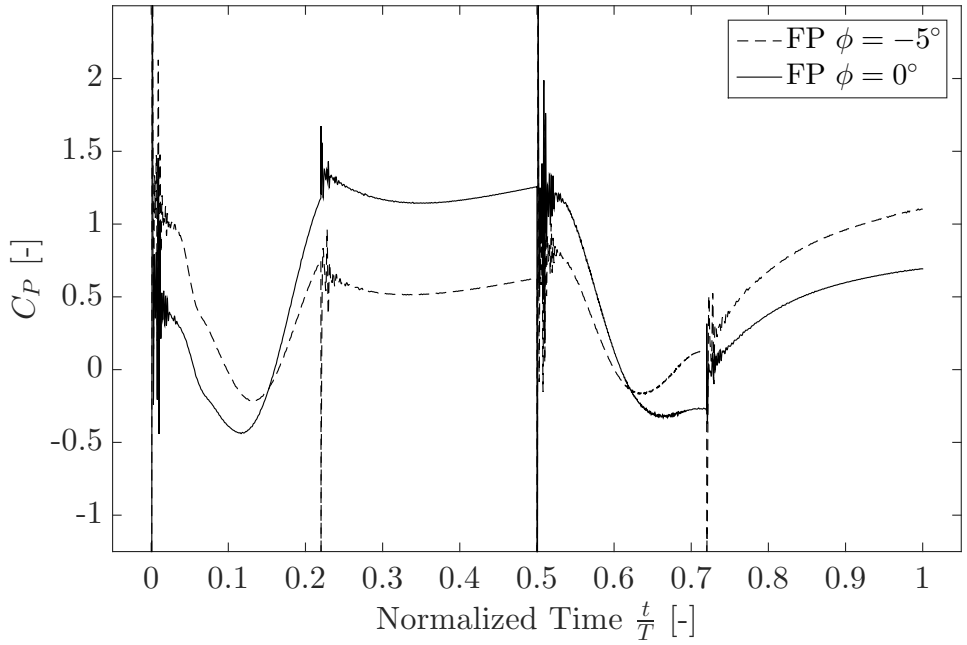

Figure 5.4: Fixed-pitch TE-IN, $\phi = -5°$: Instantaneous C_P comparison.

Although simply a prerequisite analysis before the active-pitch implementation, the fixed-pitch simulations offer insight into the flow physics and the impact of pitching the D-VAWT blade. Recalling the baseline's cycle-averaged C_P value of 0.54, the C_P values for the TE-OUT ($\phi = +5°$) and TE-IN ($\phi = -5°$) cases are 0.46 and 0.5, respectively. The lower TE-OUT C_P value supports the notion that TE-OUT fixed blade pitch angles are typically less favourable than equivalent fixed-pitch TE-IN angles for vertical-axis wind turbines [35, 37]. Of interest from the instantaneous C_P curves of Figures 5.3 and 5.4, even with the large pitch angles of $\phi = \pm 5°$, is how the blade appears to evade stall during the entire cycle. This is an important observation since the D-VAWT's West Translation region in particular is designed to be maximally aerodynamic efficient [21]. Consequently, a potential increase in turbine performance could be achieved if the blade's angle of attack can be increased in this region without experiencing stall.

5.2 Active-Pitch Computational Approach

Building off the methodology developed to implement the baseline D-VAWT blade path, a method is devised to employ active blade pitch also as a function of time-step throughout the cycle. Pitching of the blade is taken to occur about the blade's centroid, which for the NACA0018 blade profile can be computed to be at approximately $x = 0.4c$ from the leading edge along the chordwise longitudinal axis. However, to assign a rate of rotation to a body, STAR-CCM+ requires an exact axis of rotation to be specified in all three coordinate directions. Determination of the cartesian position vector of the blade body is not a readily extractable variable from the simulation environment, and as such a manual technique is used to accurately determine the exact centroid position at each time-step. This is accomplished using the geometrical features shown in Figure 5.5. A local coordinate system is defined at the blade's centroid at time $t = 0$, and it is specified for this blade coordinate system to be *governed* by the motion of the blade. That is, the local coordinate system follows the blade at each time-step during the cycle. Two point probes are then defined with respect to the blade coordinate system to be at the upper and lower blade surfaces exactly along the local x-direction axis. At each time-step, the global position vectors of each point probe are extracted and the mean of the position reading in each direction equates exactly to the location of the blade centroid in that direction. The computed centroid is then used as the pitch axis origin to assign the appropriate rate of pitch rotation at each time-step. For the current investigation, a pitch duration of 100 time-steps, or approximately 0.014s is used to carry out the desired pitch

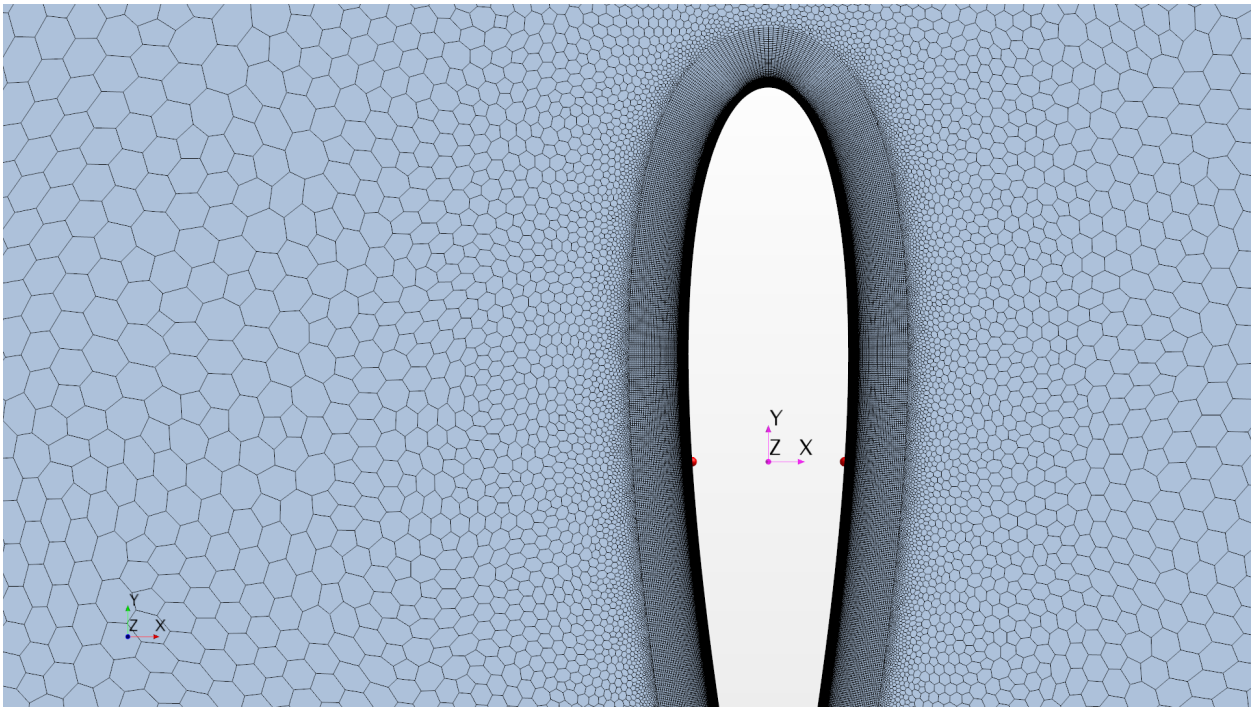

Figure 5.5: Local coordinate system and point probes for blade centroid tracking.

rotation. For example, a blade pitch of +5°equates to a rate of rotation of:

$$\dot{\phi} = \frac{5^\circ}{(\Delta t)(100 \text{ steps})} = \frac{0.08727 \text{ rad}}{(\Delta t)(100 \text{ steps})} = 6.25 \text{ rad/s}.$$

The temporal duration of blade pitching is a parameter that must be further investigated for detailed turbine design, with the 100 steps used in the current investigation taken to be an appropriate time period to prevent a drastic shock to the CFD solver and flow physics. An example of the user-defined field functions developed for implementing active-pitch is given in Appendix B.2. It should be noted here that the current body motion approach in STAR-CCM+ allows for only one non-zero velocity and rate of rotation to be assigned at each time-step. Thus, regions of active blade pitching are only possible during the beginning and ending of rectilinear motion regions, i.e. the East and West Translation regions.

The final converged CFD solution of the 1-blade D-VAWT baseline case is used as the input to all active-pitch simulations. After modifying the required blade motion specifications, the AP simulation is ran until a cyle-to-cycle C_P percent difference of $\leq 1\%$ is re-established.

5.3 Active-Pitch Control Results

Using the CFD tool developed, a number of active-pitch schemes are applied to the D-VAWT blade's motion. Although strategically selected beforehand, the magnitudes of pitch rotation and point of action within the cycle presents implications to the rotor flow physics that are unknown a priori.

5.3.1 Scheme 1

Computational fluid dynamics results have shown the baseline 1-blade D-VAWT to already produce impressive power extraction in the West Translation design region of interest, where the traditional point of peak tangential force for standard VAWTs is extended. With this in mind, the first active-pitch approach investigated is to alter the blade pitch to improve the aerodynamic performance in the downstream portion of the cycle. As evidenced by the inward fixed-pitch results in Section 5.1, a blade pitch with the trailing edge pointing inwards towards the rotor longitudinal axis will produce a favourable angle of attack to alleviate the negative C_P experienced in the South Rotation region while increasing the angle of attack in the East Translation region. To explore the potential efficiency improvements available in these regions, the first active-pitch scheme rotates the D-VAWT blade to the prescribed inward (negative) pitch angle at the end of the West Translation region, and returns the blade exactly to the original $\phi = 0°$ position at the end of the downstream East Translation. The pitching topology for Scheme 1 is presented visually in Figure 5.6.

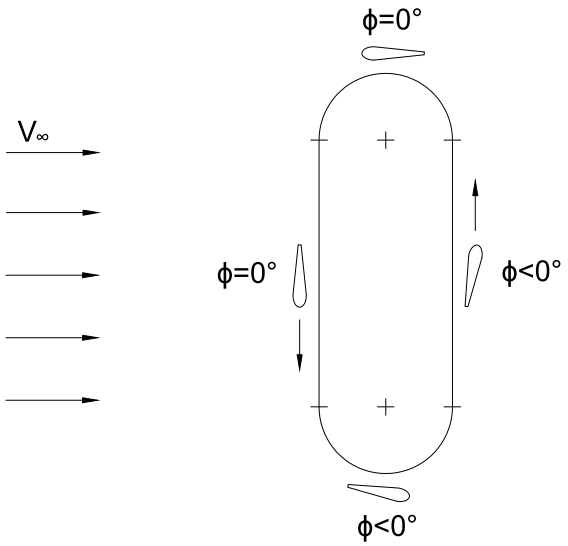

Figure 5.6: Active-pitch Scheme 1 topology.

Scheme 1a — 5° pitch

An active blade pitch angle of 5° is first investigated for the South and East regions. Although a pitch angle of this magnitude is known to be relatively large for a VAWT [20], since a strategically targeted active pitch approach is being used, $\phi = -5°$ is a suitable starting point for the analysis. The instantaneous C_P curves of the final AP Scheme 1a cycle and the baseline case are compared in Figure 5.7.

It is fruitful to examine Figure 5.7 on a per-region basis with respect to the D-VAWT cycle. During the North Rotation region of $0 < \frac{t}{T} < 0.2$, the C_P performance is quite similar. This is to be expected, since the blade's pitch is returned to exactly $\phi = 0°$ by the start of this region. The South Rotation ($0.5 < \frac{t}{T} < 0.7$) and East Translation ($0.7 < \frac{t}{T} < 1$) regions — where the blade is now pitched at $\phi = -5°$ — also produce readily-understood results, as the intent of the active pitching is indeed to improve the performance in these regions. However, during the West Translation at time $0.2 < \frac{t}{T} < 0.5$ — where the blade pitch is the baseline case of $\phi = 0°$ — a significant reduction in power extraction is noted compared to the baseline results. The reduction in power is so much so that the cycle-averaged C_P for this AP scheme is actually 3.70% *lower* than the baseline case, as shown in Table 5.1.

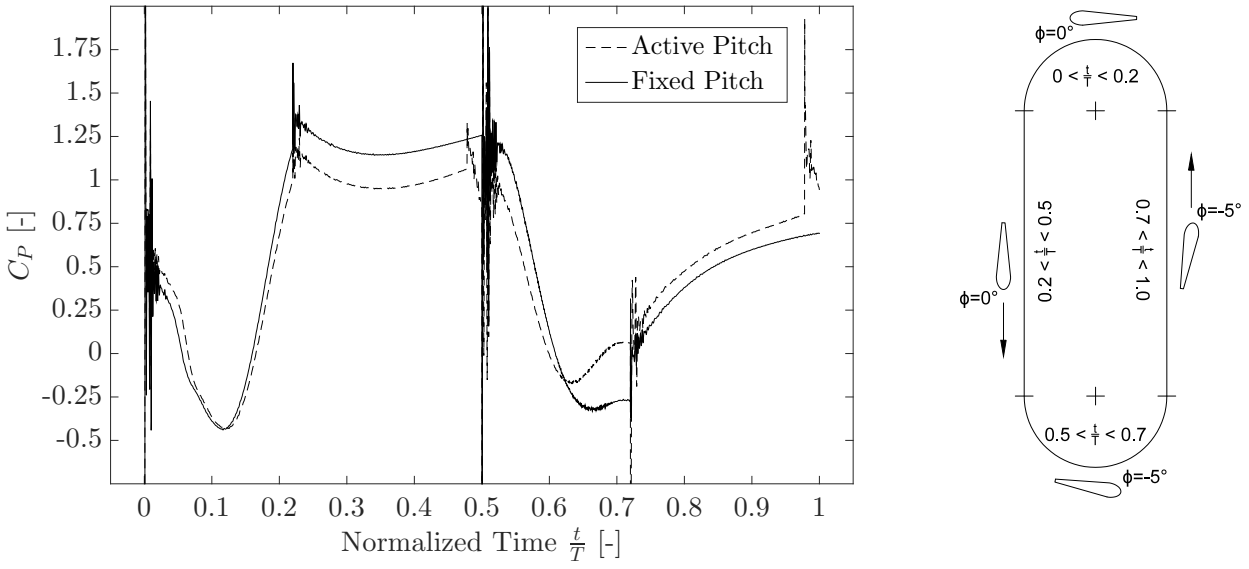

Figure 5.7: Active-pitch scheme 1a: Instantaneous C_P comparison.

Active-pitch Scheme 1a alters the blade pitch *only* in the South Rotation and East Translation regions of the turbine cycle, which are in the downstream half of the rotor. Therefore, it is peculiar to

Table 5.1: Active-pitch Scheme 1a cycle-averaged power coefficient.

Active-pitch Scheme 1a C_P	0.52
Fixed-pitch baseline C_P	0.54
Percent difference	-3.70%

observe such a drastic impact on the blade's power extraction during the optimal West Translation region, where under the current AP scheme the blade pitch is returned exactly to zero. This phenomenon can be explained by examining the incoming wind velocity upstream of the West Translation blade path.

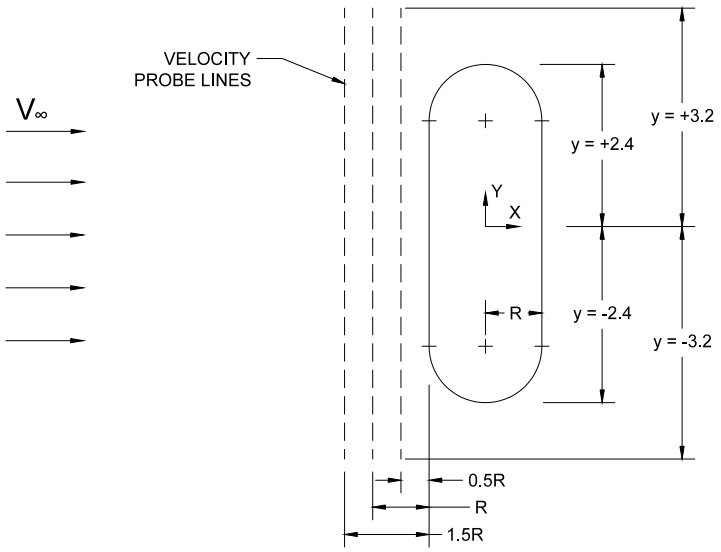

Figure 5.8: Upstream velocity probes topology.

The velocity profiles are all extracted using linear y-direction data probes in the velocity field at 0.5R, 1.0R and 1.5R upstream and parallel to the West Translation blade path. Figure 5.8 provides a schematic of the approach used. Vertical position $y = 0$ corresponds to the center of the D-VAWT rotor, with the rotor blade path extending until $y = \pm 2.4$ (the extremities of the North and South regions). The velocity data in Figure 5.9 is pulled at the point where the D-VAWT blade completes its final cycle, at the end of the East Translation region. Thus, the profiles shown are a revealing representation of the significant effect the downstream blade operation has on its upstream counterpart. The downstream-upstream influence is highlighted by focusing on the velocity profile at the closest vertical profile at a distance of 0.5R upstream of the West Translation

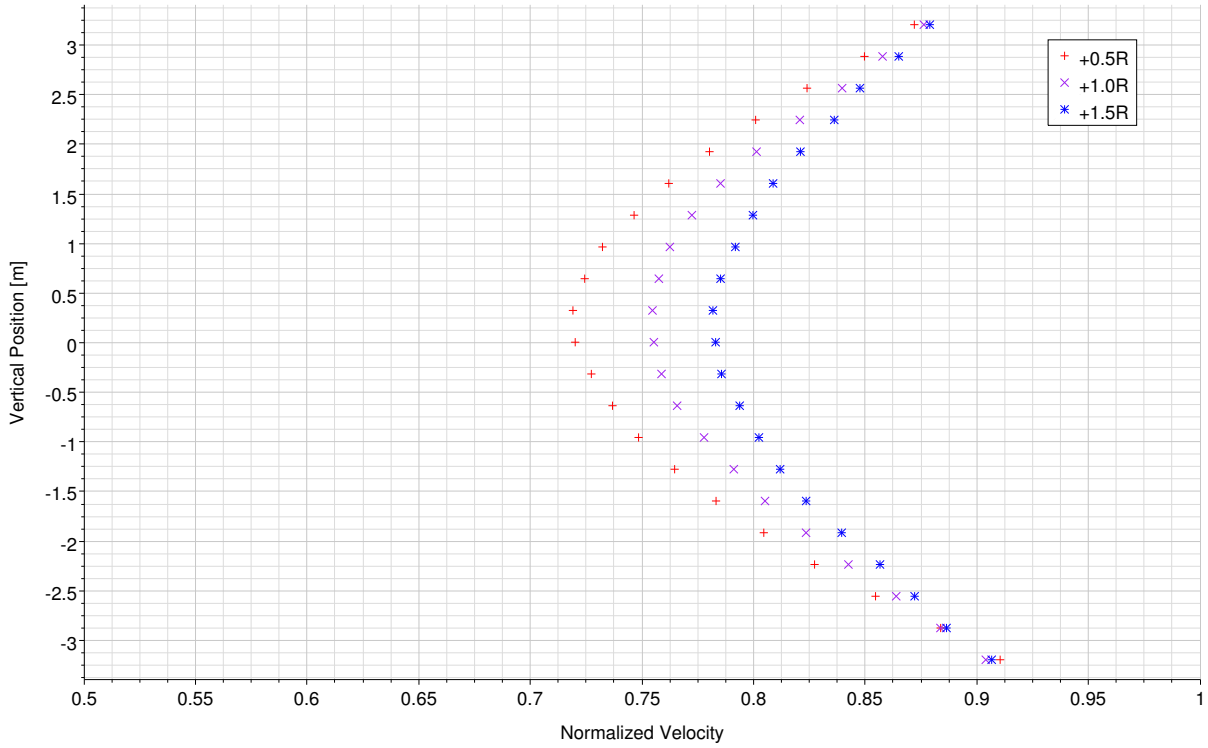

(a) Active-pitch Scheme 1a.

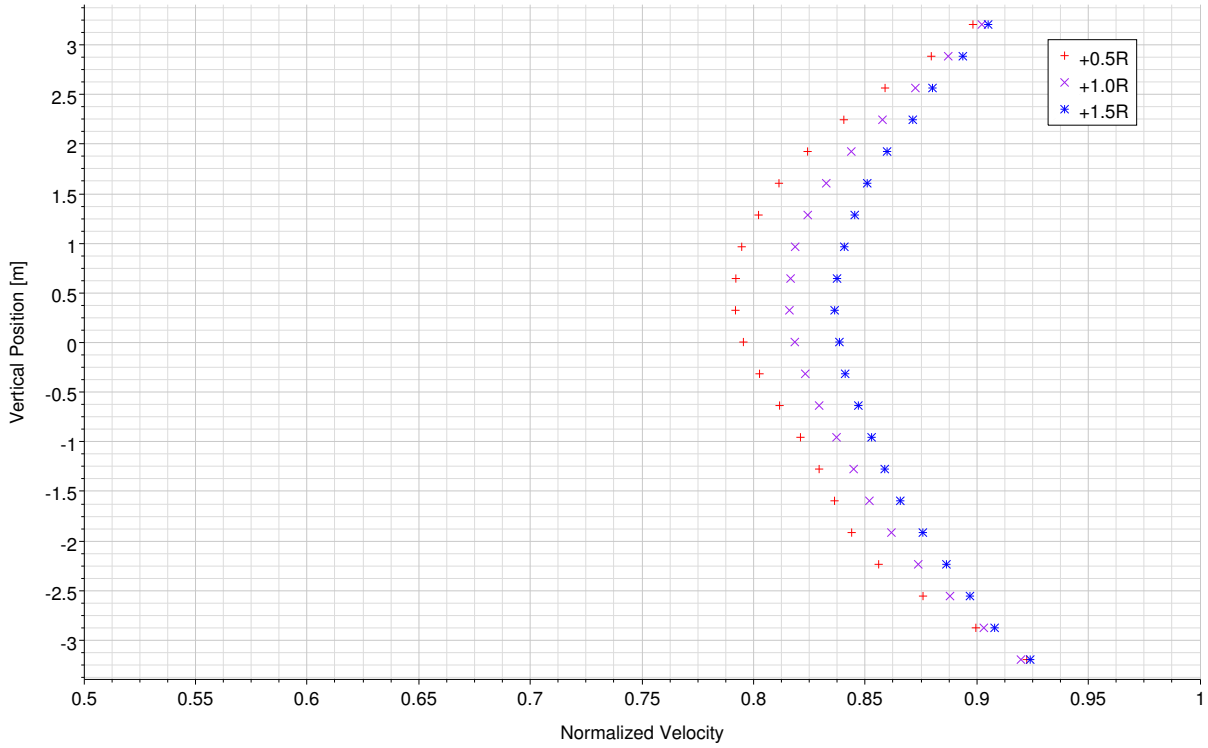

(b) Fixed-pitch baseline.

Figure 5.9: Active-pitch Scheme 1a: Incoming wind velocity to D-VAWT rotor.

path. Figure 5.10 overlays the 0.5R upstream AP1a and baseline FP velocity profiles, and provides the explanation for the reduction in power extraction experienced for the current scheme.

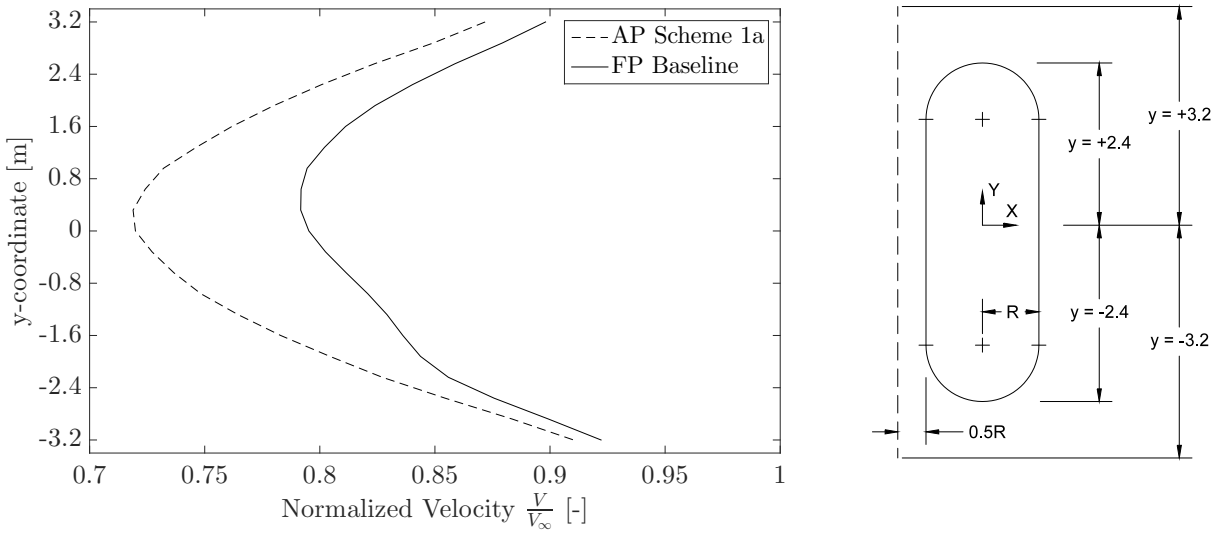

Figure 5.10: Active-pitch Scheme 1a: Incoming velocity profile at 0.5R upstream of West Translation.

Equation 4.2 is the underlying cubic relationship between the available power in the wind and its incoming velocity. Observing Figure 5.10, a remarkable reduction in the incoming velocity magnitude is present for the AP case. As the velocity profile is extracted at the end of the D-VAWT's cycle following the East Translation region — where for the current AP scheme the blade is pitched at $\phi = -5°$ — the blade's downstream aerodynamics appear to have a significant effect on the flow field upstream of the turbine rotor. Figure 5.11 is the incoming flow field's normalized velocity in the x-direction only. As expected, a significant variation in velocity magnitude is observed in the wake deficit of the turbine. However, the velocity experiences a non-negligible deviation from V_∞ *upstream* of the rotor and the crucial West Translation region. This reveals a rather striking and important behaviour of the incoming flow velocity, which is in fact notably *less* than the prescribed value — the freestream velocity value that the turbine is designed for.

Scheme 1b — 2° pitch

Heeding to the discovered interaction between the downstream and upstream flow fields, a similar scheme to AP1a is adopted but with the magnitude of the blade pitch reduced to $\phi = -2°$ in the South and East regions (the North and West regions are left at the $\phi = 0°$ baseline). The instantaneous C_P curve for AP Scheme 1b and its accompanying cycle-averaged C_P comparison

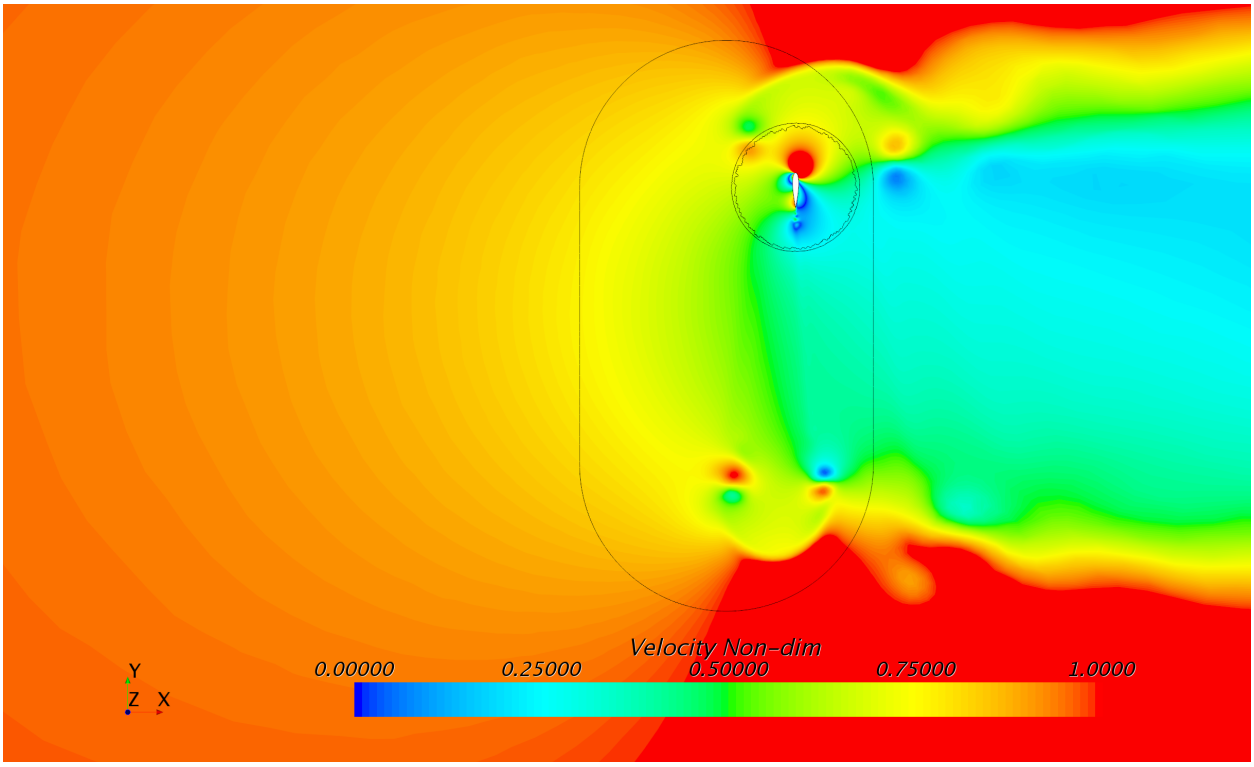

Figure 5.11: Active pitch scheme 1a: Normalized incoming velocity $\frac{V}{V_\infty}$ field.

are presented as Figure 5.12 and Table 5.2, respectively. A similar result to Scheme 1a is observed. Essentially, the trends are virtually the same and the magnitude of the difference between the AP and FP baseline is reduced. The negative impact on the West Translation's power extraction still causes an overall cycle-averaged C_P reduction of 1.85%.

Observing Figure 5.13, the incoming velocity profile follows a similar trend to Scheme 1a, albeit now marginally closer to the FP baseline. Under the safe assumption that a pitch angle of $\phi = -1°$ using the same scheme would just move the C_P curve closer to the baseline, another approach is instead adopted in an effort to counteract the physics observed in schemes AP 1a and 1b.

Table 5.2: Active-pitch Scheme 1b cycle-averaged power coefficient.

Active-pitch Scheme 1b C_P	0.53
Fixed-pitch baseline C_P	0.54
Percent difference	-1.85%

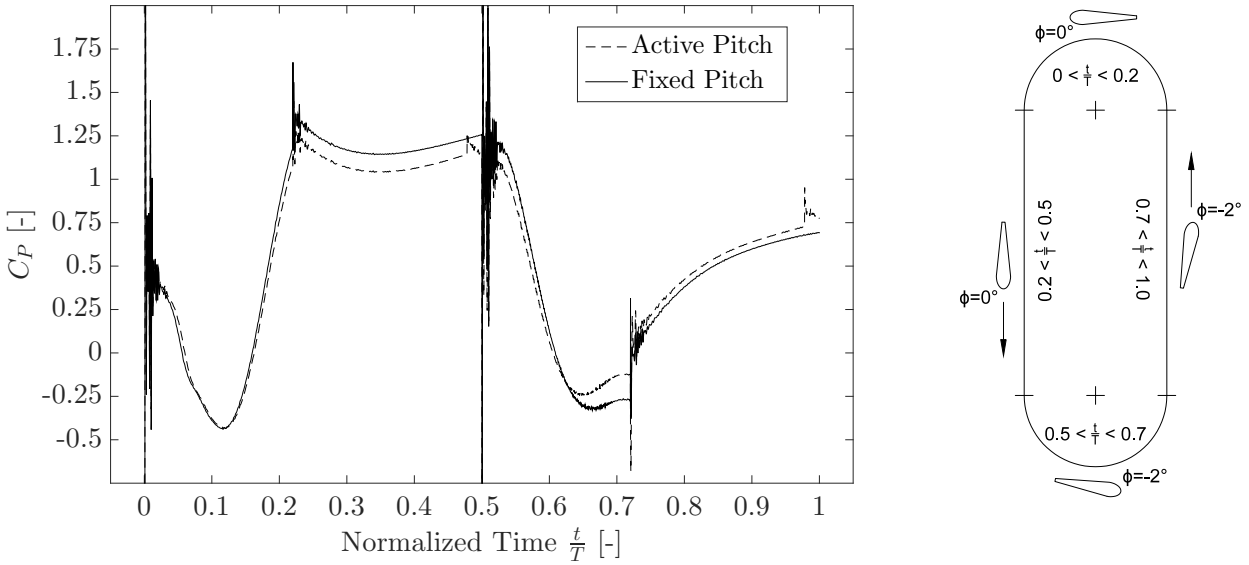

Figure 5.12: Active pitch scheme 1b: Instantaneous C_P comparison.

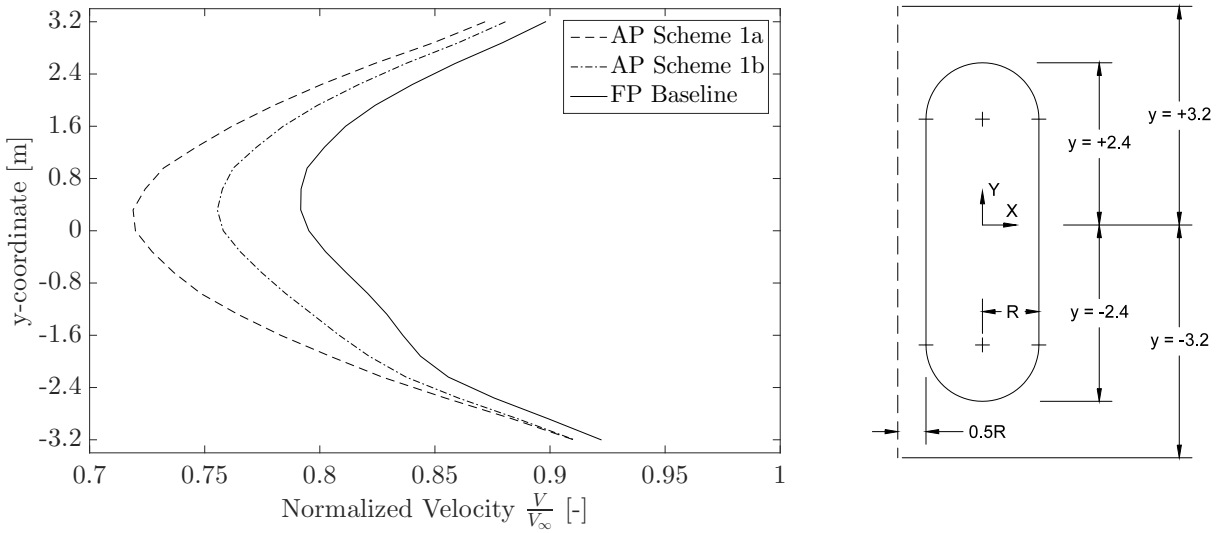

Figure 5.13: Active-pitch Scheme 1a & 1b: Incoming velocity profile at 0.5R upstream of West Translation.

5.3.2 Scheme 2

Active-pitch in the South and East regions demonstrates that improvements in power extraction can indeed be achieved at these points in the D-VAWT cycle, with the caveat being that additional power extraction downstream essentially reduces the useful incoming velocity component upstream. To counteract this negative effect, Scheme 1b is modified to include a blade pitch of $\phi = +2°$ in the West Translation region. Rotation of the trailing edge outwards with respect to the rotor center in this region has the effect of increasing the blade angle of attack, and thus the idea is to account for the decreased flow velocity by increasing the effective angle of attack through active-pitching. The TE-IN active-pitch of $\phi = -2°$ is left unchanged from Scheme AP1b, with the overall topology of Scheme 2 being depicted in Figure 5.14.

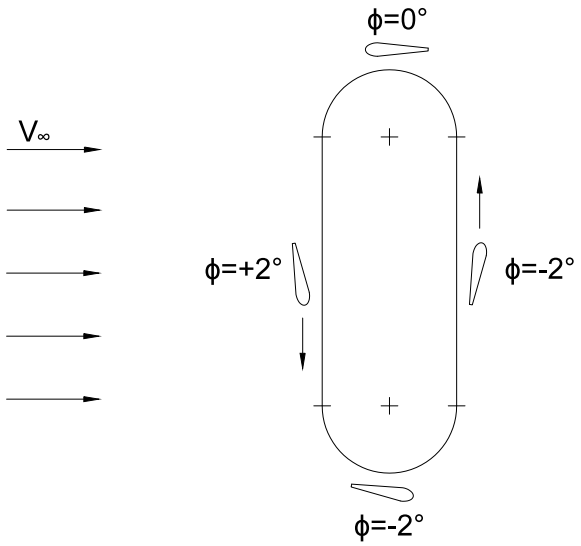

Figure 5.14: Active-pitch Scheme 2 topology.

The instantaneous power coefficient for Scheme AP2 is given in Figure 5.16. As a modification to Scheme AP1b, the only difference in the present active-pitch implementation is a blade pitch of $\phi = +2°$ in the West Translation region between $0.2 < \frac{t}{T} < 0.5$. In this region of interest, Figure 5.16 demonstrates that the power extraction of the blade is nearly recovered as compared to the FP baseline case. This is a notable finding, since the incoming velocity profile given as Figure 5.15 shows that a significant velocity deficit still remains for Scheme AP2. Consequently, the blade's ability to at least partially recover the power extraction performance in the West region is a testament to the power of pitch control. Comparing Scheme 2's Figure 5.16 and Scheme 1b's Figure 5.12, the South Rotation between $0.5 < \frac{t}{T} < 0.7$ is virtually unaffected by the introduction

of outward pitching in the West Translation region (Scheme 2).

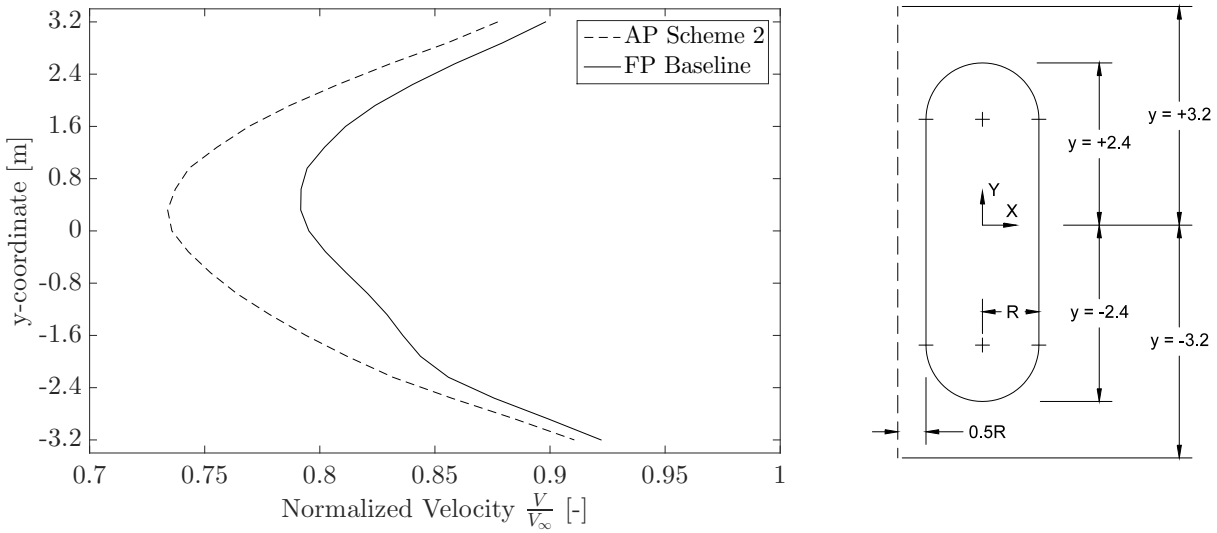

Figure 5.15: Active-pitch Scheme 2: Incoming velocity profile at 0.5R upstream of West Translation.

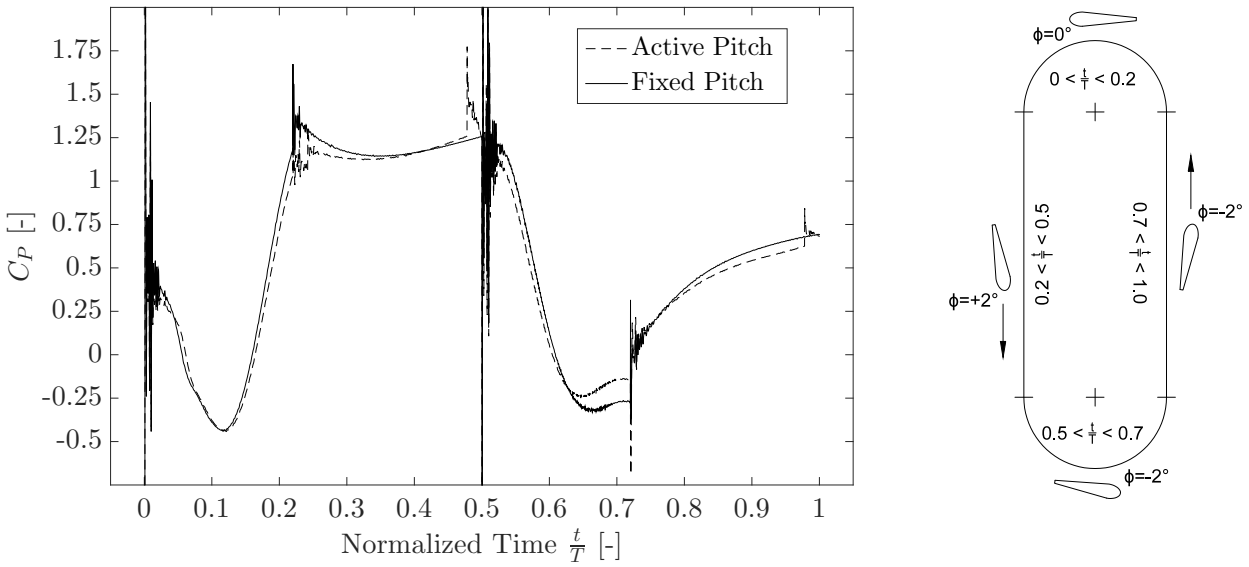

Figure 5.16: Active-pitch Scheme 2: Instantaneous C_P comparison.

However, the final blade region of $0.7 \leq \frac{t}{T} \leq 1$ in Figure 5.16 shows that the East Translation — directly downstream and parallel to the West Translation — is notably affected by the increased power extraction resulting from the blade's outward pitching and consequential larger angle of attack. The proximity of the upstream and downstream translation regions can be appreciated in Figure 5.17, where the effect of the West Translation's impressive performance is clearly visible on

the incoming flow ($V_\infty = 4\ m/s$) to the downstream East Translation region.

Table 5.3: Active-pitch Scheme 2 cycle-averaged power coefficient.

Active-pitch Scheme 2 C_P	0.52
Fixed-pitch baseline C_P	0.54
Percent difference	-3.70%

Similar to the upstream-downstream relationships uncovered in Scheme 1, the gain experienced in one region is essentially negated in the respective downstream or upstream region again in Scheme 2. Table 5.3 provides the cycle-averaged C_P for Scheme AP2, which still results in a decrease in overall performance from the fixed-pitch baseline. Despite Scheme AP2's improvement in the West Translation region, Figure 5.16 shows the strategic pitching in the downstream East Translation region is now rendered ineffective and is in fact less efficient that the fixed-pitch baseline case.

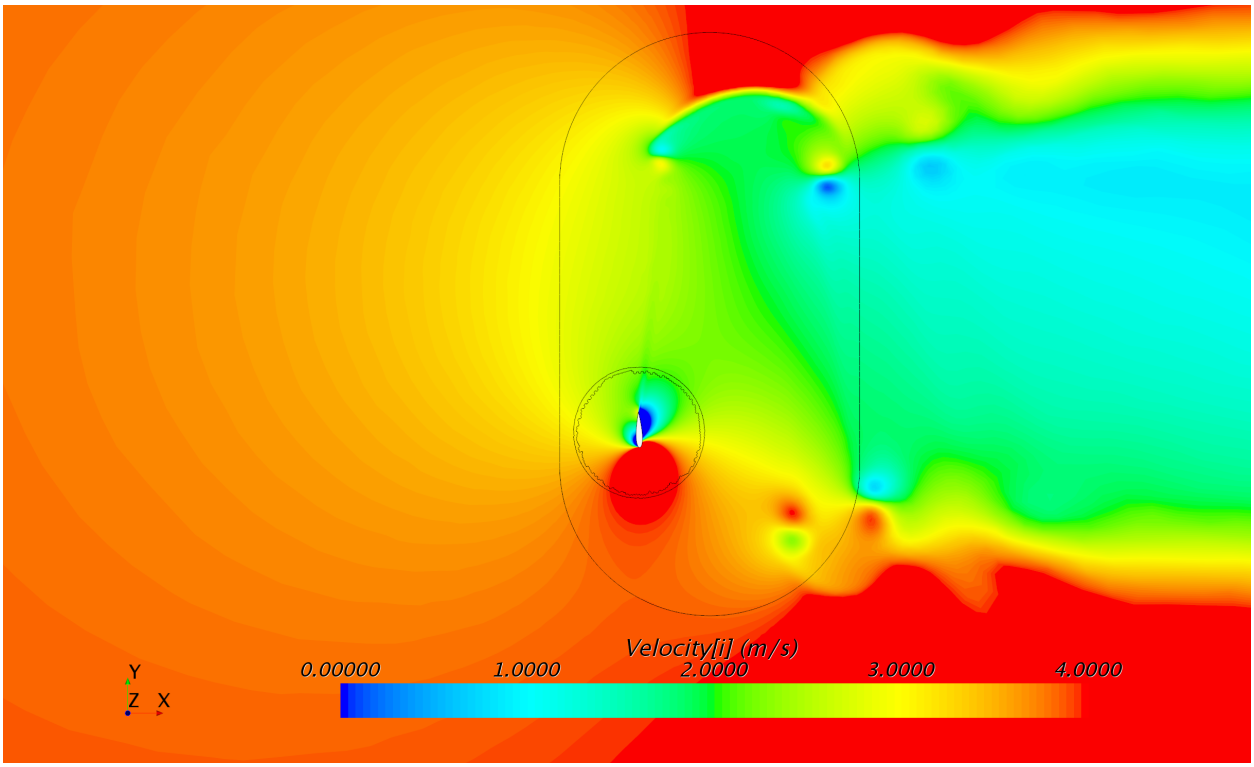

Figure 5.17: Active pitch scheme 2: V_x field following West Translation region.

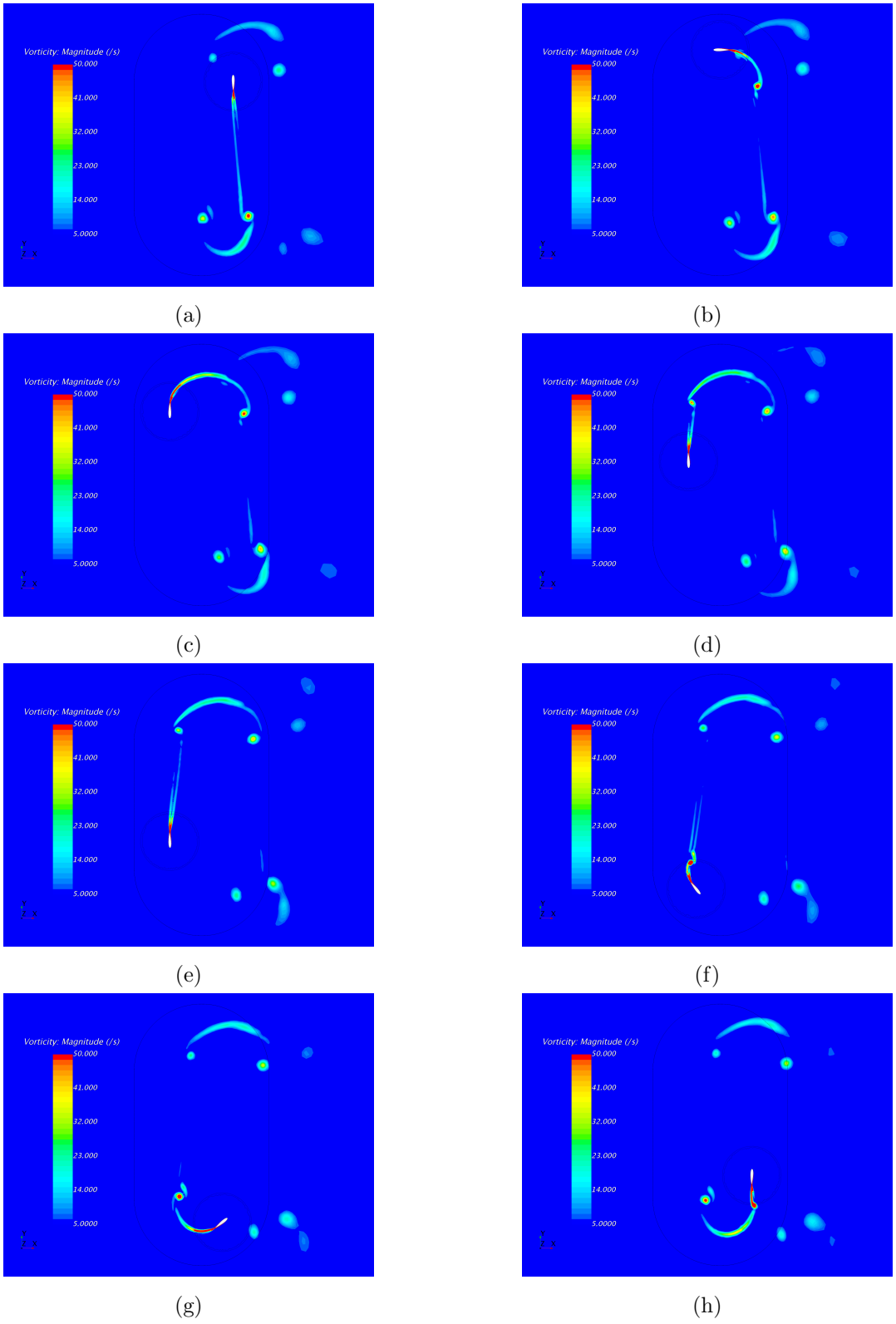

Figure 5.18: Vorticity development during one cycle of Scheme AP2.

5.3.3 Discussion

Due to its moderately high TSR of $\lambda = 4.5$, the D-VAWT experiences minimal vortex shedding. Even with the implementation of active blade pitching, as is shown in Figure 5.18 for Scheme AP2, there is essentially no interaction of vorticity between the upstream and downstream translation regions. Small vortices can be seen during the abrupt change from linear to rotational motion and vice versa, while the pitching mechanisms themselves introduce negligible shed vorticity to the overall rotor flow.

The negligible introduction of shed vorticity due to active-pitching suggests that there is additional interaction between the downstream blade fluid physics and the upstream. A comparison between the upstream incoming wind velocity for all active-pitch schemes is presented in Figure 5.19. The implementation of active-pitch control causes a more severe velocity deficit upstream of the D-VAWT rotor for all cases examined. Interestingly, the deficit is stronger for scheme AP1a when compared to scheme AP2, with the latter using an outward pitch angle of $\phi = +2°$ in the upstream West Translation region. This implies that the downstream East Translation inward pitch angle of $\phi = -5°$ could actually be more impactful on the incoming flow velocity than the smaller West Translation outward pitch angle.

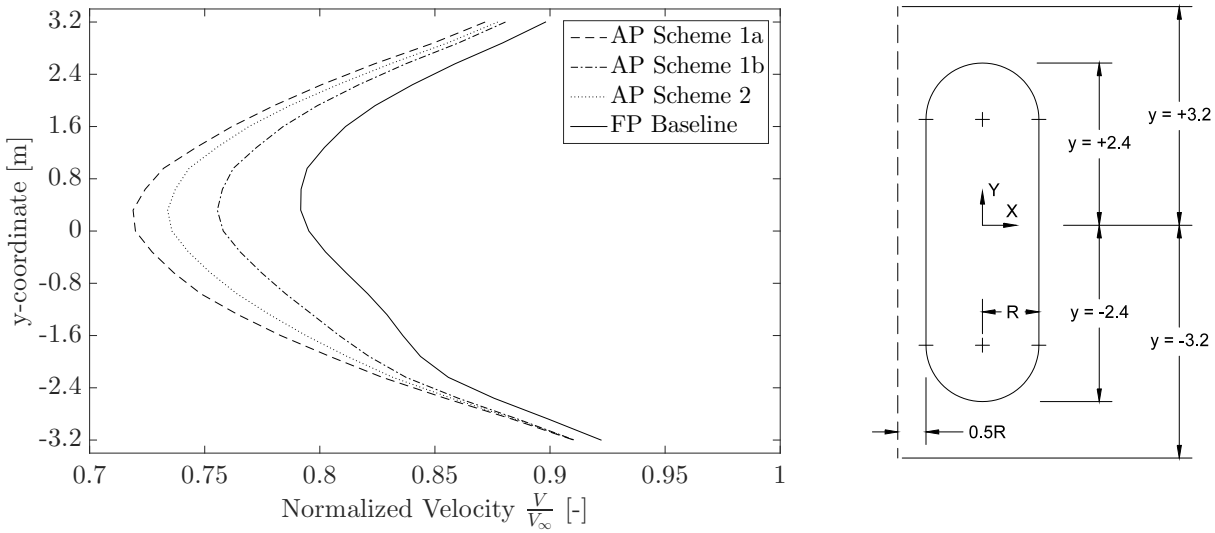

Figure 5.19: Comparison of active-pitch incoming velocity profiles at 0.5R upstream of West Translation.

Ultimately, the current 1-blade D-VAWT geometry is not conducive to active-pitch control due to the large chord-to-radius $\frac{c}{R}$ ratio and proximity of upstream to downstream translation regions.

In order for active-pitching to be a useful design improvement to the D-VAWT, the counter-action in aerodynamic performance of the West and East Translation regions needs to be minimized. This may or may not be possible, and will require future design work and analysis; the D-VAWT could potentially produce optimal flow physics under a straightforward fixed-pitch baseline regime. Despite the drop in overall C_P performance observed at present, the active-pitch schemes explored in the current investigation highlight the importance of the interaction between the upstream and downstream regions of the dual-vertical-axis wind turbine.

Chapter 6

Conclusion

A variety of aspects pertaining to the dual-vertical-axis wind turbine and its computational simulation are explored during the present scope of work. Useful contributions are made to the understanding of the D-VAWT's flow physics and developing a capable simulation environment using the STAR-CCM+ CFD package. Exciting areas of research remain to be explored, and are identified here for future investigators to continue.

6.1 Overview

Computational fluid dynamics is employed to study the effect of active-pitch implementation on a single-blade D-VAWT. The CFD environment is developed using the overset meshing approach in STAR-CCM+, and is validated through accurate prediction of the aerodynamics of a low tip speed ratio experimental vertical-axis wind turbine. The effect of controlling the blade pitch throughout the cycle is analyzed in detail, as well as the influence of the blade's pitching on other areas of the flow field. The cycle-averaged power coefficient of the current D-VAWT does not benefit from the implementation of active-pitch control, however the technique still offers opportunities pertaining to the turbine's operation and optimization.

6.2 Contributions

Techniques for accurate VAWT CFD Modeling at low TSR. Simulation of VAWTs operating at low TSRs is challenging, primarily due to the extensive vortex shedding and blade-vortex interaction in the flow field. The validation phase of the current investigation presents a proficient

CFD approach for accurately modeling this demanding flow situation. A thick region of smooth prism layers is required around the blade in order to properly capture the large (and often separated) boundary layer present in low TSR operation. To capture vortex roll-up and shedding — critical phenomena associated with the prediction of surface forces — a sufficiently large number of nodes (~ 1000) on the airfoil is recommended.

Validation of numerical methodology for overset mesh method. Overset meshing is indeed an excellent means of simulating bodies with complex motion definitions, however few reference cases are currently available in the literature or documentation. The successful modeling of the D-VAWT blade path offers a valuable example to the community. Polygonal meshing is found to be a suitable topology, and the overset-to-underset element size ratio of $\frac{l_o}{l_u} = 1/2$ is confirmed to be suitable for this type of external aerodynamics application. Interestingly, the fully-implicit coupled solver with active energy model is far superior with regards to residual behaviour compared to the traditional incompressible segregated approach.

User-defined code in STAR-CCM+. As a relatively new tool in academic research, at present few resources are available to provide relevant user code examples or troubleshooting for STAR-CCM+. The user code developed for the preliminary start-up analysis is provided with the intent to be an aid and starting point for future investigators. The code works in both serial and parallel, and demonstrates how to create the linkage between user code and simulation solver in the STAR-CCM+ environment.

Computational approach for arbitrary motion and centroid tracking. A manual method is developed to track the motion of an airfoil body throughout the rotor cycle, as a function of only the position vectors of two point probes aligned with a local coordinate system created at the body's geometric centroid. At present there is no other means of directly extracting this information from STAR-CCM+, thus the methodology developed here can be applied to a wide range of simulation scenarios where complex body motion is present.

Flow field interaction during active pitch control for the D-VAWT concept. Arguably the most important finding of the work — the level of power extraction in the downstream portion of the rotor has a non-negligible impact on the incoming flow field upstream of the turbine. A reduction of incoming flow velocity can lead to a substantial reduction in aerodynamic power

extraction, following the cubic relationship between the two parameters. This is crucial for the D-VAWT, but also relevant to traditional vertical-axis turbines. Further power extraction could be possible for VAWT-style turbines knowing that the incoming wind could in fact be slower than the freestream value the turbine is originally designed for. The interaction between upstream and downstream rotor regions has hitherto not been understood in terms of the D-VAWT and is often not considered for VAWT design.

Active-pitch is able to equilibrate load but not able to increase power extraction. Due to the discovered flow field interaction, active-pitch is unable to improve the cycle-averaged power coefficient for the present turbine. However, drastic variations in aerodynamic loading are experienced as the D-VAWT blade moves through its cycle. Although outside the scope of the current study, structural loading is an imperative consideration for a holistic wind turbine design. Active-pitch control could be used as a means of decreasing potential structural damage due to overbearing variations in loading throughout the rotor cycle.

6.3 Future Work

Active blade pitch with optimized D-VAWT geometry. Active pitch still certainly has potential with the D-VAWT. To decrease the proximity of the upstream and downstream regions, increasing the rotor radius should be investigated. Reduction of the chord-to-radius ratio is also hypothesized to favour active-pitch implementation, as this geometric modification would reduce flow curvature effects.

Multi-blade active pitch control. All D-VAWT simulations presented use only a single blade. The effect of multiple blades on the efficiency of active-pitch would be a necessary investigation for a complete assessment of this design option.

Active blade pitch for start-up. During start-up, the blades of a VAWT are often in starting positions that do not produce any positive torque to contribute to the rotor's initial motion. The D-VAWT introduces two large linear regions where the blades are now perpendicular to the incoming wind, or at the quasi $\theta = \pm 90°$ azimuth position. Making use of active-pitch in these regions to increase a blade's positive tangential force could have a notable impact on the D-VAWT's ability to overcome its inertia and set the rotor in motion.

Active blade pitch for variable wind directions. Its unique linear translation regions cause the D-VAWT's performance to be susceptible to changes in incoming wind direction. To alleviate this disadvantage — which could be especially important for a large-scale sized D-VAWT — active-pitch control could be employed with microprocessors to react to changes in incoming wind direction and adjust individual blade pitch for optimal power extraction.

References

[1] "The energy report: 100% renewable by 2050," The World Wide Fund for Nature, Gland, Switzerland, Tech. Rep., 2011.

[2] P. Hawken, *Drawdown: The most comprehensive plan ever proposed to reverse global warming.* Penguin Books, 2017.

[3] International Energy Agency, "World energy investment 2017," URL: https://www.iea.org/publications/wei2017/, July 2017.

[4] D. Bogdanov and C. Breyer, "North-east asian super grid for 100% renewable energy supply: Optimal mix of energy technologies for electricity, gas and heat supply options," *Energy Conversion and Management*, vol. 112, pp. 176–190, 2016.

[5] D. Connolly, H. Lund, and B. Mathiesen, "Smart energy europe: The technical and economic impact of one potential 100% renewable energy scenario for the european union," *Renewable and Sustainable Energy Reviews*, vol. 60, pp. 1634–1653, 2016.

[6] P. Gipe, *Wind Energy Comes of Age*, ser. The Wiley Series in Sustainable Design. Wiley, 1995.

[7] T. Andresen, "Offshore wind farms offer subsidy-free power for first time," URL: https://www.bloomberg.com/news/articles/2017-04-13/germany-gets-bids-for-first-subsidy-free-offshore-wind-farms, Bloomberg, April 2017.

[8] "Short-term energy outlook," U.S. Energy Information Administration, Tech. Rep., July 2017.

[9] "Annual energy outlook 2017," U.S. Energy Information Administration, Tech. Rep., January 2017.

[10] "Global wind report 2016," Global Wind Energy Council, Tech. Rep., 2017.

[11] "Energy fact book 2016-2017," Natural Resources Canada, Tech. Rep., 2017.

[12] J. D. Anderson, *Fundamentals of Aerodynamics*, 3rd ed., ser. Aeronautical and aerospace engineering. McGraw-Hill, 2001.

[13] A. P. Schaffarczyk, *Introduction to Wind Turbine Aerodynamics*, ser. Green Energy and Technology. Springer, 2014.

[14] S. Eriksson, H. Bernhoff, and M. Leijon, "Evaluation of different turbine concepts for wind power," *Renewable and Sustainable Energy Reviews*, vol. 12, no. 5, pp. 1419–1434, 2008.

[15] B. K. Kirke, "Evaluation of self-starting vertical axis wind turbines for stand-alone applications," Ph.D. dissertation, Griffith University, Gold Coast Campus, 1998.

[16] U. S. Paulsen, M. Borg, H. A. Madsen, T. F. Pedersen, J. Hattel, E. Ritchie, C. S. Ferreira, H. Svendsen, P. A. Berthelsen, and C. Smadja, "Outcomes of the deepwind conceptual design," *Energy Procedia*, vol. 80, pp. 329–341, 2015.

[17] E. Dyachuk, M. Rossander, A. Goude, and H. Bernhoff, "Measurements of the aerodynamic normal forces on a 12-kw straight-bladed vertical axis wind turbine," *Energies*, vol. 8, no. 8, pp. 8482–8496, 2015.

[18] M. Paraschivoiu, M. Komeili, and S. N. Zadeh, "Mesh convergence study for 2-D straight-blade vertical axis wind turbine simulations and estimation for 3-D simulations," *Transactions of the Canadian Society for Mechanical Engineering,*, vol. 38, no. 4, 2014.

[19] P. A. Kozak, D. Vallverdú, and D. Rempfer, "Modeling vertical-axis wind turbine performance: Blade element method vs. finite volume approach," in *To be submitted in the In Proceedings of The AIAA Propulsion and Energy Forum and Exposition*, vol. 2014, 2014.

[20] R. Gosselin, G. Dumas, and M. Boudreau, "Parametric study of H-darrieus vertical-axis turbines using uRANS simulations," *Paper CFDSC-2013*, vol. 178, pp. 6–9, 2013.

[21] G. Naccache, "CFD based analysis and parametric study of a novel wind turbine design: the dual vertical axis wind turbine," Master's thesis, Concordia University, 2016.

[22] O. Kikanov, *Essential Computational Fluid Dynamics*. Wiley, 2010.

[23] F. Balduzzi, A. Bianchini, R. Maleci, G. Ferrara, and L. Ferrari, "Critical issues in the CFD simulation of darrieus wind turbines," *Renewable Energy*, vol. 85, pp. 419–435, 2016.

[24] P. A. Davidson, *Turbulence: An Introduction for Scientists and Engineers*, 2nd ed. Oxford University Press, 2015.

[25] D. C. Wilcox, *Turbulence Modeling for CFD*, 3rd ed. DCW Industries, 2006.

[26] F. Menter, "Influence of freestream values on k turbulence model predictions," *AIAA J*, vol. 30, no. 6, pp. 1657–1659, 1992.

[27] F. Menter, M. Kuntz, and R. Langtry, "Ten years of industrial experience with the SST turbulence model," *Turbulence, heat and mass transfer*, vol. 4, no. 1, pp. 625–632, 2003.

[28] M. O. L. Hansen, *Aerodynamics of Wind Turbines*, 2nd ed. Earthscan, 2008.

[29] R. Howell, N. Qin, J. Edwards, and N. Durrani, "Wind tunnel and numerical study of a small vertical axis wind turbine," *Renewable energy*, vol. 35, no. 2, pp. 412–422, 2010.

[30] R. Gerakopulos, M. S. Boutilier, and S. Yarusevych, "Aerodynamic characterization of a NACA 0018 airfoil at low reynolds numbers," *AIAA paper*, vol. 4629, 2010.

[31] C. Simão Ferreira, A. Van Zuijlen, H. Bijl, G. Van Bussel, and G. Van Kuik, "Simulating dynamic stall in a two-dimensional vertical-axis wind turbine: verification and validation with particle image velocimetry data," *Wind Energy*, vol. 13, no. 1, pp. 1–17, 2010.

[32] C. S. Ferreira, G. Van Kuik, G. Van Bussel, and F. Scarano, "Visualization by PIV of dynamic stall on a vertical axis wind turbine," *Experiments in Fluids*, vol. 46, no. 1, pp. 97–108, 2009.

[33] N. Qin, R. Howell, N. Durrani, K. Hamada, and T. Smith, "Unsteady flow simulation and dynamic stall behaviour of vertical axis wind turbine blades," *Wind Engineering*, vol. 35, no. 4, pp. 511–527, 2011.

[34] I. Paraschivoiu, *Wind Turbine Design: With Emphasis on Darrieus Concept*. Polytechnic International Press, 2002.

[35] P. C. Klimas and M. H. Worstell, "Effects of blade preset pitch/offset on curved-blade darrieus vertical axis wind turbine performance," Sandia National Laboratories, Albuquerque, New Mexico, Tech. Rep. SAND-81-1762, 1981.

[36] R. E. Sheldahl, P. C. Klimas, and L. V. Feltz, "Aerodynamic performance of a 5-metre-diameter darrieus turbine with extruded aluminum NACA-0015 blades," Sandia National Laboratories, Albuquerque, New Mexico, Tech. Rep. SAND80-0179, 1980.

[37] S. Armstrong, A. Fiedler, and S. Tullis, "Flow separation on a high reynolds number, high solidity vertical axis wind turbine with straight and canted blades and canted blades with fences," *Renewable Energy*, vol. 41, pp. 13–22, 2012.

[38] M. Benedict, V. Lakshminarayan, J. Pino, and I. Chopra, "Aerodynamics of a small-scale vertical-axis wind turbine with dynamic blade pitching," *AIAA Journal*, 2015.

[39] Siemens, *STAR-CCM+ User Guide, Version 12.02A*, Siemens PLM Software, 2017.

[40] J. Anderson and J. e. Wendt, *Computational Fluid Dynamics: An Introduction*, 3rd ed. Springer, 2009.

[41] P. K. Kundu, I. M. Cohen, and D. R. Dowling, *Fluid Mechanics*, 5th ed. Elsevier Academic Press, 2012.

[42] F. R. Menter *et al.*, "Two-equation eddy-viscosity turbulence models for engineering applications," *AIAA journal*, vol. 32, no. 8, pp. 1598–1605, 1994.

[43] H. Schlichting and K. Gersten, *Boundary-Layer Theory*, 9th ed. Springer, 2017.

[44] ANSYS, *ANSYS Fluent User Guide, Release 12.0*, ANSYS Fluent, 2009.

[45] P. A. Durbin and G. Medic, *Fluid Dynamics with a Computational Perspective*. Cambridge University Press, 2007.

[46] É. Gauthier, "Oscillating-foils hydrokinetic turbine performance prediction: Impact of turbulence modeling, of structure interference and of confinement," Master's thesis, Université Laval, 2015.

[47] P. Kozak, "Effects of unsteady aerodynamics on vertial-axis wind turbine performance," Master's thesis, Illinois Institute of Technology, 2014.

[48] D. Castelein, "Dynamic stall on vertical axis wind turbines," Master's thesis, TU Delft, 2015.

[49] G. Naccache and M. Paraschivoiu, "Parametric study of the dual vertical axis wind turbine using CFD," *Accepted in Journal of Wind Engineering & Industrial Aerodynamics*, 2017.

[50] A. Bianchini, L. Ferrari, and S. Magnani, "Start-up behavior of a three-bladed H-darrieus vawt: experimental and numerical analysis," *ASME Paper No. GT2011-45882*, 2011.

[51] W. Chong, A. Fazlizan, S. Poh, K. Pan, W. Hew, and F. Hsiao, "The design, simulation and testing of an urban vertical axis wind turbine with the omni-direction-guide-vane," *Applied Energy*, vol. 112, pp. 601–609, 2013.

[52] R. Dominy, P. Lunt, A. Bickerdyke, and J. Dominy, "Self-starting capability of a darrieus turbine," *Proceedings of the Institution of Mechanical Engineers, Part A: Journal of Power and Energy*, vol. 221, no. 1, pp. 111–120, 2007.

[53] N. Hill, R. Dominy, G. Ingram, and J. Dominy, "Darrieus turbines: the physics of self-starting," *Proceedings of the Institution of Mechanical Engineers, Part A: Journal of Power and Energy*, vol. 223, no. 1, pp. 21–29, 2009.

[54] A. Untaroiu, H. G. Wood, P. E. Allaire, and R. J. Ribando, "Investigation of self-starting capability of vertical axis wind turbines using a computational fluid dynamics approach," *Journal of Solar Energy Engineering*, vol. 133, no. 4, p. 041010, 2011.

[55] M. T. Asr, E. Z. Nezhad, F. Mustapha, and S. Wiriadidjaja, "Study on start-up characteristics of H-darrieus vertical axis wind turbines comprising NACA 4-digit series blade airfoils," *Energy*, vol. 112, pp. 528–537, 2016.

[56] A. Rossetti and G. Pavesi, "Comparison of different numerical approaches to the study of the H-darrieus turbines start-up," *Renewable Energy*, vol. 50, pp. 7–19, 2013.

[57] S. Worasinchai, G. L. Ingram, and R. G. Dominy, "The physics of H-darrieus turbine starting behaviour," in *Proceedings of the ASME Turbo Expo*, 2014.

[58] R. E. Sheldahl and P. C. Klimas, "Aerodynamic characteristics of seven symmetrical airfoil sections through 180-degree angle of attack for use in aerodynamic analysis of vertical axis wind turbines," Sandia National Laboratories, Albuquerque, New Mexico, Tech. Rep. SAND80-2114, 1981.

Appendix A

D-VAWT Start-Up Considerations

Start-up is one of the most important design criteria for a vertical-axis wind turbine. Addressing the D-VAWT's ability to self-start is a crucial question to its feasibility as a practical wind energy device. Due to the extreme computational resources and simulation time required to accurately simulate a turbine's start-up, the present start-up analysis is strictly preliminary and provides the basis for simulating the process in the STAR-CCM+ CFD environment.

A.1 Literature Review: The Self-Starting Ability of VAWTs

Various definitions of a turbine's ability to self-start can be found, but at present the criteria set by Bianchini et al. [50] seems to be the most meaningful. In this definition, a VAWT is considered self-starting if, in the absence of external assistance and under fixed incoming wind conditions, it is able to ramp up its rotor velocity until the steady-state rotation rate (i.e. TSR) is achieved. The Darrieus VAWT's ability to self-start is one of the main concerns brought forward when discussing the viability of the design. Historically, with the exception of rare wind conditions, classical Darrieus VAWTs are known to be not self-starting devices, and thus a motor is required to initially reach the turbine's operational speed [6].

However, the recent resurgence in VAWT research has shown more hope for the starting capability of the H-rotor Darrieus. In an exciting experimental investigation from Chong et al. [51], a potentially impactful omni-direction-guide-vane (ODGV) is designed and tested. Under the wind tunnel conditions tested, this VAWT augmentation device reduced the self-starting speed of a 5-blade, cambered airfoil turbine from 7.35 m/s to 4.0 m/s. A conceptual rendition of the patented ODGV is shown in Figure A.1.

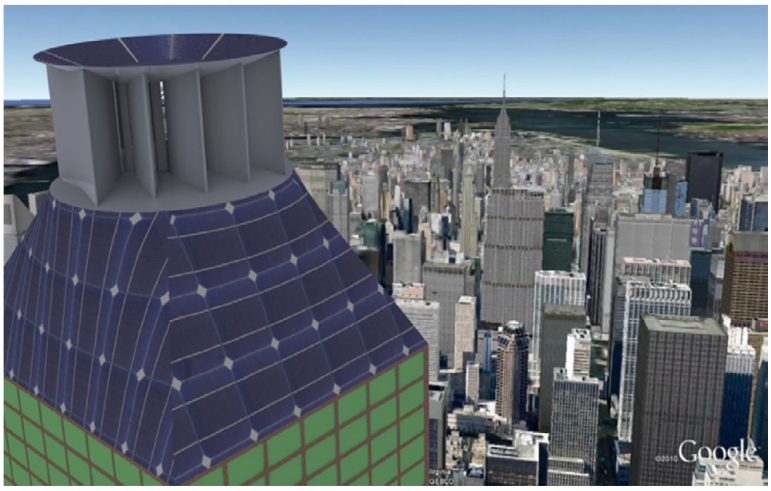

Figure A.1: Artistic rendition of the recently conceived omni-direction-guide-vane VAWT enhancement mounted on a high rise building [51].

In a study using numerical aerodynamics, Dominy et al. [52] show that a three-blade, symmetric airfoil H-rotor in fixed incoming wind is indeed self-starting for all initial blade positions, while the two-blade turbine's self-starting capability can be dependent on blade starting positions. This work is continued by Hill, Dominy et al. [53] with their often-referenced wind tunnel and numerical study on the self-starting characteristic of a three-blade H-rotor VAWT. This investigation reveals, with the finding provided in Figure A.2, the four stages of VAWT start-up behaviour:

1. An approximate linear increase in TSR from rest, initially influenced by simple drag pushing on the blades.

2. A plateau region where there is very little change in TSR.

3. A rapid increase in TSR, at which point the turbine's rotation is now dominated by the lift force of the blades.

4. Quasi steady-state operation at the final TSR.

Detailed physical interpretation of these regions is provided by Untaroiu et al. [54] as part of their CFD effort to model the experimental turbine setup of Hill et al. [53]. The computational model produced a large underestimation of the time required for start-up, which is hypothesized to be at least partially due to the selection of the $k-\varepsilon$ turbulence model instead of the more adept $k-\omega$. An improved CFD representation of the experimental start-up data [53] is achieved by Asr

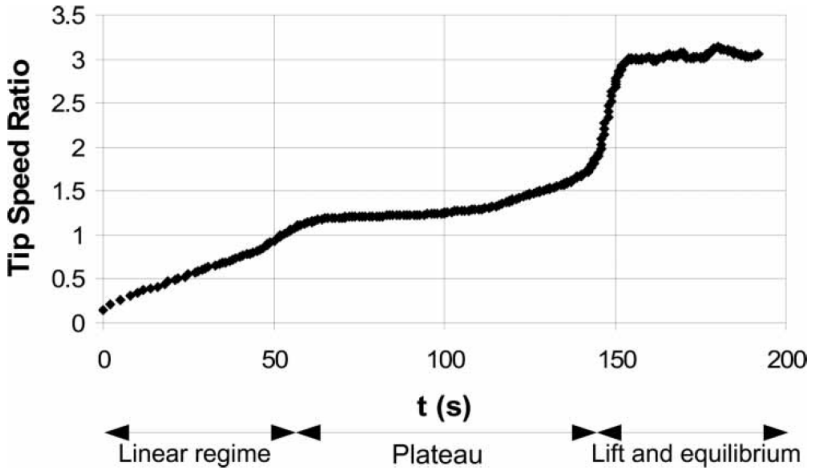

Figure A.2: The starting TSR-characteristic of a vertical-axis wind turbine [53].

et al. [55]. Here, the $k-\omega$ SST turbulence model is employed and this time a comparable start-up characteristic curve is observed. In their study on the same turbine geometry as Hill's [53], Rossetti and Pavesi [56] find success with using the new SAS turbulence model to overcome the shortcomings of the RANS approach. Interestingly, at tip speed ratio $\lambda = 1$, the mean average torque for the 3D CFD model is significantly greater (in the positive direction) than that seen for the 2D model, suggesting that 3D flow effects could actually have a beneficial impact for low TSR and start-up operation. Worasinchai et al. [57] provide a biologically-inspired interpretation of the self-starting physics by comparing the H-Darrieus' blade path to that of the flapping of a bird's wing. From the currently available literature, it can be confidently said that the flow physics associated with the starting of a VAWT are quite complex and their prediction using computational techniques — especially with regards to turbulence modeling — remains to be a challenging task.

A.2 Starting Position Static Analysis

At rest, a VAWT encounters its greatest challenge to produce sufficient aerodynamic force to put the rotor into motion. This is a causal effect of the lack of blade velocity, V_b, present in the relative wind velocity vector triangle acting on the blade, which drastically changes the aerodynamics of the blade. Naturally, the rotor must also overcome the initial inertial restraint to begin rotating.

Despite the difficulties associated with VAWT start-up, the physics are not insurmountable. Figure A.3 presents experimental data of the tangential force coefficient generated over a static NACA0018 blade under a Reynolds number of $Re = 80,000$ [58]. At the special case of turbine

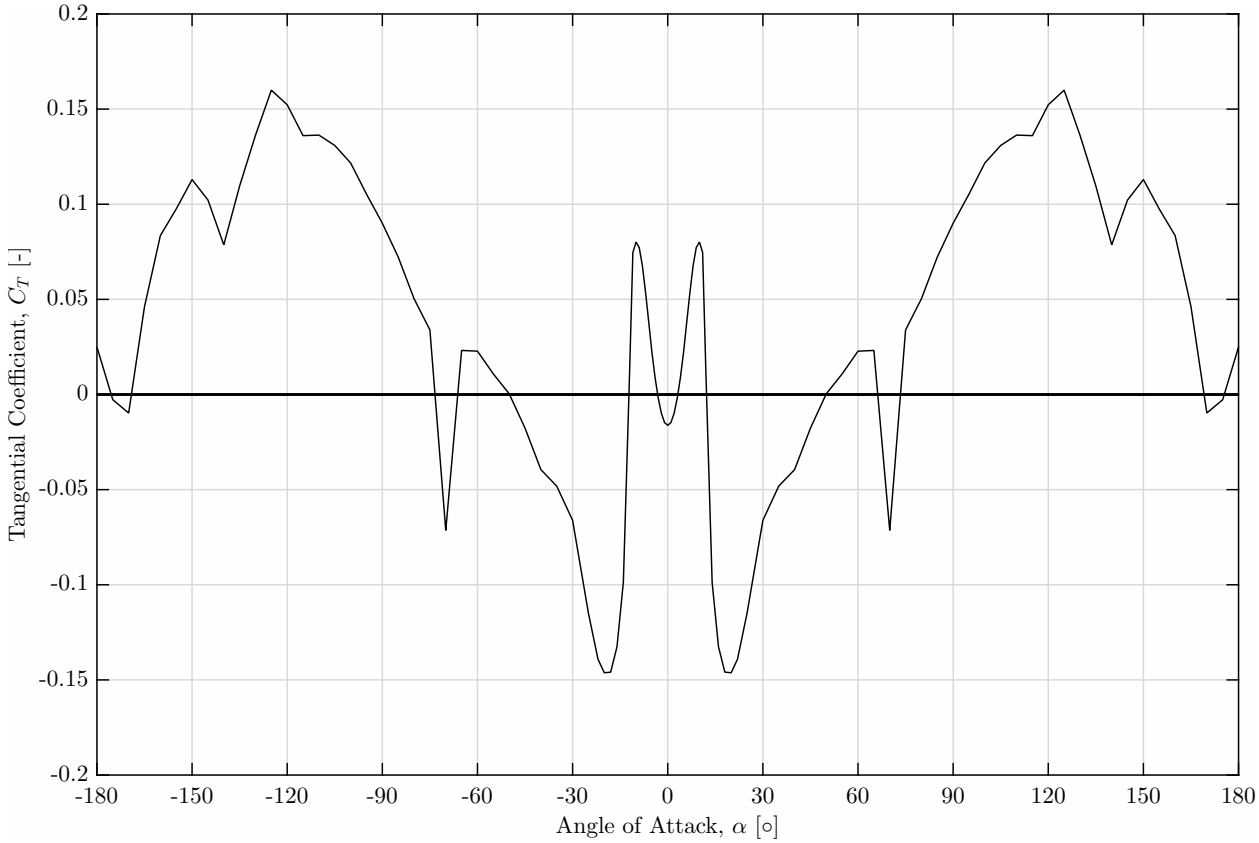

Figure A.3: Static wind tunnel NACA0018 tangential coefficients at Reynolds number $Re = 80,000$. Data courtesy of Sandia Labs [58].

rotor start-up, where the tip-speed ratio is $\lambda \approx 0$, the blade motion induces essentially no wind velocity component, and thus the relative velocity acting on the blade is simply the incoming free-stream wind velocity. Considering this, the azimuth angle position of the blade is effectively the same as the angle of attack depicted on the x-axis of Figure A.3, where angles of attack for $\alpha > 0°$ correspond to the downstream half of the rotor and $\alpha < 0°$ to the upstream [53]. The important takeaway from this quasi static perspective and Figure A.3 is that there is a considerable range of angles of attack between $0° \leq \alpha \leq \pm 180°$ for which the tangential coffecient C_T is greater than zero. A $C_T > 0$ represents a generation of aerodynamic force in the direction of desired motion, and thus is a net positive contributor to the effort of rotor start-up. This notion of the importance of blade starting position on VAWT start-up ability is thoroughly explored by Dominy et al. [52], who examine the start-up cability of VAWTs as a function of the blade's starting position in the rotor cycle and the turbine's number of blades.

A.3 Computational Approach

At the time of the current investigation, a severe paucity of STAR-CCM+ user code cases are available to be used as reference examples. Accordingly, the intent here is to provide a brief explanation of the code developed for simulating VAWT start-up using STAR-CCM+, such that future researchers can avail of it as a starting point for similar undertakings. All source code generated is provided in Appendix B.3. Included is the actual computational source file, `VAWTstart.c`, as well as the two complementary files required for STAR-CCM+ user code implementation. The header file, `uclib.h`, is essentially generic and can be found in the STAR-CCM+ documentation [39], while `uclib.c` is the library defintion file and specifies the user-defined functions within the code as well as the solver variables to be extracted from the simulation.

The code and simulation environment developed is a computational representation of the experimental VAWT start-up case of Hill et al. [53]. To investigate start-up numerically, instead of assigning a fixed velocity to the blade or rotor, the computed forces are used to determine the acceleration and resulting motion at each time-step. Respective fundamental equations of motion are solved in the user code environment depending on the blade being in a translation or rotational region. Untaroui et al. [54] provide a mathematical description of this approach, which can be summarized as:

$$\ddot{\theta}^{N+1} = \frac{M_z^N}{I} \tag{A.1}$$

$$\dot{\theta}^{N+1} = \dot{\theta}^N + \left(\ddot{\theta}^{N+1}\Delta t\right), \tag{A.2}$$

where N is the current time-step, $N+1$ is the next successive time-step, M_z is the total torque generated by the rotor, I is the rotor's moment of inertia about the axis of rotation (z-axis), $\ddot{\theta}$ is the angular acceleration, and $\dot{\theta}$ is the angular velocity. Similarly, if applied to a blade in rectilinear motion, the governing equations become:

$$\ddot{y}^{N+1} = \frac{F^N}{m} \tag{A.3}$$

$$\dot{y}^{N+1} = \dot{y}^N + \left(\ddot{y}^{N+1}\Delta t\right), \tag{A.4}$$

where F is the tangential force in the desired direction of motion, and m is the mass of the blade. Essentially, the approach is to extract the forces and moment on each blade from the CFD solver at each time-step, with the data then used in the respective governing equations (A.3 and A.1) to

compute the new motion to be implemented at the beginning of the proceeding time-step. For the traditional VAWT used as per the experimental case [53], the moment of each blade is extracted from the solver, summed together, and then used in Equation A.1 to compute the net rate of angular acceleration for the entire rotor. Equation A.2 provides the final rate of rotation to be returned to the CFD solver to be implemented in the simulation for the next time-step, with that rotation rate value also being stored in the user code for use as the $\dot{\theta}^N$ term in Equation A.2 during the computation at the following time-step.

Expanding the computational approach from the traditional VAWT to the D-VAWT requires a number of additional considerations. Firstly, and most notably, the D-VAWT's motion path presents an additional complexity to simulating start-up for this particular turbine. Up until now, the unique blade motion path has been governed through the time-step of the cycle and its breakdown on a per-region basis. This is only possible, however, when a *prescribed* velocity is assigned to the blade body. For the case of start-up, the velocity is calculated at each time-step of the simulation, and thus the total number of time-steps for any given cycle of motion is impossible to know a priori. Two potential solutions are seen to overcome this issue: the degrees-of-freedom of the blade's velocity could be controlled as a function of the blade's centroid position in the cycle, or the blade motion path could be prescribed beforehand through a more 'hardcoded' approach yet to be determined. Other complexities to the start-up analysis of the D-VAWT are the proper way to represent the entire rotor's acceleration, considering that some blades will be in rectilinear motion and others in rotation at any given point in time; as well as the proper treatment of moment of inertia of the blade and entire rotor. These complexities are solvable, and will indeed require solving to further solidify the D-VAWT concept.

A.4 Predicting Start-up Behaviour

Expected preliminary results are produced using the methodolgy described to implement VAWT start-up using STAR-CCM+. Figure A.4 is the characteristic start-up plot of the development of tip speed ratio in time. The overall trend shows the TSR to be increasing in time, which is essentially the definition of a wind turbine undergoing start-up. However, the isse here is that after 0.8s of physical time, the TSR is still quite close to zero. This is understandable, considering the TSR history plot of Hill et al. [53] given as Figure A.2 requires 200 s of physical runtime to achieve the steady-state TSR, and nearly 50 s to achieve a TSR of $\lambda = 1$. Since the current simulation

takes 3-4 days of runtime to achieve a physical time of $t = 0.8s$, the requirement for a substantial supercomputer resource is evident.

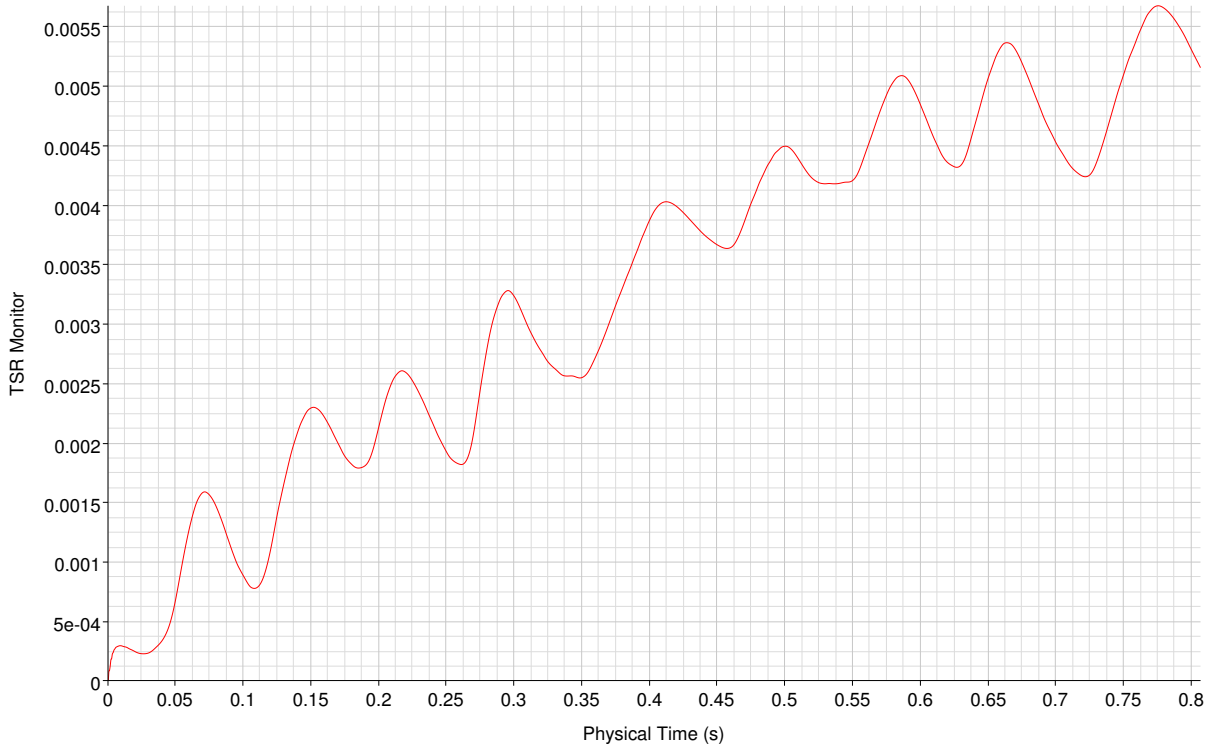

Figure A.4: Preliminary simulated TSR ramp-up for VAWT reference case [53].

The oscillations observed as the TSR follows its overall increasing trend can be explained by the pressure fields and moments experienced by the blades, provided in Figure A.5. In Figures A.5a and A.5b, blade 1 is at top dead-center, with blades 2 and 3 following in the counter-clockwise direction. Blade 1, at an angle of attack close to zero, contributes negligible moment force to the rotation of the rotor. Blades 2 and 3 explain the oscillatory behaviour, as they experience vortex shedding and volatile pressure fields as the flow field develops. Even at a TSR of $\lambda \approx 0.005$ after 0.8s of physical time, a slight counter-clockwise rotation of the VAWT rotor is noticeable in Figure A.5a.

Producing the TSR trend of Figure A.4 is a proof of concept. The approach successfully uses STAR-CCM+ user code to compute and assign the motion of the VAWT rotor body at each time-step. Given the proper computational resources and time, the methodology could be adapted to use with the D-VAWT or with any other VAWT under investigation.

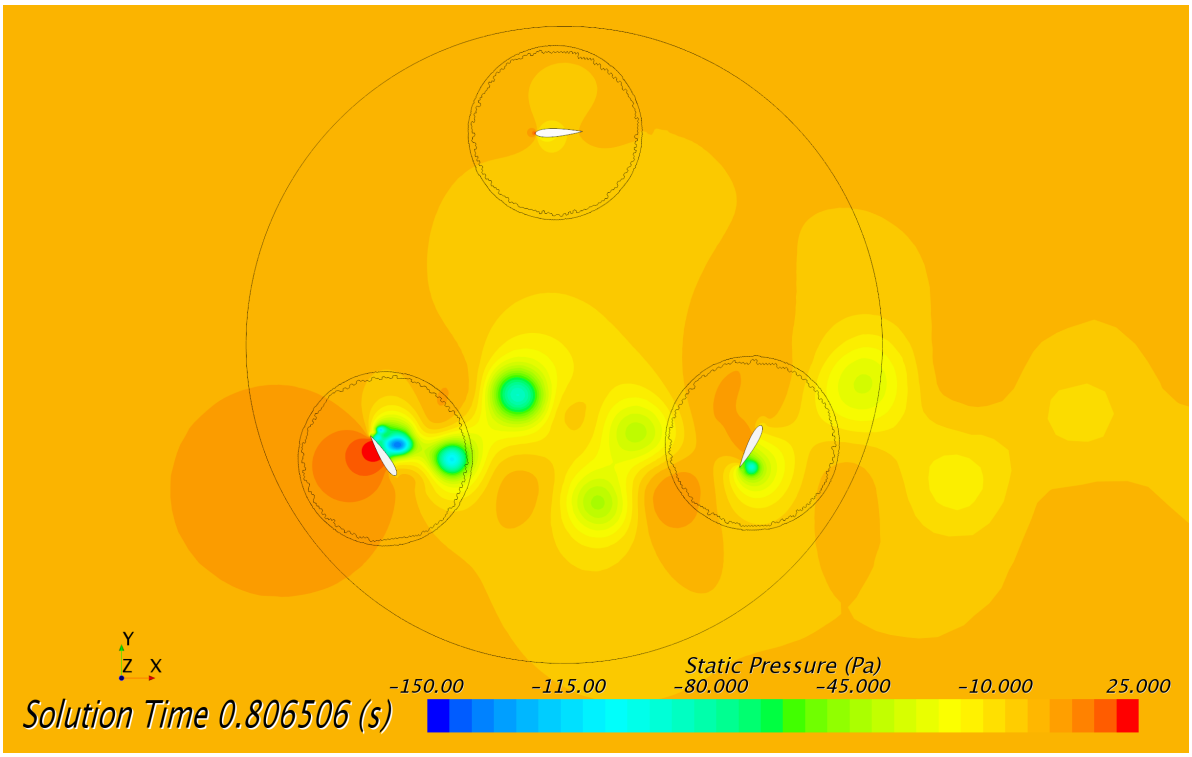

(a) Pressure field.

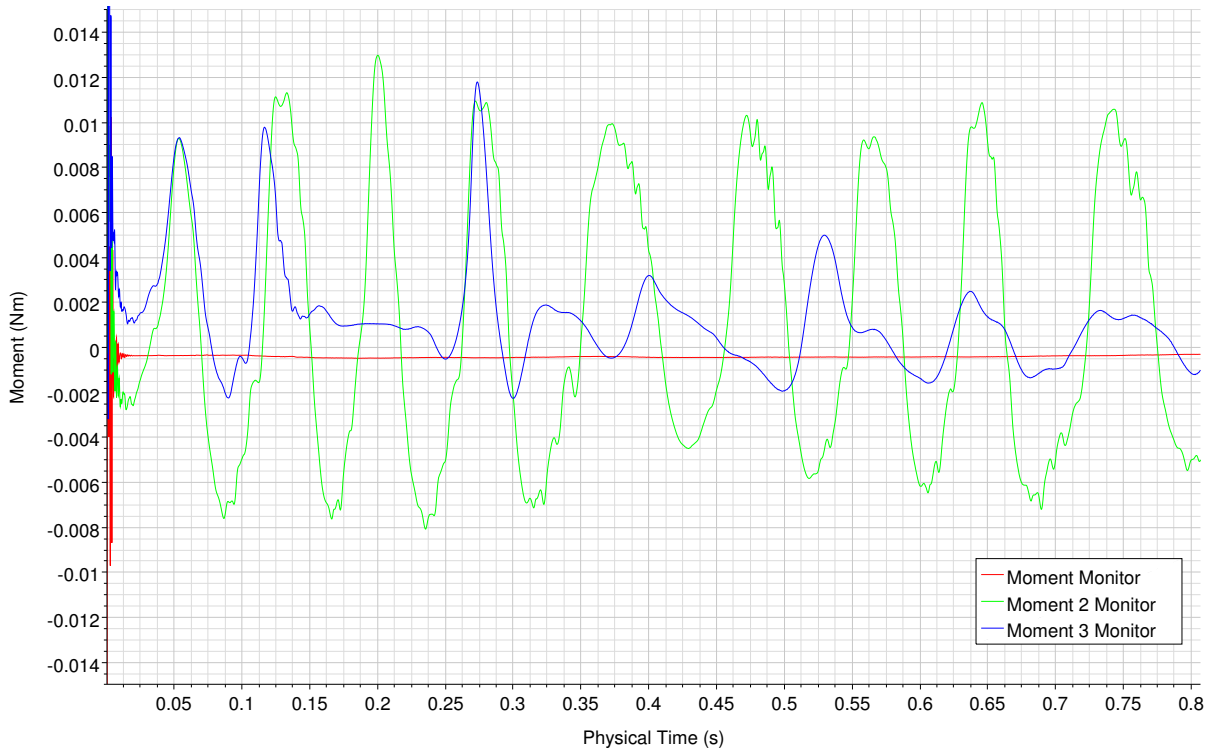

(b) Individual blade moments.

Figure A.5: Simulation results for initial start-up investigation.

Appendix B

User Code

B.1 D-VAWT Motion

Three separate user-defined field functions are defined to achieve the D-VAWT motion, namely: the axis of rotation, rate of rotation, and rate of translation. Each function is triggered using the pre-determined local time-step of the cycle (`CycleStep` variable).

Axis

```
($CycleStep <= 1000) ? [0,1.6,0] :
(
($CycleStep > 2273 && $CycleStep <= 3273) ? [0,-1.59939833476496,0] : [0,0,0]
)
```

Rotation

```
($CycleStep <= 1000) ? 22.5 :
(
($CycleStep > 2273 && $CycleStep <= 3273) ? 22.5 : 0
)
```

Translation

```
($CycleStep > 1000 && $CycleStep <= 2273) ? [0,-18,0] :
(
($CycleStep > 3273 && $CycleStep <= 4546) ? [0,18,0] : [0,0,0]
)
```

B.2 D-VAWT Active-Pitch Control

Active-pitch control is implemented by adding the blade pitch rate of rotation and pitch axis during the activation intervals. During pitch activation, the axis of rotation corresponds to the centroid coordinates of the body extracted using the point probe procedure. The $CG_y \pm (V_b)(\Delta t)$ term seen in the pitch axis y-coordinate is to account for STAR-CCM+'s execution of body rotation *after* any translation motion. For the active-pitch control scheme, the linear translation user definition remains the same as the baseline D-VAWT motion in Section B.1. The code provided here is for AP Scheme 1a, producing a pitch angle of $\phi = -5°$ in the South and East regions.

Axis

```
($CycleStep <= 1000) ? [0,1.6,0] :
(
($CycleStep > 2173 && $CycleStep <= 2273) ?
[${CGx_1Report}, ${CGy_1Report}-(18*${TimeStep}), 0.0] :

($CycleStep > 2273 && $CycleStep <= 3273) ?
[0,-1.59939833476496,0] :

($CycleStep > 4446 && $CycleStep <= 4546) ?
[${CGx_1Report}, ${CGy_1Report}+(18*${TimeStep}), 0.0] : [0,0,0]
)
```

Rotation

```
($CycleStep <= 1000) ? 22.5 :
(
 ($CycleStep > 2173 && $CycleStep <= 2273) ? -6.25 :

($CycleStep > 2273 && $CycleStep <= 3273) ? 22.5 :

($CycleStep > 4446 && $CycleStep <= 4546) ? 6.25 : 0
)
```

Translation

```
($CycleStep > 1000 && $CycleStep <= 2273) ? [0,-18,0] :
(
($CycleStep > 3273 && $CycleStep <= 4546) ? [0,18,0] : [0,0,0]
)
```

B.3 VAWT Start-Up

User-defined code in STAR-CCM+ is based on the `C` programming language and requires three separate files: a generic header file, library definition file, and source file containing the function(s) to execute and return information to the CFD solver. All three are provided here, with the `UserOmega` function of the source file being responsible for the rotor rate of rotation calculation.

B.3.1 Header File

```
#ifndef UCLIB_H
#define UCLIB_H
#ifdef DOUBLE_PRECISION
typedef double Real;
#else
typedef float Real;
#endif
typedef double CoordReal;

#ifdef __cplusplus
extern "C" {
#endif
#if defined(WIN32) || defined(_WINDOWS) || defined(_WINNT)
# define USERFUNCTION_EXPORT __declspec(dllexport)
# define USERFUNCTION_IMPORT __declspec(dllimport)
#else
# define USERFUNCTION_EXPORT
# define USERFUNCTION_IMPORT
#endif

extern void USERFUNCTION_IMPORT ucarg(void *, char *, char *, int);
extern void USERFUNCTION_IMPORT ucfunc(void *, char *, char *);
extern void USERFUNCTION_IMPORT ucfunction(void *, char *, char *, int, ...);

void USERFUNCTION_EXPORT uclib();
#ifdef __cplusplus
}
#endif
#endif
```

B.3.2 Library Defintion File

```
#include "uclib.h"

void UserOmega(Real*, int, CoordReal*, CoordReal*, CoordReal*, CoordReal*,
        CoordReal*, CoordReal*);
void SizeTest(Real*, int);

 void
  USERFUNCTION_EXPORT uclib()
  {
        ucfunc(UserOmega, "ScalarFieldFunction", "UserOmega");
        ucarg(UserOmega, "Cell", "$MomentReport", sizeof(CoordReal));
        ucarg(UserOmega, "Cell", "$Moment2Report", sizeof(CoordReal));
        ucarg(UserOmega, "Cell", "$Moment3Report", sizeof(CoordReal));
        ucarg(UserOmega, "Cell", "$Time", sizeof(CoordReal));
        ucarg(UserOmega, "Cell", "$TimeStep", sizeof(CoordReal));
        ucarg(UserOmega, "Cell", "$TimeLevelReport", sizeof(CoordReal));

        ucfunc(SizeTest, "ScalarFieldFunction", "SizeTest");

  }
```

B.3.3 Source File

```
#include "uclib.h"
#include <stdio.h>
#include <stdlib.h>
#include <math.h>

double Omega_new = 0.;
double Omega_old = 0.;
double lastAdded = 0.;
double lastTime = 0.;

#define I_ZZ 0.018      // Moment of inertia for entire turbine rotor

/* Determine the rotation rate for the following time-step based on integrated
    forces */
void USERFUNCTION_EXPORT
```

```
UserOmega(Real *result, int size, CoordReal *M1, CoordReal *M2, CoordReal *M3,
CoordReal *t, CoordReal *dt, CoordReal *step)
{

	int i = 0;
	int stepHold = 0;		// Number of time steps to hold turbine static for
	double alpha = 0.0;		// Angular acceleration (rad/s^2)

	/* Parallel processing check */
	if (size == 0)
	{
		return;
	}

	/* Initial Condition */
	if (t[0] == 0)
	{
		for (i=0; i < size; i++)
		{
			result[i] = 0;
		}

	}
	//if the solution has been cleared, reset history
	else if (t[0] < lastTime)
	{

		double Omega_new = 0.0;
		double Omega_old = 0.0;
		double lastAdded = 0.0;
		double lastTime = 0.0;
	}

	 /* Hold turbine steady for first few time steps */
	if (step[0] < stepHold)
	{
		for (i=0; i < size; i++)
		{
			result[i] = 0;
```

```
                }
        }
        // If new time step
        else if (t[0] > lastTime)
        {
                lastTime = t[0];
        }
        // If NOT new time step
        else
        {
                        Omega_old = Omega_old - lastAdded;      //Reset previous
                            omega variable
        }

        /* Compute rotation rate for input to following time step  */
        if (step[0] >= stepHold)
        {
                for (i=0; i < size; i++)
                {
                alpha = (M1[i] + M2[i] + M3[i])/I_ZZ;
                lastAdded = alpha*dt[0];
                Omega_new = Omega_old + lastAdded;

                result[i] = Omega_new;
                }

                Omega_old = Omega_new;

        }

}
```